

# A Measurement of Diffractive Charm Production at HERA

Dissertation

zur

Erlangung der naturwissenschaftlichen Doktorwürde  
(Dr. sc. nat.)

vorgelegt der

Mathematisch-naturwissenschaftlichen Fakultät  
der

Universität Zürich

von

Stefan Hengstmann

aus

Deutschland

Begutachtet von

Prof. Dr. Peter Truöl

Dr. Felix Sefkow

Zürich 2000

Die vorliegende Arbeit wurde von der Mathematisch-naturwissenschaftlichen Fakultät der Universität Zürich auf Antrag von Prof. Dr. Peter Truöl und Prof. Dr. Ulrich Straumann als Dissertation angenommen.

## Abstract

A measurement is presented of  $D^*$  meson production in diffractive deep-inelastic  $ep$  scattering at HERA. Diffractive processes are characterized experimentally by a large rapidity-gap where no particles are observed. They are attributed predominantly to the exchange of a colorless object, which can be interpreted as the pomeron. The cross section is measured in a kinematic range where the experimental acceptance is large and presented differentially as a function of various kinematic variables exploring the dynamics of diffractive charm production. The results are compared with a model based on a partonic pomeron as determined in a QCD analysis of the diffractive structure function, with perturbative QCD calculations of two gluon exchange and with a soft color interaction model.

## Zusammenfassung

Streuprozesse, bei denen die Quantenzahlen des Vakuums zwischen den beteiligten Teilchen ausgetauscht werden, bezeichnet man als diffraktiv. Sie können durch den Austausch eines farbneutralen Teilchens, des sogenannten *Pomerons*, parametrisiert werden. Experimentell sind diffraktive Ereignisse in der tiefinelastischen  $ep$ -Streuung bei HERA durch einen Bereich in der Pseudorapidität charakterisiert, in dem keine Teilchen nachgewiesen werden.

Die diffraktive Produktion von  $D^*$ -Mesonen wurde mit dem H1-Detektor im kinematischen Bereich hoher experimenteller Akzeptanz untersucht. Differenzielle Wirkungsquerschnitte als Funktion verschiedener kinematischer Variablen wurden gemessen und mit einem Modell verglichen, das auf einer partonischen Struktur des Pomerons beruht, wie sie aus der QCD-Analyse der inklusiven diffraktiven Strukturfunktion bestimmt wurde. Weiterhin werden Berechnungen des Zwei-Gluon-Austauschs in störungstheoretischer QCD und des sogenannten *Soft Color Interaction* Modells den gemessenen Wirkungsquerschnitten gegenübergestellt.

# Contents

<b>1</b>	<b>Theoretical Framework</b>	<b>3</b>
1.1	Kinematics of deep inelastic $ep$ -scattering . . . . .	3
1.2	Inclusive cross section and structure functions . . . . .	4
1.2.1	The naive quark parton model . . . . .	5
1.2.2	Scaling violation and perturbative QCD . . . . .	5
1.3	Charm production . . . . .	8
1.3.1	Fragmentation of charm quarks . . . . .	9
1.4	Diffraction deep inelastic scattering . . . . .	10
1.4.1	Hadron-hadron interactions and Regge theory . . . . .	11
1.4.2	Diffraction structure function $F_2^{D(3)}$ . . . . .	12
1.5	Charm in diffraction . . . . .	17
1.5.1	Resolved pomeron model . . . . .	17
1.5.2	Two-gluon model . . . . .	19
1.5.3	Soft color interaction model . . . . .	19
1.5.4	Monte Carlo implementation . . . . .	19
1.5.5	Model comparison . . . . .	20
<b>2</b>	<b>The H1 Detector at HERA</b>	<b>23</b>
2.1	The HERA positron-proton collider . . . . .	24
2.2	The H1 detector . . . . .	24
2.2.1	Time-of-flight system . . . . .	26
2.2.2	Luminosity measurement . . . . .	27
2.2.3	The central tracking detector . . . . .	27
2.2.4	Track finding and reconstruction . . . . .	30

2.2.5	The liquid argon calorimeter . . . . .	32
2.2.6	The backward detectors . . . . .	32
2.2.7	Forward detectors . . . . .	34
2.2.8	Trigger scheme . . . . .	35
2.2.9	Detector simulation . . . . .	39
<b>3</b>	<b>Event Selection</b>	<b>40</b>
3.1	Run selection . . . . .	40
3.1.1	The analysis subtrigger . . . . .	41
3.1.2	Luminosity . . . . .	41
3.2	Deep inelastic scattering events . . . . .	42
3.2.1	Selection of DIS events . . . . .	43
3.2.2	DIS kinematics . . . . .	44
3.3	Reconstruction of $D^*$ mesons . . . . .	45
3.3.1	Track selection . . . . .	46
3.3.2	Kinematic region . . . . .	47
3.4	Selection of diffractive events . . . . .	48
3.4.1	Forward cuts . . . . .	49
3.4.2	Diffractive kinematic region . . . . .	50
3.4.3	Diffractive $D^*$ production . . . . .	52
<b>4</b>	<b>Cross Section Measurement</b>	<b>55</b>
4.1	Determination of the cross section . . . . .	55
4.1.1	Noise correction $\nu$ . . . . .	56
4.1.2	Reflections . . . . .	57
4.1.3	Trigger efficiency . . . . .	58
4.1.4	Acceptance and reconstruction efficiency . . . . .	59
4.1.5	$M_Y$ smearing $S$ . . . . .	61
4.1.6	Cross check with the inclusive measurement . . . . .	63
4.2	Error calculation . . . . .	65
4.3	Results . . . . .	66
4.3.1	Diffractive charm cross section . . . . .	66
4.3.2	Comparison with models . . . . .	66
4.3.3	Comparison with ZEUS results . . . . .	72
4.3.4	Results from diffractive dijet production . . . . .	73

<b>5</b>	<b>Summary and Outlook</b>	<b>75</b>
<b>A</b>	<b>Reflection Background</b>	<b>77</b>
A.1.1	Reconstruction of $D^*$ decays on generator level . . . . .	77
A.1.2	Determination of the background . . . . .	80
<b>B</b>	<b>Reconstruction of Charm Mesons with the CST</b>	<b>82</b>
B.1	CST tracks . . . . .	82
B.2	Reconstructing $D^*$ mesons with the CST . . . . .	83
B.3	Reconstruction of the $D^0$ decay length . . . . .	84
B.3.1	Mass resolution of the $D^*$ and the $D^0$ meson . . . . .	85
B.4	$D^0$ lifetime . . . . .	85
<b>C</b>	<b>Calibration of the <math>Z</math>-Chambers</b>	<b>87</b>
C.1	Space point reconstruction . . . . .	87
C.2	CST reference tracks . . . . .	89
C.3	Calibration constants and their determination . . . . .	90
C.3.1	CIZ calibration with cosmic tracks . . . . .	91
C.3.2	$Z$ -superfit . . . . .	93
	<b>List of Figures</b>	<b>97</b>
	<b>List of Tables</b>	<b>100</b>
	<b>References</b>	<b>101</b>

# Introduction

The fundamental concern of elementary particle physics is the understanding of matter in terms of its smallest constituents and their interactions. The theory which describes the interactions between elementary particles is nowadays governed by *gauge theories*. Unifying the theories of the strong interactions, *Quantum Chromodynamics* (QCD) and the electroweak interactions, *Quantum Flavordynamics* the most comprehensive model is the *Standard Model* of elementary particle physics. Lepton-nucleon scattering experiments offer one possibility to test the predictions of the Standard Model.

The Hadron Electron Ring Accelerator (HERA), situated at the DESY<sup>1</sup> laboratory in Hamburg, has made it possible to study electron proton collisions at a center of mass energy of  $\sqrt{s} \simeq 300$  GeV. In QCD the proton is pictured to be composed of spin-half, point-like partons with fractional electric charge called *quarks*. The quarks are interacting by the exchange of massless gauge bosons known as *gluons*. *ep*-interactions are understood to be deep inelastic scattering (DIS). They are dominated by the exchange of a photon radiated by the electron and interacting with a parton of the proton. In DIS the proton structure can be explored in terms of the structure function  $F_2$  which depends on the density of the quarks and gluons in the proton.

At HERA *rapidity gap* events are observed where the emerging particles are separated by a large region in pseudorapidity devoid of any hadronic energy. Such events constitute approximately 10% of the inclusive DIS cross section. They have been interpreted as *diffractive* processes, in which no quantum numbers are exchanged between the interacting particles. Such processes were known from earlier hadron-hadron experiments and were described phenomenologically in terms of Regge theory before the advent of QCD. At high energies the dominant contribution to the cross section is due to the exchange of a colorless object, the *pomeron*, which carries the vacuum quantum numbers. At HERA the pomeron can be described as an object with a partonic structure. In the same way as the proton the pomeron structure can be understood in terms of a diffractive structure function  $F_2^{D(3)}$  and its partonic content can be determined in the framework of perturbative QCD.

Diffractive *open charm* production in DIS is sensitive to the gluon content of the exchange, since charm quarks are predominantly produced by gluon induced processes. In this thesis a measurement of differential cross sections is presented which explore the dynamics of diffractive charm production. The measurement is based upon data which were collected with the H1 detector during the years 1995, 1996 and 1997.

---

<sup>1</sup>DESY=Deutsches Elektronen Synchrotron

The thesis starts with a theoretical overview of diffractive deep inelastic scattering. In the second part of Chapter 1 different theoretical approaches to diffractive charm production are introduced. The HERA accelerator and the H1 experiment are described in Chapter 2. The subjects of Chapter 3 are the technical aspects of the detection of diffractive charm events in DIS and the reconstruction of the kinematic variables. The selection method of charm events using the decay mode  $D^* \rightarrow D^0 \pi_s \rightarrow (K\pi)\pi_s$  is described and the kinematic region for which the cross sections are measured is defined. In the first part of Chapter 4 the correction procedure used to determine the cross sections is explained and the systematic uncertainties are discussed. The second part of Chapter 4 is devoted to the presentation and interpretation of the cross sections in comparison with the models for diffractive charm production. Chapter 5 summarizes the results and gives an outlook for future analyses on the topic at HERA.

The determination of a correction factor relevant for the cross section measurement is carried out in Appendix A. A study exploiting the central silicon detector for the reconstruction of charm events is presented in Appendix B. Finally, technical aspects of the alignment and calibration of the central inner and outer  $z$ -chambers CIZ and COZ are treated in Appendix C.

# Chapter 1

## Theoretical Framework

This analysis concerns the measurement of cross sections for charm production in deep inelastic diffractive scattering. Firstly the kinematics of the inclusive scattering process  $ep \rightarrow eX$  is explained and the basic ideas of its description in the framework of the theory of the strong interaction - QCD - are introduced. Thereafter diffractive processes, measured at HERA, are defined in terms of a topological decomposition of the final state hadrons into two distinct systems  $X$  and  $Y$  separated by a so-called rapidity gap. Kinematic variables frequently referred to in diffractive scattering are explained. Different theoretical approaches to diffractive charm production exist. Those which will be directly compared with the presented measurement are introduced in the last part of this chapter.

### 1.1 Kinematics of deep inelastic $ep$ -scattering

Figure 1.1 shows the dominant deep inelastic  $ep$ -scattering (DIS) process measured at HERA. The incoming positron<sup>1</sup> carrying the four-momentum  $l$  scatters off the proton by the exchange of a photon or a  $Z^0$  boson (*neutral current*) carrying the four-momentum  $q$ . The square of the four-momentum transfer and the total center of mass energy of the process are given by

$$Q^2 \equiv -q^2 = -(l - l')^2 \quad \text{and} \quad (1.1)$$

$$s = (p + l)^2 \simeq 4E_e E_p . \quad (1.2)$$

where  $E_e$  and  $E_p$  are the energies of the incoming positron and proton, respectively. The rest masses of the positron and proton are neglected here and in the following.

For fixed center of mass energies  $\sqrt{s}$  the DIS process can uniquely be described by the two dimensionless variables Bjorken- $x$  and inelasticity  $y$  defined as

$$x = \frac{Q^2}{2(q \cdot p)} \quad 0 \leq x \leq 1 , \quad (1.3)$$

$$y = \frac{q \cdot p}{l \cdot p} \quad 0 \leq y \leq 1 . \quad (1.4)$$

---

<sup>1</sup>HERA is able to collide both positrons and electrons with protons. In this thesis the term *positron* is used to describe generically electrons and positrons.

These variables are related to  $Q^2$  by the equation  $Q^2 = xys$ .

Because of baryon number conservation, the invariant mass of the hadronic final state  $X$

$$W^2 = (q + p_p)^2 = Q^2 \cdot \left(\frac{1}{x} - 1\right) \quad (1.5)$$

is constraint to be at least the proton rest mass  $m_p$ .

Two kinematic regions can be defined: For  $Q^2 \rightarrow 0$  almost real photons are radiated off the positron defining the *photoproduction* region; while the region  $Q^2 \gtrsim 1 \text{ GeV}^2$  and  $W^2 \gg m_p^2$  is the domain of *deep inelastic scattering* and the region of interest for the present analysis.

For moderate values of  $Q^2$  ( $Q^2 \leq 100 \text{ GeV}^2$ ) the  $ep$ -interaction is predominantly mediated by a photon since  $Z^0$ -exchange is suppressed by a factor  $\sim Q^2/(Q^2 + M_Z^2)$ , where  $M_Z$  is the rest mass of the  $Z^0$  boson. For the same argument *charged current* contributions ( $W^\pm$ -exchange) are negligible.

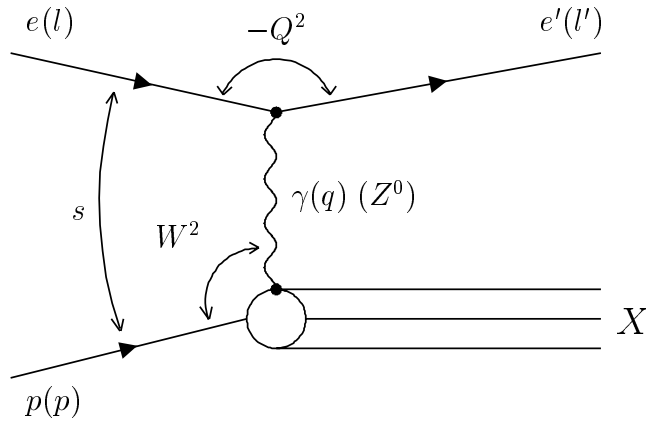


**Figure 1.1:** *Generic Feynman diagram for ep-scattering.*

## 1.2 Inclusive cross section and structure functions

The inclusive cross section of the DIS process  $ep \rightarrow eX$  is, in lowest order QED<sup>2</sup>, proportional to the product of a leptonic tensor  $L_{\mu\nu}$  and a hadronic tensor  $W_{\mu\nu}$

$$\sigma \propto L_{\mu\nu} W^{\mu\nu} \quad (1.6)$$

$L_{\mu\nu}$  describes the interaction between the positron and the exchanged photon and is exactly calculable in QED. Since the proton structure is a-priori unknown,  $W_{\mu\nu}$ , which describes the interaction between the photon and the proton, is not calculable and must be determined from experiments.

---

<sup>2</sup>*Quantum Electrodynamics*

The requirement of Lorentz invariance and current conservation leads to the expression for the inclusive double differential cross section

$$\frac{d^2\sigma(ep \rightarrow eX)}{dx dQ^2} = \frac{4\pi\alpha_{em}^2}{xQ^4} (y^2 x F_1(x, Q^2) + (1-y) F_2(x, Q^2)) \quad (1.7)$$

where  $\alpha_{em}$  is the electromagnetic coupling constant and  $F_1(x, Q^2)$  and  $F_2(x, Q^2)$  are structure functions depending on the Bjorken scaling variable  $x$  and  $Q^2$  and containing the information of the dynamics of the process. An interference term  $F_3$  accounting for contributions from  $Z^0$  exchange and interference terms between  $\gamma$  and  $Z^0$  exchange is neglected in Equation 1.7 for the reasons discussed in the previous Section 1.1.

### 1.2.1 The naive quark parton model

In the naive quark parton model (QPM) [1] the proton is considered to be composed of non-interacting point-like partons. The positron-proton interaction cross section is approximated by an incoherent sum of elastic positron-parton cross sections. The QPM has to be reconciled with the *static* parton model where the proton (like all baryons) consists of three fractionally charged constituents, namely *quarks*. This is achieved by distinguishing between the three *valence* quarks  $uud$ , which determine the quantum numbers of the proton and a *sea* of quark anti-quark pairs which have no net flavor.

In the QPM the process  $ep \rightarrow eX$  is described in terms of *parton density functions*  $f_i(x)$  giving the probability of finding a parton of type  $i$  and charge  $e_i$  carrying the fraction  $x$  of the proton's momentum. The following relation between them and the structure functions  $F_1(x, Q^2)$  and  $F_2(x, Q^2)$  (see Section 1.2) can be established:

$$F_1(x, Q^2) = \frac{1}{2} \sum_i e_i^2 f_i(x) \quad (1.8)$$

$$F_2(x, Q^2) = x \sum_i e_i^2 f_i(x) \quad (1.9)$$

The combination of these two equations leads to

$$F_2(x, Q^2) = 2xF_1(x, Q^2) \quad (1.10)$$

which is called the Callan-Gross relation [2] and is a consequence of the spin-half nature of the quarks. As can be seen from Equation 1.9 the QPM implies that  $F_2(x, Q^2)$  should not depend on  $Q^2$  for fixed values of  $x$ . This behavior was expected by Bjorken and is known as *scaling invariance* [3]. Figure 1.2 shows a measurement of  $F_2(x, Q^2)$  as a function of  $Q^2$  for various values of  $x$  [4]. Only little dependence on  $Q^2$  is observed over a wide kinematic range. However, slight deviations from this scaling behavior occur in particular for low values of  $x$ .

### 1.2.2 Scaling violation and perturbative QCD

One of the basic assumptions of the QPM (see Section 1.2.1) is that the sum of the momenta of the quarks and anti-quarks equal that of the proton which can be expressed

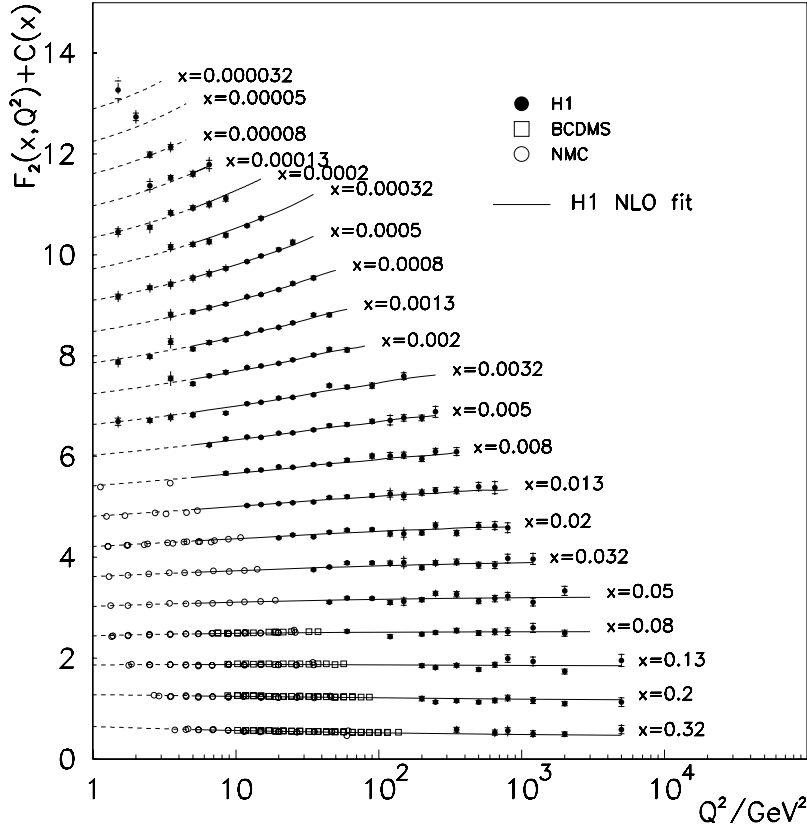


Figure 1.2: Scaling violation of  $F_2(x, Q^2)$ .

by the sum rule:

$$\sum_i \int_0^1 x f_i(x) dx = 1. \quad (1.11)$$

Measurements however have demonstrated that the total momentum carried by the quarks amounts to approximately only half the momentum of the proton [5], which is a strong evidence that quarks cannot be the only constituents of the proton. On the other hand the measurement of  $F_2(x, Q^2)$  shows a dependence on  $Q^2$  (see Figure 1.2) and the scaling invariance is *violated* which is in contrast to the prediction of the QPM.

These effects can be explained in terms of the theory of the strong interaction, *Quantum Chromodynamics* QCD. In QCD the proton is composed of quarks interacting by the exchange of *gluons*. Quarks carry an additional degree of freedom, *color*. Color is exchanged by eight gluons, which carry different combinations of color charge. Gluons are massless, electrically neutral and have spin 1. In contrast to photons gluons are able to couple to each other. The self-coupling of the color field leads to the dependence of the strong coupling constant  $\alpha_s$  on the scale  $\mu^2$  (e.g.  $Q^2$ )

$$\alpha_s(Q^2) = \frac{12\pi}{(33 - 2N_f) \ln(Q^2/\Lambda_{QCD}^2)} \quad (1.12)$$

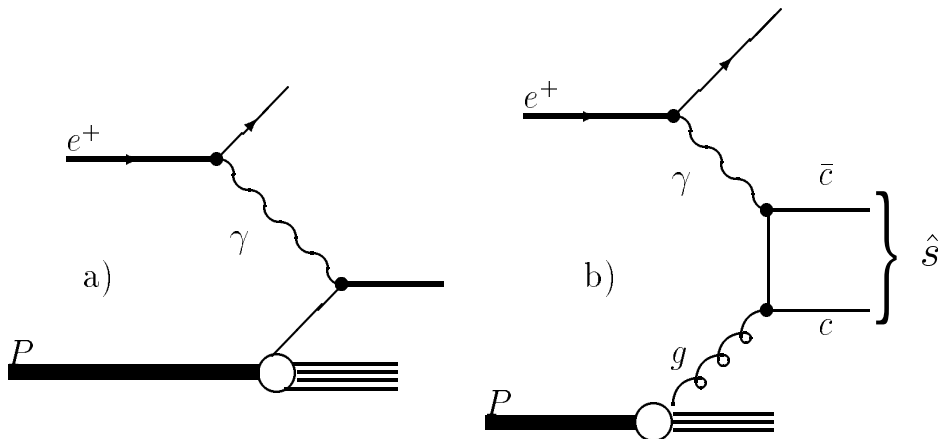


**Figure 1.3:** Leading order diagrams for a) charm production via flavor excitation and b) photo-gluon fusion.

where  $N_f$  is the number of quark flavors and  $\Lambda_{QCD}$  a parameter that has to be determined from experiments. With increasing  $Q^2$  the coupling strength becomes small (*asymptotic freedom*), and conversely, when  $Q^2$  decreases,  $\alpha_s$  becomes large and the quarks are strongly bound together (*confinement*). In the regime of DIS measurements ( $Q^2 \gtrsim 1 \text{ GeV}^2$ )  $\alpha_s$  is sufficiently small and perturbative QCD (pQCD) is applicable. Within pQCD it is not possible to calculate the parton densities from first principles. However predictions on the evolution of these parton densities as a function of  $\ln(Q^2)$  can be calculated within the framework of the DGLAP<sup>3</sup> evolution equations [6]. The DGLAP formalism successfully describes the scaling violation of the structure function  $F_2(x, Q^2)$ . This can be seen in Figure 1.2, where a fit based on this description is shown together with the data.

The **QCD factorization theorem** states that the  $ep$ -interaction can be divided into a perturbative *short distance* part and a non-perturbative *long distance* part. The non-perturbative part can not be calculated and has to be determined experimentally. In the perturbative part  $\alpha_s$  is sufficiently small to allow an expansions in a series of powers of  $\alpha_s$ . The structure function  $F_2(x, Q^2)$  can be expressed as a convolution of a coefficient function  $C_2^i$  calculable in pQCD and the parton distribution function  $f_i$  of the proton,

$$F_2(x, Q^2) = \sum_{f_i=q, \bar{q}, g} \int_x^1 d\xi C_2^i \left( \frac{x}{\xi}, \frac{Q^2}{\mu^2}, \frac{\mu_f^2}{\mu^2}, \alpha_s(\mu^2) \right) f_i(\xi, \mu_f, \mu) \quad (1.13)$$

where  $\mu_f$  is the *factorization scale*, which defines the boundary between the perturbative and non-perturbative regions and  $\mu$  is the *renormalization scale* used to absorb the divergent parts of the perturbation series.

A detailed introduction to the theory of QCD can be found in (e.g. [7, 8]).

<sup>3</sup>Dokshitzer, Gribov, Lipatov, Altarelli, Parisi

### 1.3 Charm production

At HERA charm is produced via the production mechanisms of *photon-gluon fusion* (PGF)  $\gamma g \rightarrow c\bar{c}$ , where the photon, radiated by the incoming positron, interacts with a gluon of the proton. Charm may also be produced when the photon scatters off a charm quark in the sea of the proton, often referred to as *flavor excitation*. Leading order diagrams for both processes are sketched in Figure 1.3. Their relative contributions have been measured at H1 by detecting  $D^*$  mesons in the kinematic range  $10 < Q^2 < 100 \text{ GeV}^2$  [9]. The measurement excludes at 95% confidence level a 5% contribution from charm sea quarks to the total charm production. In this analysis charm is measured in the range  $2 < Q^2 < 100 \text{ GeV}^2$  and only the photon-gluon process is considered. The cross section of this process is sensitive to the gluon density in the proton. The momentum fraction of the proton carried by the gluon which enters the PGF process  $x_g$  can be related to the invariant mass squared of the  $c\bar{c}$  system  $\hat{s} = (p_{\bar{c}} + p_c)^2$  (see Figure 1.3). In leading order  $x_g$  can be reconstructed from

$$x_g = x \left( 1 + \frac{\hat{s}}{Q^2} \right) \quad \text{with} \quad \hat{s} = \frac{p_{Tc}^{*2} + m_c^2}{z(1-z)} \quad (1.14)$$

and

$$z \equiv \frac{p \cdot c}{p \cdot q} = \frac{(E - p_z)_c^{lab}}{2yE_e} \quad (1.15)$$

where  $c$  denotes the four-momentum of the charm quark and  $p_{Tc}^{*2}$  the transverse momentum in the  $\gamma^*p$  center of mass system (CMS). The Lorentz invariant  $z$  can be calculated in the laboratory frame from the energy  $E$  and the longitudinal momentum  $p_z$  of the  $c$  quark. For PGF processes it can be correlated with the quark scattering angle in the photon-gluon CMS. The  $c$  quark is not measured directly but can be detected, like in this analysis, via the identification of  $D^*$  mesons through the decay chain  $D^{*\pm} \rightarrow D^0 \pi_s^\pm \rightarrow (K^\mp \pi^\pm) \pi_s^\pm$ . The hadronic observable  $x_g^{obs}$  is defined by replacing  $p_{Tc}^{*2}$  with  $1.2 \cdot p_T(D^*)$  and  $(E - p_z)_c^{lab}$  with  $(E - p_z)_{D^*}^{lab}$  in Equation 1.14 and 1.15 and can therefore be used as an estimator for the gluon momentum fraction  $x_g$ . The factor 1.2 has been introduced to account for the average reduction in the momentum of the  $D^*$  meson compared to the  $c$  quark. H1 has measured the cross section for  $D^*$  meson production differentially as a function of  $x_g^{obs}$  [10]. The gluon density  $x_g g(x_g)$  has been unfolded from the  $x_g^{obs}$  distribution, where the factorization scale  $\mu_f^2 = 4m_c^2 + Q^2$  has been used. The measurement reaches down to values of  $x_g$  of  $\approx 10^{-3}$  and has been found to be in good agreement with the *indirect* extraction of  $x_g g(x_g)$  from the  $F_2$  data [4]. The local behavior of the structure function  $F_2$  at a given value of  $x$  depends on the gluon distribution  $x_g g(x_g)$  in a rather wide range of values of the momentum fraction  $x_g$ , and the analysis requires the assumption of a certain functional form of  $x_g g(x_g)$ , the parameters of which are then determined in a fit procedure. In this sense the measurement of open charm conveniently provides a *direct* measure of the gluonic structure of the proton.

### 1.3.1 Fragmentation of charm quarks

The measured particles are the hadrons emerging from the *fragmentation* of the charm quarks. This process can not be derived from first principles but has to be described by phenomenological models. Two models are commonly used, the rather sophisticated *Lund String Model* [11], where the hadronization is modelled by the fragmentation of color *strings* spanned between the charm quarks and the partons in the proton, and the simpler *Peterson fragmentation* [12], describing the transition of the  $c$  quark with momentum  $p_c$  to a charmed hadron  $h$  with momentum  $zp_c$  using the probability function

$$D_h(z) = \frac{N_h}{z(1 - \frac{1}{z} - \frac{\epsilon_c}{1-z})^2} . \quad (1.16)$$

The normalization factor  $N_h$  is constraint by the requirement  $\sum_h \int_0^1 x D_h(x) dx = 1$ . The free parameter  $\epsilon_c$  is of  $\mathcal{O}(m_q^2/m_c^2)$  where  $m_q^2$  is the mass of the light anti-quark picked up from the vacuum by the  $c$  quark. The smaller  $\epsilon_c$  the harder the momentum spectrum of the charmed hadron. The fragmentation process is assumed to be independent of the underlying hard scattering process. In a way similar to the factorization of the proton structure function (see Section 1.2.2), the charm hadron cross section can be described by a convolution of the non-perturbative fragmentation function with a perturbative evolution term. Peterson fragmentation functions are plotted in Figure 1.4(a) for different values of  $\epsilon_c$ , which are determined from fits to data measured at  $e^+e^-$  colliders. Figure 1.4(b) shows a measurement performed by the ARGUS [13] and CLEO [14] collaborations in  $e^+e^-$  annihilations at center of mass energies of  $\sqrt{s} \simeq 10$  GeV. The inclusive  $D^0$  and  $D^*$  cross sections are measured as a function of the variable  $x_p = p/p_{max}$  which is a close approximation to the variable  $z$ . A value of  $\epsilon_c = 0.078 \pm 0.008$  is extracted from the fit to the  $D^*$  distribution.

Measurements of the type performed for  $e^+e^-$  data have not yet been done at HERA since the center of mass energy of the  $\gamma g$  system is not known a priori. Furthermore color interactions with the proton remnant may affect charm fragmentation in  $ep$  interactions [17].

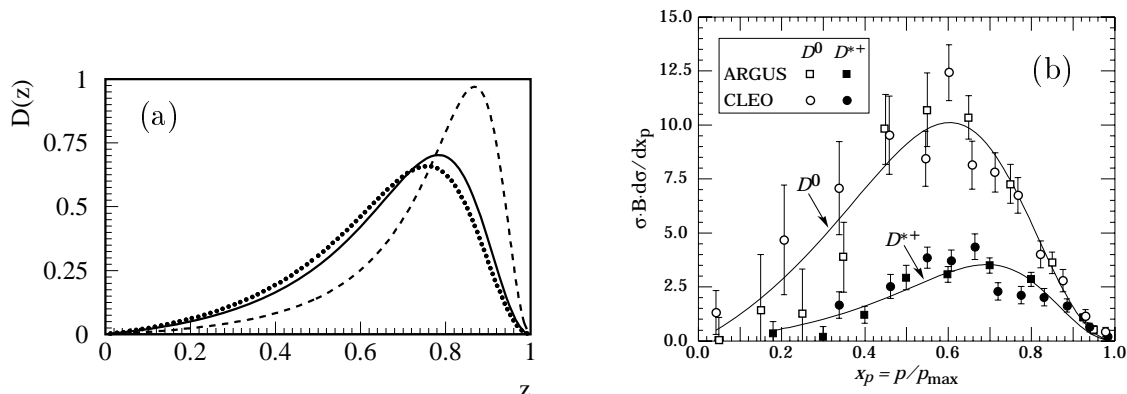


**Figure 1.4:** (a) Peterson fragmentation function for  $\epsilon_c = 0.02$  (dashed) [15],  $0.06$  (solid) [16] and  $0.078$  (dotted) [68]. (b)  $D^0$  and  $D^*$  cross sections measured in  $e^+e^-$  scattering as a function of  $x_p = p/p_{max}$ . The data are fitted by Peterson fragmentation functions. The  $D^*$  spectrum yields a parameter of  $\epsilon_c = 0.078 \pm 0.008$ .

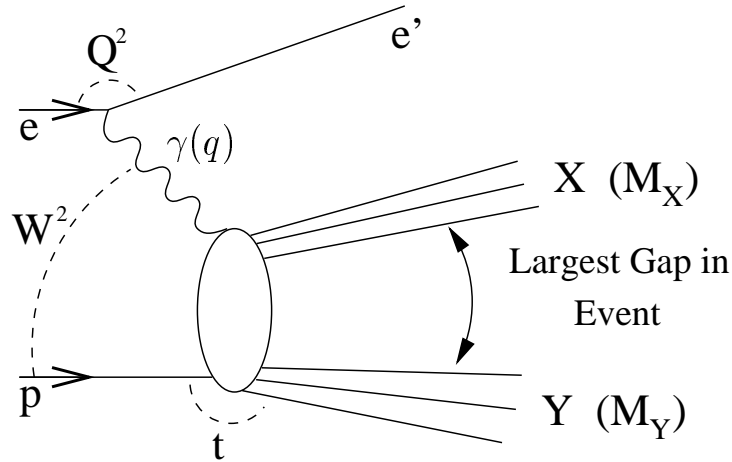


**Figure 1.5:** Diagram representing the inclusive deep inelastic diffractive scattering process. The process is described by the 4-vectors of the system  $X$  ( $X$ ), the system  $Y$  ( $Y$ ), the exchanged photon  $\gamma$ , the incoming proton ( $p$ ), and the squared four-momentum transfer at the proton vertex ( $t$ ).

## 1.4 Diffractive deep inelastic scattering

In this analysis open charm events are measured in diffractive deep inelastic scattering. Before the models for diffractive open charm production will be introduced, the general features of inclusive diffractive DIS events are described in the following.

Studies of DIS events at HERA revealed the presence of *rapidity gap events* of the form  $ep \rightarrow eXY$  [18, 19]. Two distinct hadronic systems  $X$  and  $Y$  are separated by the largest interval in rapidity without any hadronic activity between the final state hadrons, see Figure 1.5. The proton can either scatter *elastically* ( $M_Y = m_p$ ) or *dissociate* diffractively into a low-mass state ( $M_Y > m_p$ ). Diffractive events are interpreted as being due to *diffractive interactions* between the photon and the proton mediated by the exchange of a colorless object, the *pomeron*<sup>4</sup> ( $\mathbb{P}$ ).

Diffractive DIS processes are described using kinematic variables, which can be defined with reference to Figure 1.5:

$$x_p = \frac{q \cdot (p - Y)}{q \cdot p} = \frac{(Q^2 + M_X^2 - t^2)}{(Q^2 + W^2 - m_p^2)} \simeq \frac{(Q^2 + M_X^2)}{(Q^2 + W^2)} \quad (1.17)$$

$$\beta = \frac{Q^2}{2q \cdot (p - Y)} = \frac{Q^2}{(Q^2 + M_X^2 - t^2)} \simeq \frac{Q^2}{(Q^2 + M_X^2)} \quad (1.18)$$

where  $M_X$  and  $M_Y$  are the invariant masses of the systems  $X$  and  $Y$  and  $t = (p - Y)^2$  is the momentum transfer squared at the proton vertex.  $x_p$  is, in the limit  $t \rightarrow 0$ , the fraction of the proton momentum carried by the pomeron.

<sup>4</sup>In this thesis the terms *pomeron exchange* and *diffractive* are used synonymously.

### 1.4.1 Hadron-hadron interactions and Regge theory

Diffractive processes are known from hadron-hadron interactions. Since the strong forces between the hadrons take place at small momentum transfer such *soft* processes are not perturbatively calculable. They can be described within the phenomenological framework of Regge theory [20, 21]. In Regge theory, cross sections are described by the  $t$ -channel exchange of so-called *Regge trajectories*, which show up as approximately straight lines if one plots the angular-momentum of possible exchanged particles versus their mass squared (Chew-Frautschi plot). When treating the angular-momentum as a continuous, complex variable,  $\alpha(t)$ , the trajectories can be expressed in a simple linear form

$$\alpha(t) = \alpha(0) + \alpha' t . \quad (1.19)$$

Resonances corresponding to mesons like e.g.  $\rho, \omega, \phi$  are observed at physical values of spin, such that  $Re(\alpha(t))$  is an integer or half-integer, known as *Regge poles*.

Regge theory states that the forward elastic amplitude  $T_{el}$  for a process  $AB \rightarrow AB$ , where  $A$  and  $B$  are the four-momenta of the scattering hadrons, has the form  $T_{el}(s, t) \propto s^{\alpha(t)}$  and is related to the total cross section via the *Optical Theorem*

$$\sigma_{tot} \sim \frac{1}{s} Im(T_{el})_{t=0} \quad (1.20)$$

and therefore in the limit  $t \rightarrow 0$

$$\sigma_{tot} \propto s^{\alpha(0)-1} . \quad (1.21)$$

The intercept  $\alpha(0)$  of a Regge trajectory thus determines the energy dependence of the total cross section for a given process. Since all known meson trajectories have intercepts  $\alpha(0) \lesssim 0.6$  the total cross section falls rapidly with increasing center of mass energy  $\sqrt{s}$ . This is in contradiction to measurements made in  $pp$  and  $p\bar{p}$  scattering experiments showing a slow rise of the elastic and the total cross section with  $\sqrt{s}$ . Such behavior can be described by a trajectory with an intercept  $\alpha(0) \gtrsim 1$  carrying the quantum numbers of the vacuum and is known as the pomeron, after Pomeranchuk. The pomeron trajectory was determined by Donnachie and Landshoff from the total cross sections in  $pp$  and  $p\bar{p}$  collisions using a parameterization

$$\sigma_{tot} = A_{\mathbb{P}} s^{\alpha_{\mathbb{P}}(0)-1} + A_{\mathbb{R}} s^{\alpha_{\mathbb{R}}(0)-1} \quad (1.22)$$

with free normalizations  $A_{\mathbb{P}}$  and  $A_{\mathbb{R}}$  and intercepts  $\alpha_{\mathbb{P}}$  and  $\alpha_{\mathbb{R}}$  of the contribution from pomeron ( $\mathbb{P}$ ) and reggeon<sup>5</sup> ( $\mathbb{R}$ ) exchange [22]. The intercepts were found to be

$$\alpha_{\mathbb{P}}(0) = 1.08 \quad \text{and} \quad \alpha_{\mathbb{R}}(0) = 0.55 \quad (1.23)$$

and an excellent agreement with hadron-hadron cross section measurements over a wide region of phase space were achieved. However, no physical particle has been observed corresponding to the pomeron trajectory, explaining the enduring attempts to understand its identity.

---

<sup>5</sup>The name *reggeon* refers to any trajectory other than that of the pomeron.

### 1.4.2 Diffractive structure function $F_2^{D(3)}$

Diffractive processes have been observed in soft hadronic interactions and were successfully described in terms of Regge theory before the advent of QCD. However, this phenomenological model makes no prediction about the possible partonic nature of the pomeron. The hard scale in DIS at HERA allows one to probe its structure within the framework of pQCD.

In a partonic interpretation of the pomeron  $\beta$  is the momentum fraction of the pomeron carried by the parton interacting with the photon and therefore may be interpreted as the analogue of the scaling variable  $x$  in inclusive DIS (see Section 1.1). It can be seen from Equations 1.17 and 1.18 that  $x = \beta \cdot x_{\mathbb{P}}$ . Diffractive DIS is used to probe the partonic structure of the pomeron. This is formalized by defining diffractive structure functions (see e.g. [23]) in analogy with the inclusive structure function  $F_2(x, Q^2)$  (see Section 1.2), such that

$$\frac{d^5\sigma(ep \rightarrow eXY)}{d\beta dQ^2 dx_{\mathbb{P}} dt dM_Y} = \frac{4\pi\alpha_{em}^2}{\beta Q^4} \left(1 - y + \frac{y^2}{2}\right) F_2^{D(5)}(\beta, Q^2, x_{\mathbb{P}}, t, M_Y). \quad (1.24)$$

The variables  $\beta$ ,  $Q^2$  and  $x_{\mathbb{P}}$  are reconstructed from the scattered positron and the hadronic system  $X$ . The system  $Y$  is usually not measured directly and the resolution in  $t$ , which may be reconstructed from the transverse momentum of the system  $X$ , is very poor. Therefore, an integration is performed over the two unmeasured quantities in a range of  $M_Y$  and  $t$  given by the experimental acceptance for the detection of system  $Y$ , to produce measurements of  $F_2^{D(3)}(\beta, Q^2, x_{\mathbb{P}})$ . For most measurements  $x_{\mathbb{P}}$  is required to be less than 0.05, so that  $Y$  takes at least 95% of the momentum carried by the initial state proton.

The factorization hypothesis [24] assumes the diffractive structure function, given by Equation 1.24, to be dominated by pomeron exchange so that it may be written as the product of two independent terms

$$F_2^{D(3)}(\beta, Q^2, x_{\mathbb{P}}) = f_{\mathbb{P}/p}(x_{\mathbb{P}}) F_2^{\mathbb{P}}(\beta, Q^2) \quad (1.25)$$

where  $F_2^{\mathbb{P}}(\beta, Q^2)$  describes the partonic structure of the pomeron, and  $f_{\mathbb{P}/p}(x_{\mathbb{P}})$  denotes the  $t$ -integrated pomeron *flux* describing the probability of the production of pomerons from the proton. The pomeron flux is assumed to follow a Regge behavior with an approximate  $1/x_{\mathbb{P}}$  dependence

$$f_{\mathbb{P}/p}(x_{\mathbb{P}}, t) \sim f(t) \left(\frac{1}{x_{\mathbb{P}}}\right)^{2\alpha(t)-1}. \quad (1.26)$$

Here  $\alpha(t)$  is the pomeron trajectory, see Equation 1.19 in Section 1.4.1.

The latest measurement of  $F_2^{D(3)}$  by H1 [25] is presented in Figure 1.6. The quantity  $x_{\mathbb{P}} F_2^{D(3)}$  is shown for various ranges of  $\beta$  and  $Q^2$ . It can be seen that over most of the kinematic region covered  $x_{\mathbb{P}} F_2^{D(3)}$  is either falling, or approximately constant, as a function of increasing  $x_{\mathbb{P}}$ . This observation is different to that expected for a leading meson trajectory, but consistent with the exchange being dominated by the pomeron.

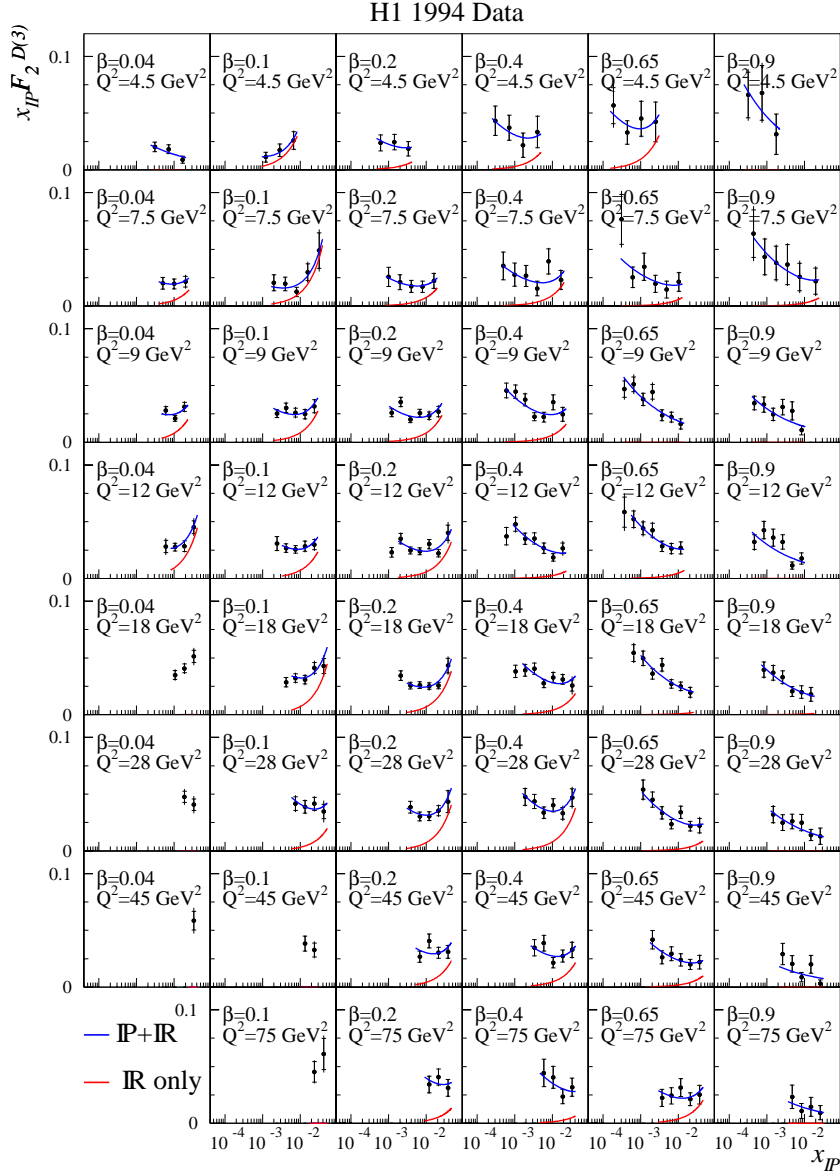


**Figure 1.6:** The diffractive structure function, as measured by H1 [25], plotted as  $x_{IP} F_2^{D(3)}(x_{IP}, \beta, Q^2)$  against  $x_{IP}$  for various  $\beta$  and  $Q^2$  values. The curves show the result of a Regge parameterization, where the lower line corresponds to the reggeon contribution, and the upper line to the total pomeron plus meson contribution.

Since the form of the  $x_{\mathbb{P}}$  dependence changes at large  $x_{\mathbb{P}}$  for some values of  $\beta$  and  $Q^2$ , the data can not be explained by the exchange of a single factorizable Regge trajectory. A natural explanation for this feature is the presence of sub-leading exchanges in addition to the leading pomeron, which lie on the approximately degenerate reggeon trajectory  $\alpha_{\mathbb{R}}(t) \simeq 0.55 + 0.9t$  and which carry the quantum numbers of the  $\rho$ ,  $\omega$ ,  $a$  or  $f$  meson. Under the assumption of factorization individually for both pomeron and reggeon exchange, the observed diffractive structure function can be expressed as

$$F_2^{D(3)} = f_{\mathbb{P}/\mathbb{P}}(x_{\mathbb{P}})F_2^{\mathbb{P}}(\beta, Q^2) + f_{\mathbb{R}/\mathbb{P}}(x_{\mathbb{R}})F_2^{\mathbb{R}}(\beta, Q^2), \quad (1.27)$$

where now  $f_{\mathbb{R}/\mathbb{P}}(x_{\mathbb{R}})$  describes the reggeon flux and  $F_2^{\mathbb{R}}(\beta, Q^2)$  the reggeon structure function. Using this Regge parameterization, a fit to the H1 data yields for the pomeron an intercept of

$$\alpha_{\mathbb{P}}(0) = 1.203 \pm 0.020(stat.) \pm 0.013(sys.)_{-0.035}^{+0.030}(model). \quad (1.28)$$

This value of  $\alpha_{\mathbb{P}}(0)$  is significantly larger than the value obtained from soft hadronic cross section measurements. The meson intercept is found to be consistent with the value of 0.55. The  $t$  dependence of the trajectories cannot be constrained in the fit and so are assumed to be the same as those obtained from analyses of hadron-hadron data.

In the factorization hypothesis of Equation 1.27 the structure functions  $F_2^{\mathbb{P}}(\beta, Q^2)$  and  $F_2^{\mathbb{R}}(\beta, Q^2)$  describe the deep-inelastic structure of the pomeron and meson exchanges respectively. The  $Q^2$  evolution of the pomeron structure function  $F_2^{\mathbb{P}}(\beta, Q^2)$  may be understood in terms of parton dynamics and therefore perturbative QCD. In analogy with the proton structure function  $F_2$ , the pomeron structure function can be written as

$$F_2^{\mathbb{P}}(\beta, Q^2) = \beta \sum_i e_i^2 f_i(\beta, Q^2), \quad (1.29)$$

where  $f_i(\beta, Q^2)$  is the parton density function giving the probability of finding a parton of type  $i$  and charge  $e_i$  carrying the fraction  $\beta$  of the pomeron's momentum. Models which treat the pomeron as though it were a hadron composed of partons are referred to as *factorizable* or *resolved* pomeron models. H1 adopted a simple prescription [25] in which parton distributions are assigned to both the pomeron and meson and are parameterized in terms of non-perturbative input distributions at a starting scale  $Q_0^2 = 3 \text{ GeV}^2$ . The pomeron and meson parton distributions are then evolved separately with increasing  $Q^2$  according to the DGLAP formalism (see Section 1.2.2). For the pomeron, the input distributions are parameterized using a quark flavor singlet distribution ( $z\mathcal{F}_q(z, Q^2) = u + \bar{u} + d + \bar{d} + s + \bar{s}$ ) and a gluon distribution ( $z\mathcal{F}_g(z, Q^2)$ ), where  $z$  is the fractional momentum of the pomeron carried by the struck parton. If the photon couples directly to a quark intrinsic to the pomeron structure then  $z = \beta$ , whilst if the photon interacts with a gluon via photon-gluon fusion then  $z$  is the fractional momentum carried by the gluon and the inequation  $0 < \beta < z$  holds.

The measurement is confronted with three calculations assuming different initial forms for the pomeron parton distributions. In fit 1 only quarks are assumed to contribute to the pomeron structure at the starting scale. The resulting parameterization of  $F_2^{D(3)}$  is shown

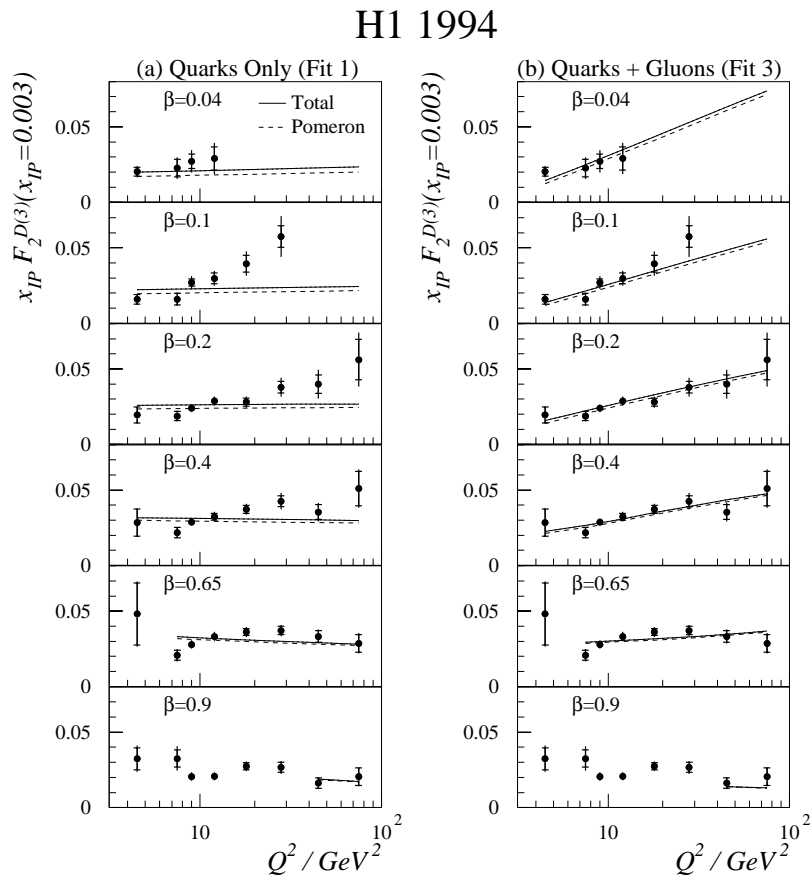


**Figure 1.7:** The quantity  $x_P F_2^{D(3)}(x_P, \beta, Q^2)$  at  $x_P = 0.003$  as a function of  $Q^2$  for different values of  $\beta$ . In both (a) and (b) the solid points show the same data. In (a) the result of QCD fit 1 (in which only quarks contributed to the pomeron structure at  $Q_0^2 = 3 \text{ GeV}^2$ ) is superimposed. In (b) the preferred QCD fit 3 (in which both quarks and gluons contribute) is shown. In both figures the solid line represents the value of  $F_2^{D(3)}(x_P, \beta, Q^2)$ , whilst the dotted line shows the contribution from the pomeron term only.

at a constant value of  $x_P = 0.003$ , where pomeron exchange is expected to dominate, as a function of  $Q^2$  for different values of  $\beta$  in Figure 1.7(a), and as a function of  $\beta$  for different values of  $Q^2$  in Figure 1.8(a). A scaling violation of  $F_2^{D(3)}$  is observed which is not described by a parameterization in which the pomeron contains only quarks. In fit 2 gluons are allowed to contribute to the pomeron structure at the starting scale, and a significantly better description of the data is obtained. Introducing two further terms in a polynomial expansion of the gluon distribution improves further the description of the data. The corresponding fit 3 is shown in Figures 1.7(b) and 1.8(b), and reproduces well the scaling violations of  $F_2^{D(3)}$  in  $Q^2$  and the dependence on  $\beta$ .

The parton distributions resulting from fits 2 and 3 are presented in Figure 1.9 where both the sum of the light quarks distributions and the gluon distribution are shown for

## H1 1994

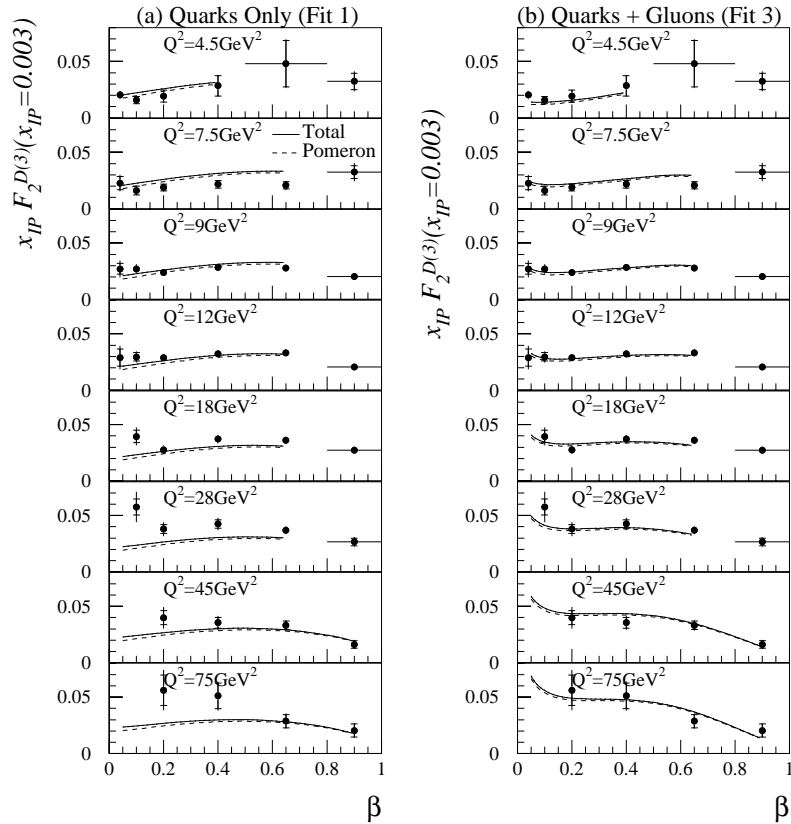


**Figure 1.8:** The quantity  $x_p F_2^{D(3)}(x_p, \beta, Q^2)$  at  $x_p = 0.003$  as a function of  $\beta$  for different values of  $Q^2$ . In both (a) and (b) the solid points show the same data. In (a) the result of QCD fit 1 (in which only quarks contributed to the pomeron structure at  $Q_0^2 = 3 \text{ GeV}^2$ ) is superimposed. In (b) the preferred QCD fit 3 (in which both quarks and gluons contribute) is shown. In both figures the solid line represents the value of  $F_2^{D(3)}(x_p, \beta, Q^2)$ , whilst the dotted line shows the contribution from the pomeron term only.

each fit for three different values of  $Q^2$ . In both fits a substantial gluon component in the pomeron is observed. The fraction of the momentum of the pomeron carried by gluons decreases with increasing  $Q^2$  from  $\sim 90\%$  at  $Q^2 = 4.5 \text{ GeV}^2$  to  $\sim 80\%$  at  $Q^2 = 75 \text{ GeV}^2$ . These results are consistent with a qualitative conclusion which may be drawn directly from Figure 1.7. The rise of the diffractive structure function  $F_2^{D(3)}$  with  $\ln Q^2$  at fixed  $\beta$ , persists to large values of  $\beta = 0.65$ . This is in contrast to the structure function of the proton  $F_2$  and is a clear evidence of the diffractive exchange being dominated by gluons. With the slightly better quality of fit 3 the data seem to prefer a gluon distribution that is large at high  $z$  such that for low values of  $Q^2$  the majority of the pomeron momentum is carried by a single gluon. Thus the data support pictures of diffractive DIS in which the dominant mechanism is boson-gluon fusion with the incoming gluon carrying a large fraction of the momentum of the pomeron.

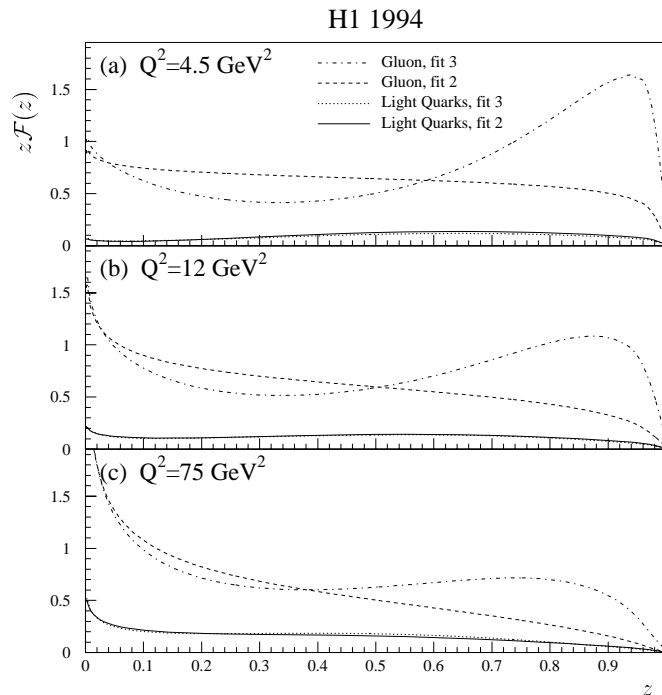


**Figure 1.9:** The contribution of the light quark and gluon distributions to  $z\mathcal{F}(z)$  for QCD fits 2 and 3 at (a)  $Q^2 = 4.5 \text{ GeV}^2$ , (b)  $Q^2 = 12 \text{ GeV}^2$  and (c)  $Q^2 = 75 \text{ GeV}^2$ .

The H1 parton distributions from fits 1 to 3 described above are implemented in a factorizable pomeron model within the RAPGAP Monte Carlo program [26].

## 1.5 Charm in diffraction

As it has been discussed in the previous section the pomeron can be interpreted as a partonic object. The QCD analysis of the inclusive diffractive structure function  $F_2^{D(3)}$  indicates a significant gluon content in the pomeron. In analogy to inclusive open charm production (see Section 1.3) the study of diffractive open charm production allows one to probe more directly the gluon content in the pomeron. The models later used for comparison are briefly introduced in the following.

### 1.5.1 Resolved pomeron model

In the resolved pomeron model [28] open charm is produced via photon-gluon fusion (PGF), where the photon, radiated by the incoming lepton, interacts with a gluon of the pomeron, carrying a fraction  $z_P$  of the pomeron momentum. The generic diagram for this process is shown in Figure 1.10. The momentum fraction of the pomeron carried by

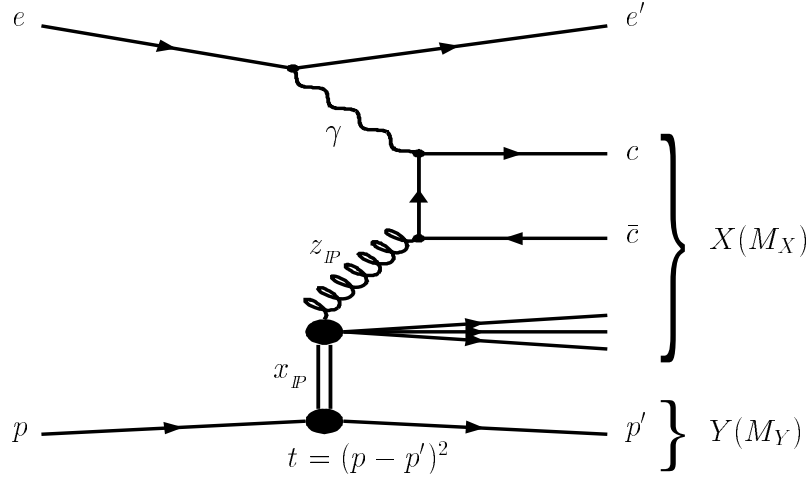


**Figure 1.10:** Photon-gluon fusion in the resolved pomeron process.  $z_P$  denotes the fraction of the pomeron momentum carried by the gluon.

the interacting gluon which enters the photon-gluon fusion process (PGF)  $z_P$  is given by

$$z_P = \frac{x_g}{x_P} = \beta \left( 1 + \frac{\hat{s}}{Q^2} \right) \simeq \frac{M_{c\bar{c}}^2 + Q^2}{M_X^2 + Q^2}, \quad (1.30)$$

see also Equation 1.18.  $z_P$  can be reconstructed from the measured hadronic final state according to Equation 1.14 and 1.15 defining the hadronic observable  $z_P^{obs}$ . In the resolved pomeron process both the  $c\bar{c}$  system and the pomeron remnant are included in the system  $X$  giving rise to the production of masses  $M_X \gg M_{c\bar{c}}$ . Therefore the gluon momentum fraction  $z_P$  is dominated by low values.

Diffractive charm production can be simulated in the resolved pomeron approach using the Monte Carlo event generator program RAPGAP. The partons emerging from the hard sub-process are hadronizing according to the LUND string model, as implemented in the JETSET [27] Monte Carlo program.

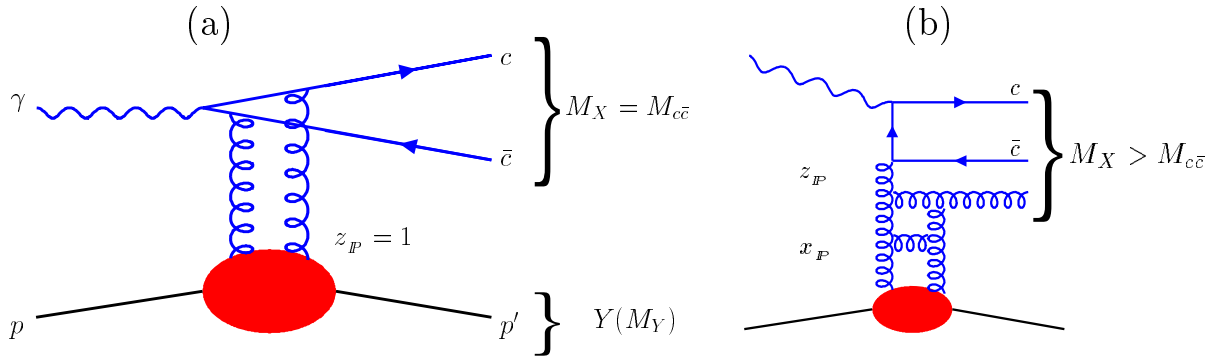


**Figure 1.11:** Diffractive open charm production by perturbative two gluon exchange. a) process  $\gamma^* + p \rightarrow c\bar{c} + p'$  where the mass of system  $X$  is restricted to the invariant mass of the  $c\bar{c}$  system. b) higher order process  $\gamma^* + p \rightarrow c\bar{c}g + p'$ .

### 1.5.2 Two-gluon model

In perturbative QCD diffractive open charm production can be realized by the exchange of two hard gluons [29, 30, 31] (see Figure 1.11(a)). Consequently the cross section for the process  $\gamma^* + p \rightarrow c\bar{c} + p'$  is proportional to the gluon density squared of the proton  $[x_p G_p(x_p, \mu)]^2$ , where  $\mu$  is the factorization scale. This process is implemented in the Monte Carlo generator RAPGAP allowing for different parameterizations of the gluon density in the proton.

In the two-gluon model  $z_p = 1$  holds for the partonic final state since the mass of system  $X$  is restricted to the invariant mass  $M_{c\bar{c}}$  of the  $c\bar{c}$  system. To produce higher masses  $M_X$  contributions such as  $\gamma^* + p \rightarrow c\bar{c}g + p'$  are needed, as it is indicated in Figure 1.11(b).

### 1.5.3 Soft color interaction model

In the soft color interaction model (SCI) [32] the  $c\bar{c}$  pair is produced via PGF. With a certain probability the color structure of the partonic state is changed by soft gluon exchanges between each pair of colored partons emerging from the hard interaction, without changing the kinematics of the process (see Figure 1.12). Large rapidity gap events can be produced when the soft interactions lead to net color-singlet exchange. The probability for SCI is a free parameter in this model. Since gluon radiation from the  $c\bar{c}$  pair is suppressed by the large charm mass the mass  $M_X$  of the system  $X$  is relatively small. The SCI has been implemented in the Monte Carlo generator AROMA 2.2.

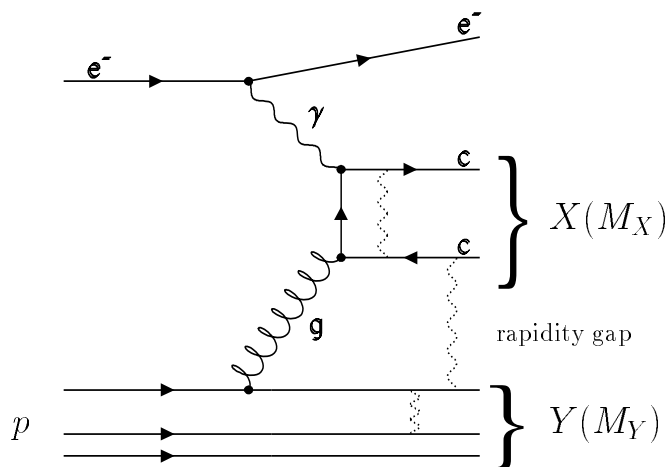


**Figure 1.12:** Charm production via photon-gluon fusion. A rapidity gap is produced via soft color interactions between the outgoing partons of the hard sub-process.

### 1.5.4 Monte Carlo implementation

The **AROMA** Monte Carlo program [33] describes the charm production process  $ep \rightarrow ec\bar{c}X$  via the photon-gluon fusion mechanism. The hard partonic subprocess  $\gamma g \rightarrow c\bar{c}$  is calculated in leading order QED and QCD. Higher order corrections are included by

initial and final state parton showers in the leading log approximation [34]. The gluon density of the proton  $g(x_g, \mu^2)$  is considered at a factorization scale given by the center of mass energies of the partonic interaction  $\mu^2 = \hat{s}$ . The hadronization is performed using the LUND string model. Rapidity gaps are produced with a rate of  $\approx 10\%$  through soft color interactions, without involving the concept of a pomeron.

The **RAPGAP** Monte Carlo program [26] produces charm in the same way as it is performed in AROMA, namely via PGF. Also hadronization is done using the LUND string model. The difference to AROMA is the construction of the partonic final state involving either the concept of the resolved pomeron or the two-gluon model, which both have been discussed in detail in the previous sections.

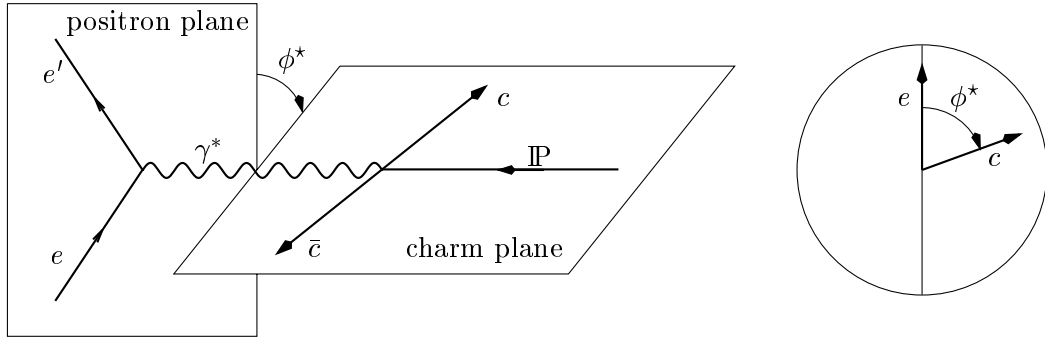


**Figure 1.13:** Definition of the azimuthal angle  $\phi^*$  in the  $\gamma^*\mathbb{P}$  center of mass system.

### 1.5.5 Model comparison

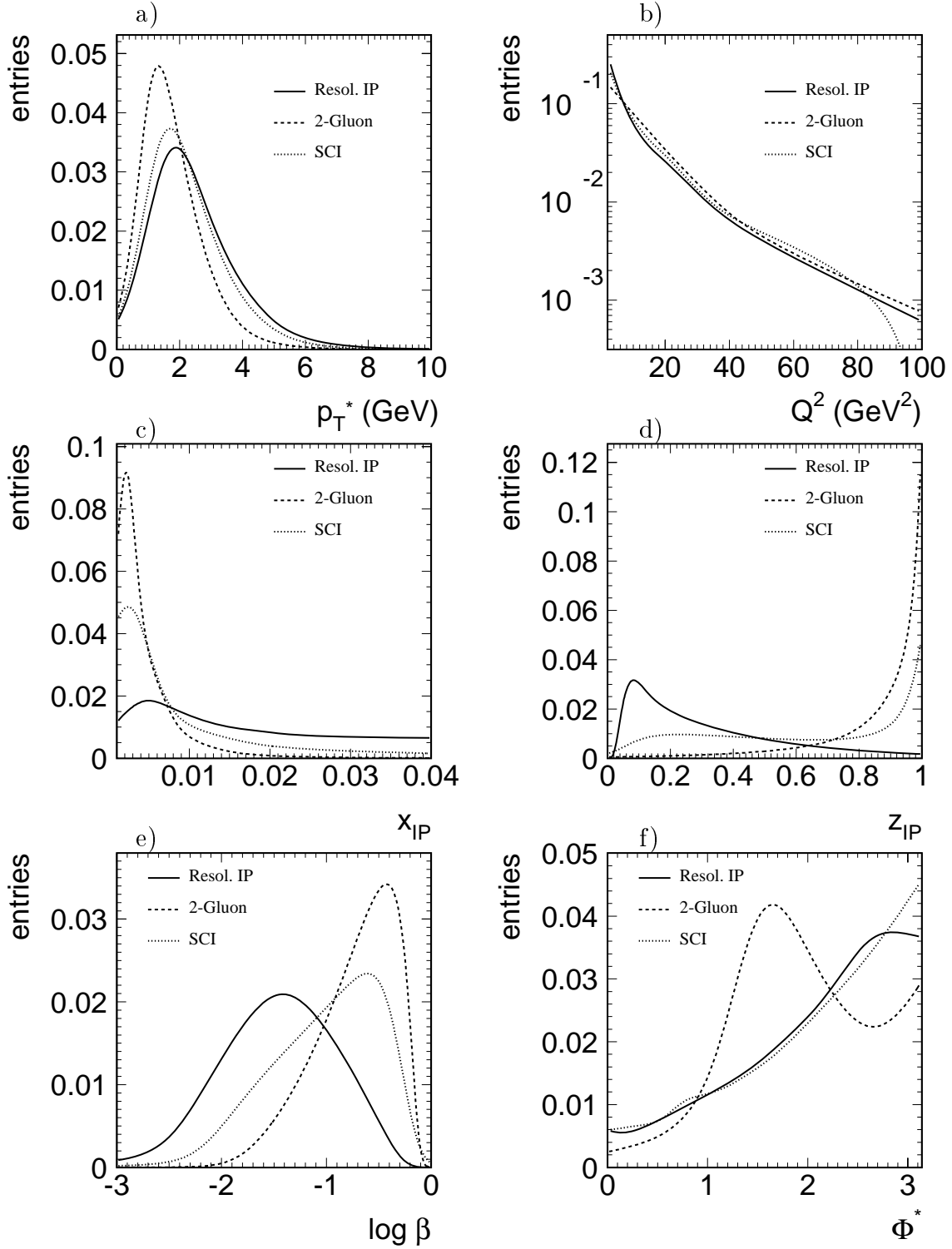
A comparison of the three different models for diffractive  $c\bar{c}$  production is presented in Figure 1.14. Shown are the parton level predictions for various kinematic variables in the kinematic region  $2 < Q^2 < 100 \text{ GeV}^2$ ,  $0.05 < y < 0.7$ ,  $p_T > 2 \text{ GeV}$ ,  $|\eta| < 1.5$ ,  $x_p < 0.04$ ,  $M_V < 1.6 \text{ GeV}$  and  $|t| < 1 \text{ GeV}^2$  where the cross section measurement, which is presented in Chapter 4, is performed. For the resolved pomeron model QCD fit 2 to  $F_2^{D(3)}$ , which is dominated by gluons at the starting scale, is used (see Figure 1.9). Pomeron and reggeon exchange is considered. A factorization scale  $\mu^2 = p_T^2 + Q^2 + 4m_c^2$ , a QCD scale  $\Lambda_{QCD} = 0.25$  and a number of active flavors  $N_f = 5$  in the first order expression of  $\alpha_s$  are chosen for both the resolved pomeron and the two-gluon model. For the SCI model  $\mu^2 = \hat{s}$ ,  $\Lambda_{QCD} = 0.2$  and  $N_f = 4$ . The gluon density within the proton is modelled by a leading order GRV<sup>6</sup> parameterization [36]. For all models a charm quark mass of  $m_c = 1.5 \text{ GeV}$  is used.

Figure 1.14(a) shows the  $p_T^*$  distribution where  $p_T^*$  is the transverse momentum of the charm quark in the  $\gamma^*\mathbb{P}$  center of mass system. The  $p_T^*$  spectrum predicted by the two-gluon model is softer compared to the predictions of the resolved  $\mathbb{P}$  and the SCI model, which are very similar. The  $Q^2$  spectra, plotted in Figure 1.14(b), are more or less equal over the full kinematic range. The predictions for the  $x_p$  distribution can be seen in

<sup>6</sup>Glück, Reya, Vogt

Figure 1.14(c) and shows a moderate increase with decreasing values of  $x_p$ . The curve peaks at  $\approx 0.005$  reflecting the fact that the colorless exchange is predominantly ( $\mathcal{O}(90\%)$ ) mediated by pomerons in the measured range. The two-gluon and the SCI model predict a strong peak at low values of  $x_p$  due to the fact that the system  $X$  in both models predominantly consists of the  $c\bar{c}$  system alone. Since the momentum fraction of the pomeron carried by the interacting gluon  $z_p$  is approximately given by the ratio  $M_{c\bar{c}}/M_X$  (see Equation 1.30) the  $z_p$  distribution peaks towards high values, see Figure 1.14(d). In contrast the resolved  $\mathbb{P}$  model predicts a distribution dominated by low values. The system  $X$  consists of the  $c\bar{c}$  pair and the pomeron remnant (see Figure 1.10) and therefore masses much larger than  $M_{c\bar{c}}$  can be produced. This is also visible in Figure 1.14(e) where the  $\beta$  distribution is plotted. A shift towards lower values of  $\beta$  can be observed compared to the curves predicted by the two-gluon and the SCI model. Finally the  $\phi^*$  distribution is shown in Figure 1.14(f), where  $\phi^*$  denotes the absolute value of the angle between the positron scattering plane and the  $c\bar{c}$  plane in the  $\gamma^*\mathbb{P}$  center of mass system, see Figure 1.13. In the two-gluon model the charm quarks are preferably produced in the plane perpendicular to the positron scattering plane.

In conclusion, the comparison shows striking differences, reflecting the different dynamics of the models. This holds in particular for the variable  $z_p$ , which combines the kinematic informations from the scattered positron, the hadronic system  $X$  and the charmed meson (see Section 1.5.1 and Equation 1.30). This observable directly probes the gluons taking part in the interaction. Despite the presence of parton shower and fragmentation effects the characteristics of the different processes are clearly visible. Thus one should gain some insight into the mechanism of diffractive charm production already with a low statistics measurement.



**Figure 1.14:** Predictions for diffractive charm production in the kinematic range  $2 < Q^2 < 100 \text{ GeV}^2$ ,  $0.05 < y < 0.7$ ,  $p_T > 2 \text{ GeV}$ ,  $|\eta| < 1.5$ ,  $x_p < 0.04$ ,  $M_\gamma < 1.6 \text{ GeV}$  and  $|t| < 1 \text{ GeV}^2$  for the resolved IP model (solid line), the 2-gluon model (dashed line) and the SCI model (dotted line). The distributions are normalized such that the sum of the entries equals one.

# Chapter 2

## The H1 Detector at HERA

The work presented here is an analysis of data from  $e^+p$  collisions in HERA<sup>1</sup>, at the DESY<sup>2</sup> laboratory in Hamburg. The data were collected with the H1 detector, a general purpose detector with almost full coverage of the solid angle around the  $e^+p$  interaction point. This apparatus is a composition of several detector components which are optimized for the measurement of various physical quantities. In the following the various components relevant for the present analysis are described. A detailed description of the H1 detector can be found in [37].

<sup>1</sup>HERA=Hadron Electron Ring Accelerator

<sup>2</sup>DESY=Deutsches Elektronen Synchrotron

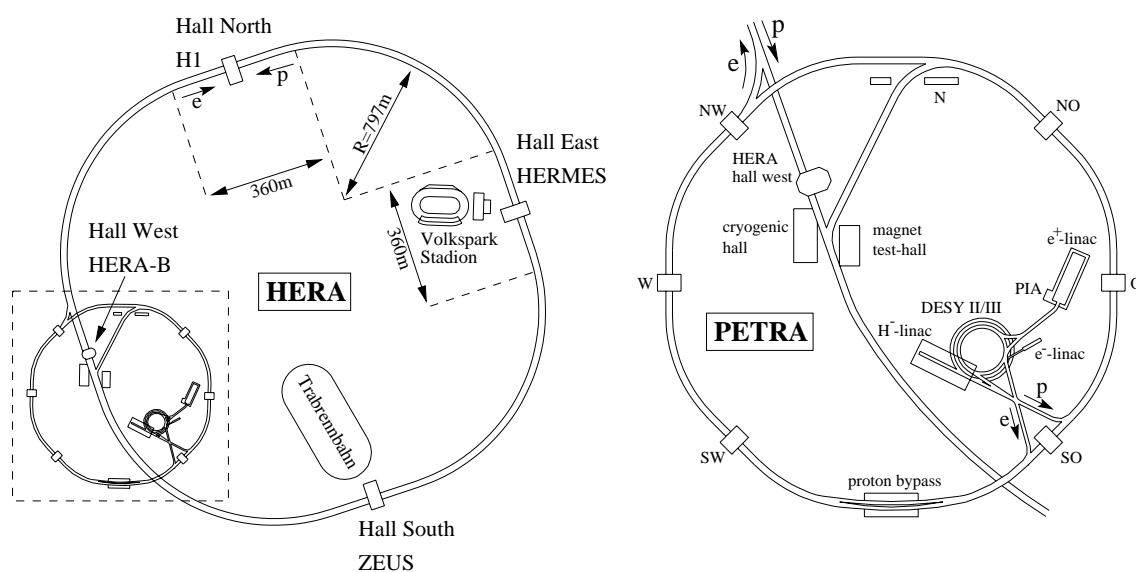
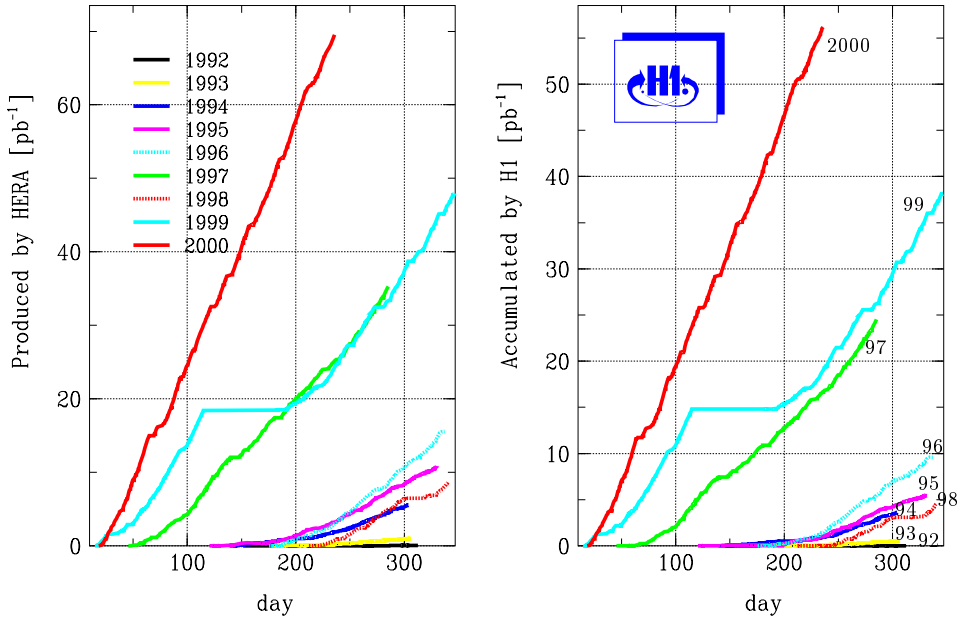


Figure 2.1: The storage ring HERA and its pre-accelerators at DESY.



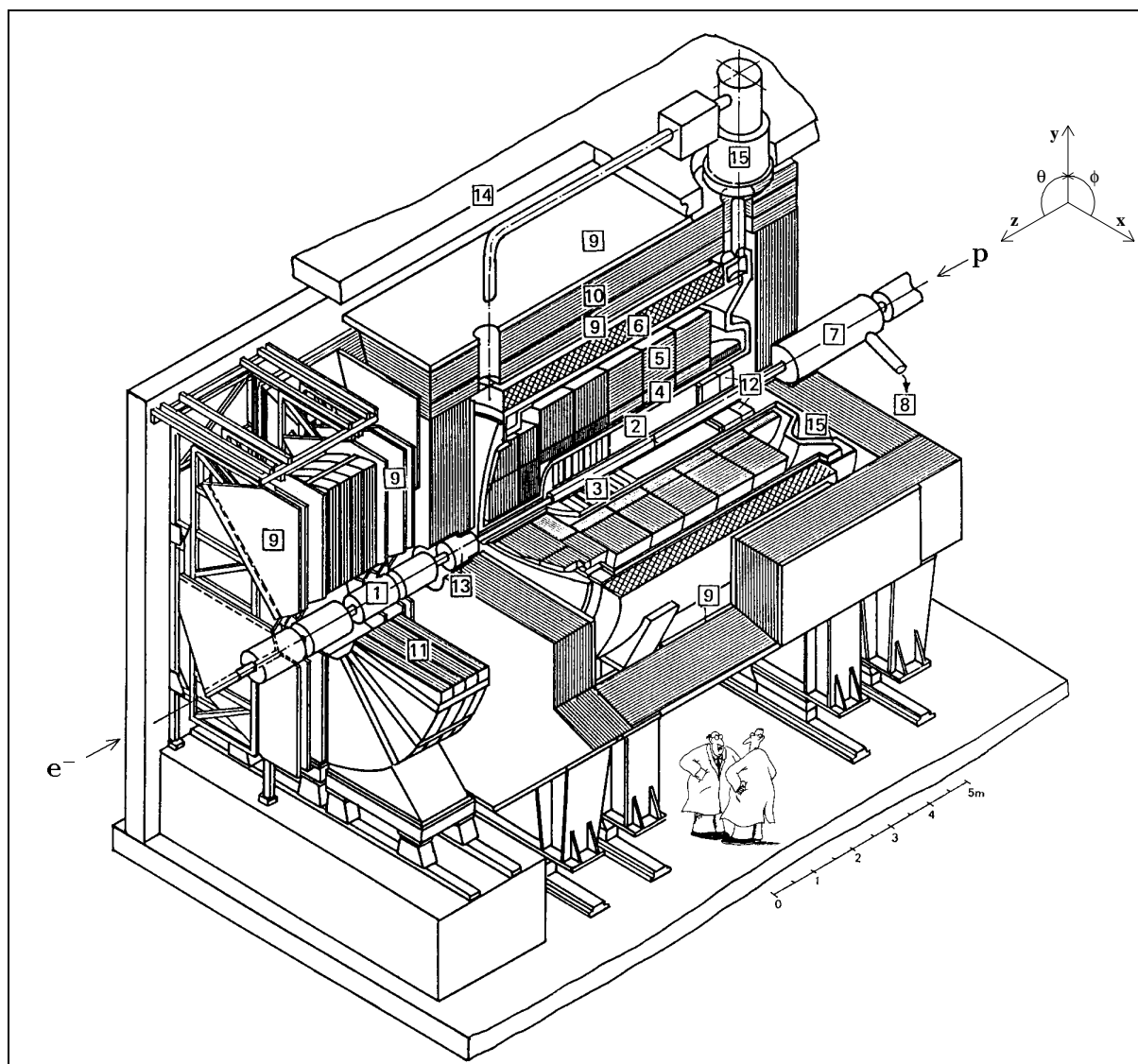
**Figure 2.2:** *Integrated luminosity produced by HERA and measured in H1 for the years 1992-2000.*

## 2.1 The HERA positron-proton collider

The HERA particle collider is the first and so far unique example of the usage of a storage ring in the study of  $ep$  collisions. A schematic overview is shown in Figure 2.1. In a tunnel with a total circumference of 6.4 km, a proton beam and a positron beam are accelerated separately up to energies of 820 GeV and 27.6 GeV, respectively. Once the beams have reached their final energies, they are adjusted to collide at zero crossing angle in the interaction regions of the H1 and ZEUS experiments. The center of mass energy of  $\sqrt{s} \simeq 300$  GeV is one order of magnitude larger than the energies achieved in fixed target lepton nucleon scattering experiments. The positron and proton beams are not continuous, but consist of bunches located 96 ns apart, corresponding to a bunch crossing frequency of 10.4 MHz. A smaller number of non-colliding bunches (*pilot bunches*) is used to study background induced by interactions of the beam with the residual gas in the beam pipe, or with its wall. In 1998 and the first run period of 1999 electrons were used in place of positrons. After the 1999 summer shutdown HERA continued with positron-proton collisions. For the analysis presented here only positron-proton data, collected with the H1 detector over the years 1995, 1996 and 1997, are used. The integrated luminosity produced in the years 1992 to 2000 is shown in Figure 2.2. The rise of the beam currents and HERA performance during the last years is clearly visible.

## 2.2 The H1 detector

The H1 detector is a typical multi-purpose detector consisting of several sub-detectors, which are generally optimized for the measurement of a specific physical quantity. The



- |    |  |    |                                     |
|----|--|----|-------------------------------------|
| 1  | Beam pipe and beam magnets                                 | 2  | Central tracking chambers           |
| 3  | Forward tracking chambers                                  |    |                                     |
| 4  | Electromagnetic calorimeter (lead/liquid argon)            |    |                                     |
| 5  | Hadronic calorimeter (steel/liquid argon)                  |    |                                     |
| 6  | Superconducting coil ( $B = 1.15$ T)                       | 7  | Compensating magnet ( $B = 4.83$ T) |
| 8  | Helium cryogenics  | 9  | Muon chambers                       |
| 10 | Instrumented iron (iron slabs and streamer tube detectors) |    |                                     |
| 11 | Muon toroid magnet ( $B = 1.6$ T)                          |    |                                     |
| 12 | Backward drift chamber and calorimeter ( <i>Spa Cal</i> )  |    |                                     |
| 13 | Plug calorimeter   | 14 | Concrete shielding                  |
| 15 | Liquid argon cryostat                                      |    |                                     |

**Figure 2.3:** Overview of the H1 detector. The H1 coordinate system is indicated in the upper right corner.

proton beam energy is significantly larger than the positron beam energy and leads to a boosted final state in the proton direction. Therefore this region, that is often referred to as the *forward* region, is more extensively instrumented than the *backward* region. The proton direction defines the  $z$ -axis of the right handed H1 coordinate system with its origin at the nominal interaction point. The  $x$ -axis points towards the center of the HERA ring and the  $y$ -axis is pointing upwards. The polar angle is  $\theta = 0^\circ$  in proton beam direction and  $\theta = 180^\circ$  in positron beam direction. The azimuth angle  $\phi$  extends from the positive  $x$ -axis to positive values for the upper detector half up to  $180^\circ$  and up to  $-180^\circ$  for the lower half.

A schematic view of the H1 detector is shown in Figure 2.3. The interaction region within the beam pipe [1] is surrounded by the tracking system which consists of a central [2] and a forward [3] part. The Liquid-Argon calorimeter (LAr) made up of electromagnetic [4] and hadronic sections [5] encloses the tracking system. In the backward region it is completed by a scintillating fibre calorimeter (SpaCal) [12]. A backward drift chamber (BDC) is located in front of the SpaCal. These two components are mainly designed to measure the scattered positron. A super-conducting coil [6] surrounding the calorimeters provides a homogeneous magnetic field of 1.12T. The iron return yoke [10] contains layers of streamer tubes [9] to measure the tails from hadronic energy showers and to identify muons. In the forward direction muons are measured by six layers of drift chambers [9], three on either side of the toroid magnet [11]. In the forward region a copper/silicon calorimeter (PLUG) [13] is embedded in the iron yoke. For the precise measurement of charged particles a Central Silicon Detector (CST) was installed in 1996 around the interaction vertex. In 1997 it was supplemented by the Backward Silicon Detector (BST) which measures the scattered positron.

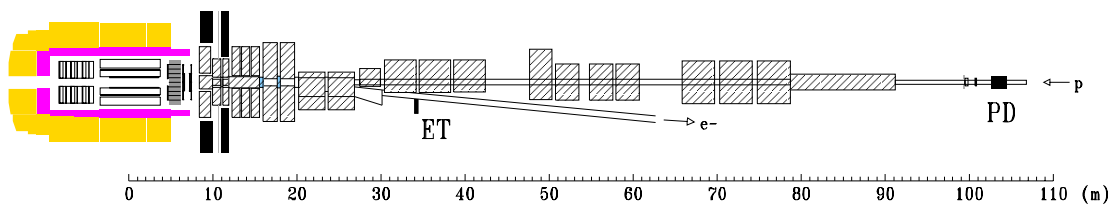


**Figure 2.4:** The H1 luminosity system, consisting of an electron tagger at  $z = -33$  m and a photon detector at  $z = -103$  m.

### 2.2.1 Time-of-flight system

The time-of-flight system (ToF) works on the principle that the time of arrival of particles from  $ep$  interactions, at a particular point in the detector, differs from that of particles from outside the vertex region. Therefore, the precise timing information of scintillators mounted around the beam pipe at both ends of the detector allows a powerful rejection of particles from beam induced background events.

### 2.2.2 Luminosity measurement

The luminosity at H1 is determined from the rate of Bethe-Heitler-Bremsstrahlung events  $ep \rightarrow ep\gamma$ . The cross section for this process can be calculated in QED with high precision. The scattered positron as well as the outgoing photon are measured simultaneously in the Electron Tagger (ET) at  $z = -33$  m and the Photon Detector (PD) at  $z = -103$  m (Figure 2.4). Background events, mainly arising from bremsstrahlung of the positron interacting with the residual gas in the beam pipe, can be subtracted using pilot bunches, thus the luminosity is given by

$$\mathcal{L} = \frac{R_{tot} - (I_{tot}/I_0)R_0}{\sigma_{vis}}, \quad (2.1)$$

where  $R_{tot}$  is the measured total rate of bremsstrahlung processes,  $R_0$  the measured bremsstrahlung rate in the pilot bunches,  $I_{tot}/I_0$  the ratio of the corresponding beam currents and  $\sigma_{vis}$  the visible part of the Bethe-Heitler cross section.

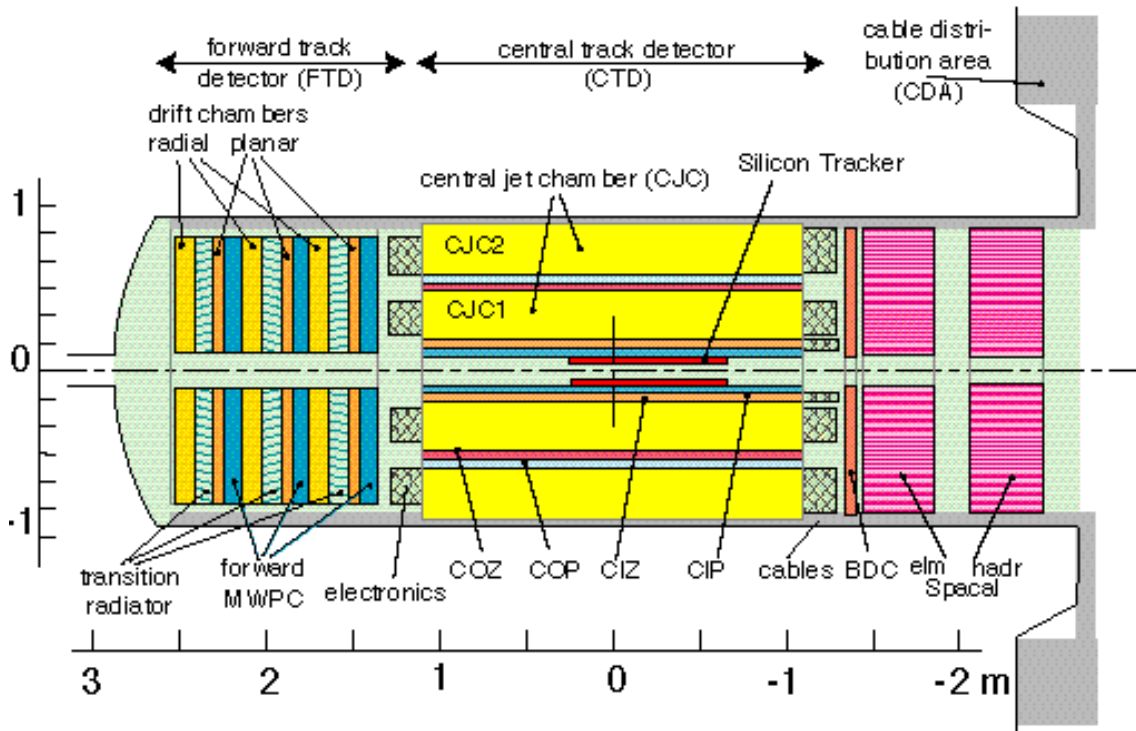


**Figure 2.5:** Schematic side view of the tracking system. in addition to the forward track detector (FTD) and the central track detector (CTD) the backward calorimeter SpaCal is also shown.

### 2.2.3 The central tracking detector

The tracking chambers are mounted cylindrically around the beam pipe and the silicon detectors in two radial layers of proportional chamber - z-chamber - jet chamber. It is

designed to measure the momenta and angles of charged particles and to provide a fast trigger signal. A side and radial view of the central tracking system is shown in Figures 2.5 and 2.6. The geometrical acceptance for the different components is given in Table 2.1.

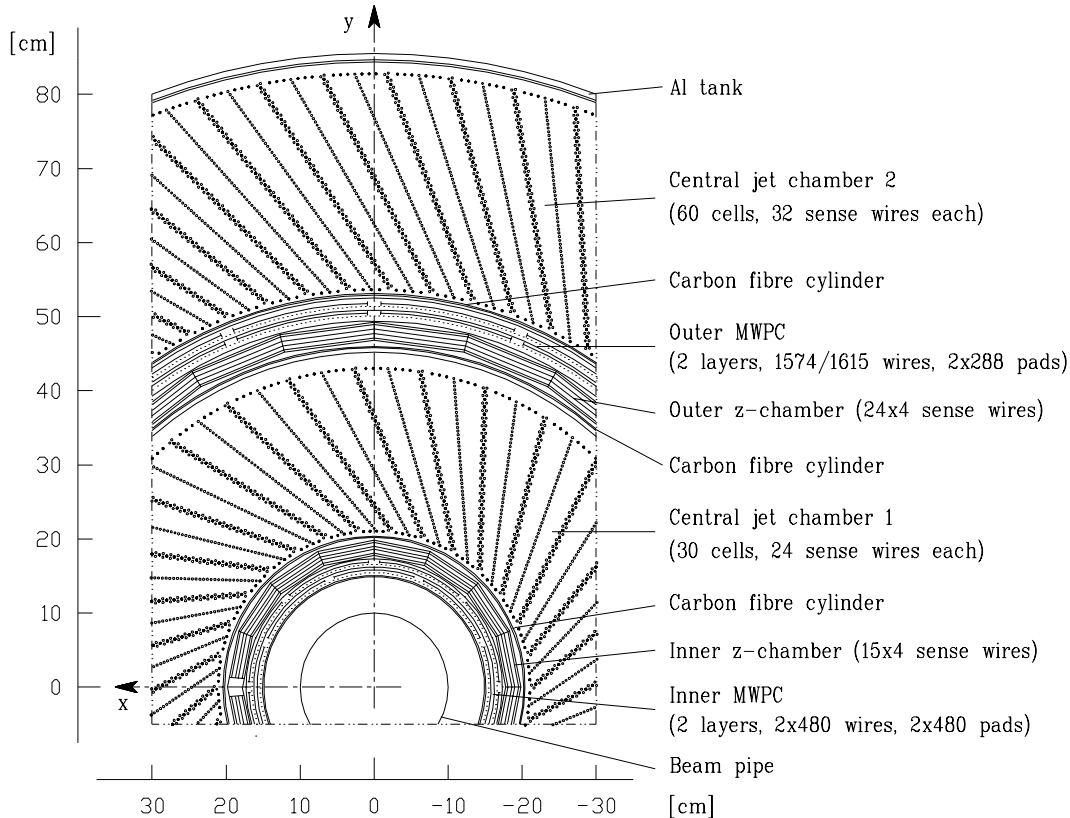


**Figure 2.6:** Schematic radial view of the central tracking detector CTD, showing the inner and outer z-drift chambers, the inner and outer multi-wire proportional chambers and the two jet chambers in detail.

### Central jet chamber

The central jet chamber is the main component of the tracking device. It was designed to measure charged particle track momenta with high precision. The two cylindrical, coaxial volumes (CJC1 and CJC2) consist of wire planes parallel to the beam axis. In azimuthal direction the CJC1 is subdivided in 30 cells each with one wire plane of 24 sense wires. The CJC2 is designed similarly but has 60 cells and 32 sense wires per cell. Each anode sense wire plane has two adjacent cathode planes shaping the drift field. The tilt of the drift cells of about  $30^\circ$  compensates for the Lorentz angle and leads to a drift direction that is almost perpendicular to a high momentum track originating from the vertex. This allows for an optimal track resolution and also helps to resolve the ambiguity introduced by wrong *mirror* track segments. A further advantage is that high momentum tracks cross at least one sense wire plane in CJC1 and CJC2. The passing time of a particle can be determined to an accuracy of  $\approx 0.5$  ns and tracks from different bunch crossings can

easily be separated.

With the jet-chamber a single hit resolution of  $\sigma_{r\phi} \approx 140 \mu\text{m}$  in the  $r\phi$ -plane is obtained and the momentum resolution is given by  $\sigma_p/p^2 \approx 6 \times 10^{-3} \text{GeV}^{-1}$  [39]. The resolution of the  $z$ -coordinate  $\sigma_z$ , measured by charge division, is  $\approx 22 \text{mm}$  or larger, depending on  $\theta$  and the energy loss  $dE/dx$ , and is thus about two orders of magnitude worse than the  $r\phi$ -resolution. The hit signals are the basis for the track finding and reconstruction, see Section 2.2.4.

### Central $z$ -chambers

The central inner and outer  $z$ -chambers (CIZ, COZ) are drift chambers with wires strung concentrically and perpendicular around the beam axis. The cross section of CIZ forms a 16-edge- and that from the COZ a 24-edge-polygon. The CIZ (COZ) is subdivided into 15 (24) rings in  $z$  with each ring having four wires. No wire staggering is implemented. The wires are read out at both ends, and the  $\phi$ -coordinate is obtained through charge division. The single hit resolution in  $z$  is of the order of  $\sigma_z = 380 \mu\text{m}$ . A detailed description of the CIZ can be found in [40, 41, 42] and in [43] for the COZ.

	Radial		$z$		Polar	
	min [cm]	max [cm]	min [cm]	max [cm]	min [°]	max [°]
CST	5.75	9.5	-17.5	17.5	30	150
CIZ	17.4	20.0	-108.0	72.0	13.6	170.8
CJC1	20.3	45.1	-112.5	107.5	10.7	169.7
COZ	46.0	48.5	-110.5	105.5	23.6	157.3
CJC2	53.0	84.4	-112.5	107.5	26.3	154.7

**Table 2.1:** Active regions of the central tracking chambers.

### Central proportional chambers

The central proportional chambers CIP (inner) and COP (outer) are multi-wire proportional chambers (MWPC). They deliver a fast timing signal which is used to separate between two consecutive HERA bunch crossings. Both chambers consist of an inner and outer layer with starting radii of the inner layers at  $\approx 15 \text{cm}$  for the CIP and  $\approx 50 \text{cm}$  for the COP. The cathodes of the CIP (COP) are 8- (16-) fold segmented in  $\phi$ . The active length of the CIP (COP) in  $z$  is  $-112.5 \text{cm} \leq z \leq 106.5 \text{cm}$  ( $-110.7 \text{cm} \leq z \leq 106.5 \text{cm}$ ) subdivided into 60 (18) pads. The signals of these pads are read out and fed into the  $z$ -vertex trigger logic, see Section 2.2.8.

### Central silicon detector

The central silicon detector CST [45, 46] has been built to provide vertex information from precision measurements of charged particle tracks close to the interaction point. It

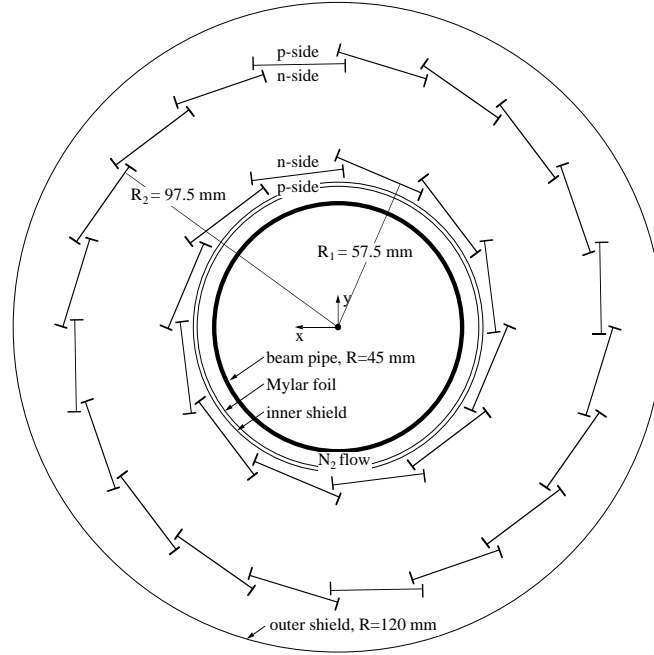


**Figure 2.7:** CST geometry in the  $r\phi$ -plane.

has been fully operational since the beginning of 1997. The CST consists of two radial layers composed from 12 and 20 faces at radii of 5.75 cm and 9.75 cm, respectively, as shown in Figure 2.7. One face or *ladder* consists of six silicon sensors and aluminium nitride hybrids at each end. The ladders in a layer are shifted tangentially with respect to each other leading to an overlap of adjacent active areas in  $r\phi$ . The detector is centered around the nominal interaction point and has an active length in  $z$  of 35.6 cm for both layers, thus covering a large fraction of the interaction region, see Table 2.1. The CST is built of double-sided, silicon strip detectors allowing for a precise measurement in the  $r\phi$ -plane as well as in  $z$ . The high resolution in  $r\phi$  is delivered by the p-side of the detector where the strips are located parallel to the  $z$ -axis. On the n-side the strips are perpendicular to the  $z$ -axis, thus measuring  $z$ . The intrinsic resolution can be derived from distributions, that are often referred to as *overlap-residuals*, plotting the distance between hits and tracks in the overlap regions. The intrinsic hit resolution obtained from such distributions is  $12\ \mu\text{m}$  in the  $r\phi$ -projection. In  $z$ , the resolution is parabolically correlated with the angle of incidence of the charged particle and reaches a minimum of  $22\ \mu\text{m}$  at about  $15^\circ$  from normal incidence [47]. For the combined CJC-CST tracks a *dca*-resolution (see next section) of  $\approx 42\ \mu\text{m}$  is obtained [48].

## 2.2.4 Track finding and reconstruction

The central track reconstruction algorithm at H1 exists in two versions running at different speeds. A fast version is applied and the result is used on trigger level L4 (see Section 2.2.8), where an efficient background recognition and classification of physics events is provided. A standard version is performed on L5 (see Section 2.2.8) as a part of

Track parameter		Unit	Value range
Curvature (inverse radius)	$\kappa$	cm <sup>-1</sup>	$-\infty \dots + \infty$
Closest distance to origin	$dca$	cm	$-\infty \dots + \infty$
Azimuthal angle at $dca$	$\phi$	rad	$-\pi \dots + \pi$
Polar angle at $dca$	$\theta$	rad	$0 \dots \pi$
Z-axis intercept at $dca$	$z_0$	cm	$-\infty \dots + \infty$

**Table 2.2:** Helix parameters describing a track

the full track reconstruction. It makes use of the results of the fast version but is about a factor of ten slower with respect to computing time. The goal of both versions is the three-dimensional description of tracks and the determination of an interaction vertex. A charged particle is bent by the solenoidal magnetic field of the CJC in a way that its trajectory describes a helix in space. Since the magnetic field is parallel to the  $z$ -axis the projection on the  $xy$ -plane is a circle. The measured hits are defined in polar coordinates  $(r, \phi)$  and fitted to a circle using a non-iterative method [49]. From this procedure the curvature  $\kappa$ , the distance of closest approach to the origin  $dca$  and the  $\phi$  defined at the  $dca$  are obtained. The polar angle  $\theta$  and the  $z$ -axis intercept  $z_0$  at the  $dca$  are determined by a linear least-squares fit in the  $Sz$ -plane, where  $S_i^{xy}$  denotes the arc-length of the point  $z_i$  in the  $xy$ -projection, with  $S_i^{xy} = 0$  at the  $dca$ . The five track parameters are listed in Table 2.2. The momentum of the track is roughly given by the equation  $p_T \approx 0.3 \cdot B/|\kappa|$ , where the following units have to be used:  $p_T$ [GeV],  $\kappa$ [m<sup>-1</sup>],  $B$ [T].

In a further reconstruction step the *non-vertex-fitted* tracks are used to determine the primary vertex of an event. Therefore, well measured high momentum tracks of many events are selected and a least-squares fit minimizing the  $dca$  is performed. The in such a way measured  $x$ - and  $y$ -position of the interaction point is called the *run-vertex* and is defined at  $z = 0$ . The size of the interaction region in  $z$  is about 10 cm. In a subsequent fitting procedure all tracks are constrained to the run-vertex and hence the resolution is improved significantly. The run-vertex is determined for every *run*<sup>3</sup> consisting of at least several thousand events. The  $z$ -position of the vertex in an event is obtained from all tracks fitted to the run-vertex. Together with the information of the *beam-tilt*<sup>4</sup> the primary vertex of each event is computed and all tracks of the event are fitted to this vertex. The uncertainty of the primary vertex is dominated by the extension of the *beam-spot* which is about 150  $\mu\text{m}$  in  $x$  and 30  $\mu\text{m}$  in  $y$  [45]. The standard reconstruction program also searches for secondary vertices caused by the decays of neutral particles, like e.g.  $K_s^0 \rightarrow \pi^+\pi^-$  or  $\Lambda \rightarrow p\pi^-$ .

Once the *vertex-fitted* tracks are built the reconstruction algorithm tries to link hits provided by the  $z$ -chambers CIZ and COZ. Since the resolution of the  $z$ -coordinate measured by charge division within the CJC (see Section 2.2.3) is rather poor, a considerable gain

<sup>3</sup>The term *run* is used for a unit of data taking in which all detector, trigger and background conditions are roughly constant; the typical duration of a run is about 20 minutes

<sup>4</sup>The beam in the H1 detector is not exactly parallel but slightly tilted with respect to the  $z$ -axis defined by the CTD

in resolution for the parameters  $\theta$  and  $z_0$  can be achieved by the  $z$ -chamber information. The track parameters, together with various other track properties, e.g. number of hits, track length, fit probabilities etc., are stored in *tracker banks*. A description of the H1 tracker bank scheme can be found in [50].

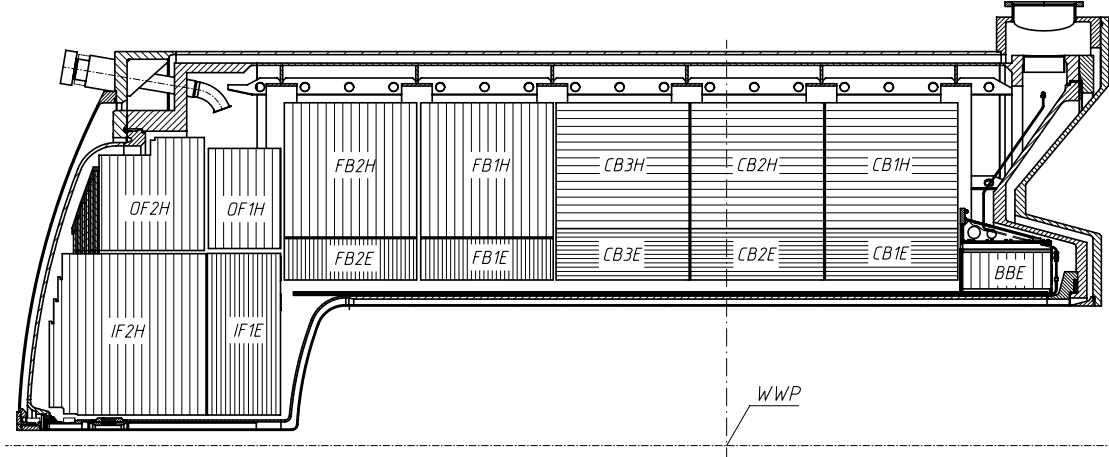


**Figure 2.8:** Side view of the upper part of the LAr calorimeter divided into electromagnetic (dark shaded) and hadronic (light shaded) and inner forward (IF), outer forward (OF), forward barrel (FB), central barrel (CB) and backward barrel (BB) parts.

### 2.2.5 The liquid argon calorimeter

The liquid argon calorimeter (LAr) is segmented longitudinally into eight *wheels* each of which is divided in  $\phi$  into eight identical stacks (Figure 2.8). It is a sandwich calorimeter composed of an electromagnetic and a hadronic part. The wheel located at the most backward point is purely electromagnetic. The calorimeter consists of about 45 000 electronic channels, with the highest granularity in the forward direction. The energy resolution is  $\sigma_E/E \approx 12\%/\sqrt{E[\text{GeV}]} \oplus 1\%$  in the electromagnetic part and  $\sigma_E/E \approx 50\%/\sqrt{E[\text{GeV}]} \oplus 2\%$  for the hadronic measurement. The total range of angular coverage is  $4^\circ \lesssim \theta \lesssim 153^\circ$ . A detailed description of the LAr calorimeter can be found in [38].

### 2.2.6 The backward detectors

The modification of the backward region was part of the 1995 upgrade of the H1 detector. The backward electromagnetic calorimeter BEMC and the backward proportional chamber BPC have been replaced by the spaghetti calorimeter SpaCal and the backward drift chamber BDC mounted in front of it. The main purpose of both chambers is to measure the scattered positron and hence to reconstruct the DIS kinematics of an event. Figure 2.9 shows where the SpaCal and the BDC are located within the H1 apparatus.

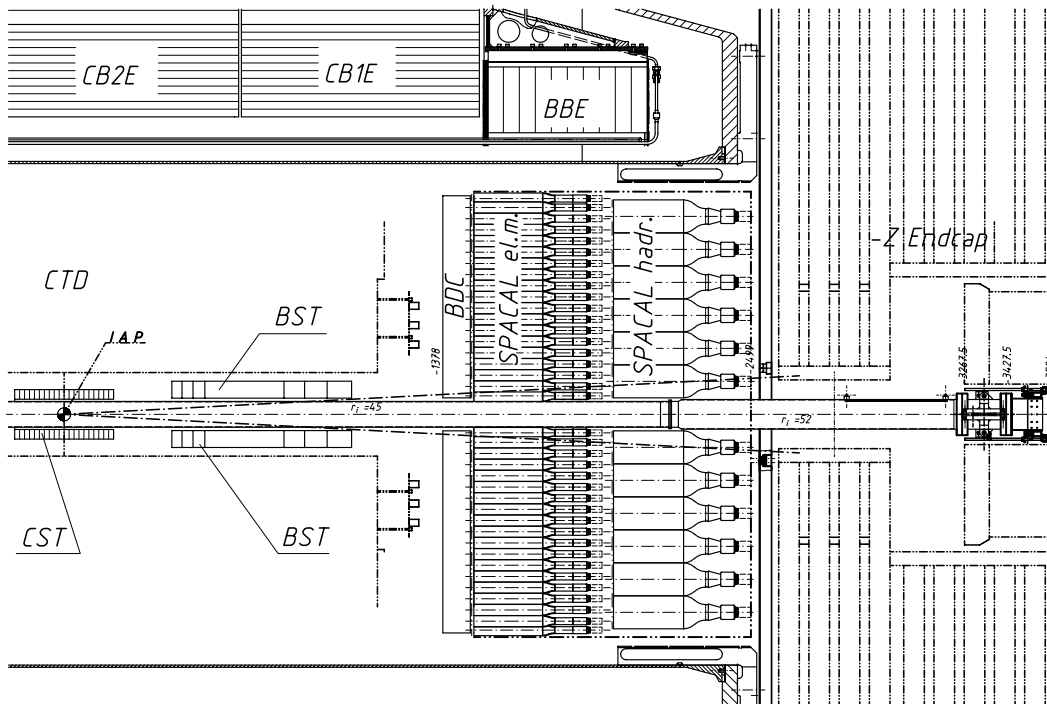


Figure 2.9: Side view of the backward detectors BDC and SpaCal.

### The spaghetti calorimeter

The spaghetti calorimeter SpaCal [51, 52, 53] is a scintillating fiber calorimeter with lead absorbers that is split into an electromagnetic and a hadronic part of 25 cm active depth each. The small cell size of  $4.5\text{cm}^2 \times 4.5\text{cm}^2$  in the electromagnetic part guarantees a good spatial resolution and a good electron-pion separation. The cell size of the hadronic section is  $11.93\text{cm}^2 \times 11.90\text{cm}^2$  accounting for the larger lateral size of hadronic showers. The electromagnetic part contains 1192 and the hadronic part 136 cells. The energy resolution of the SpaCal is about  $\sigma_E/E = 7.5\%/\sqrt{E[\text{GeV}]} \oplus 1\%$  in the electromagnetic part and  $\sigma_E/E \approx 30\%/\sqrt{E[\text{GeV}]} \oplus 7\%$  in the hadronic calorimeter. The angular acceptance is  $151^\circ \lesssim \theta \lesssim 178^\circ$  and therefore a kinematic regime down to  $Q^2 \approx 1\text{GeV}^2$  can be explored by the SpaCal.

### The backward drift chamber

The backward drift chamber BDC [54, 55, 56] is situated at  $z = -142\text{cm}$  and extends in radial direction from 6.3 cm to 72.0 cm, thus covering the full polar angular acceptance of the SpaCal (see Section 2.2.6). It consists of four double layers of drift chambers with wires strung perpendicular to the beam axis, forming concentric octagons of increasing size in a spiders web structure (Figure 2.10). Consecutive double layers are rotated to each other by  $11.25^\circ$  allowing for a precise measurement of the azimuthal coordinate  $\phi$  and minimizing overlaps of inefficient regions. Two adjacent cells in one double layer are

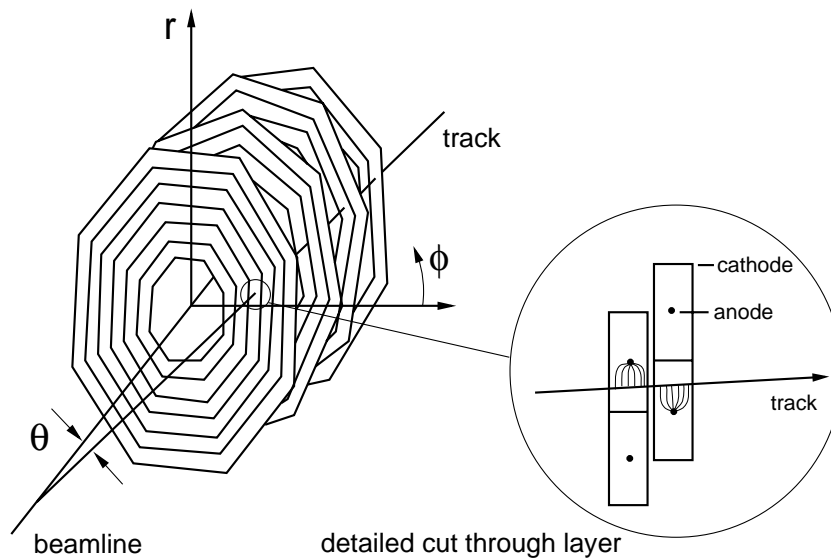


**Figure 2.10:** Schematic view of the four BDC double layers. An exploded view of two adjacent cells in one double layer is sketched.

shifted by the maximum drift length of the cell in order to solve the left-right ambiguity. An approximately radial drift field delivers an optimal resolution in the radial direction, such that the polar angle  $\theta$  of the scattered positron can be determined to an accuracy better than 1mrad. A separation, by tagging electromagnetic showers having no incidental charged particle track, can be performed accounting for photons, that can fake a positron in the SpaCal.

## 2.2.7 Forward detectors

In this analysis forward detectors are used to tag the proton remnant in processes where the proton dissociates diffractively (see Section 1.4). The remnant particles are scattered at very low angles to the direction of the proton beam. They can either be detected directly or via showers of secondary particles arising from collisions with the beam pipe or a collimator. Therefore the forward detectors, which are discussed in the following, provide an effective method to probe the proton remnant and help to select elastic events, where the proton stays intact and little activity in the forward region is expected.

### The forward muon detector

The forward muon detector FMD [57] is a spectrometer which consists of six double layers of drift chambers, three on either side of a toroidal magnet providing a field of 1.5 T to 1.75 T. Four of the drift chambers have wires strung concentrically to the beam axis to measure  $\theta$  while two have a radial wire setup to measure  $\phi$ . The two layers of drift cells are shifted in such a way that the left-right ambiguity is eliminated. A charged particle that penetrates the two layers of drift cells produces a pair of hits. The single hit resolution is of the order of  $\approx 250 \mu\text{m}$ . The hit-pairs can be linked to those of other layers, track

segments can be reconstructed and their momenta can be measured. The FMD covers polar angles of  $3^\circ < \theta < 17^\circ$  and is mounted between 6.4 m and 9.4 m forward of the H1 origin. A schematic view of the FMD is shown in Figure 2.11.

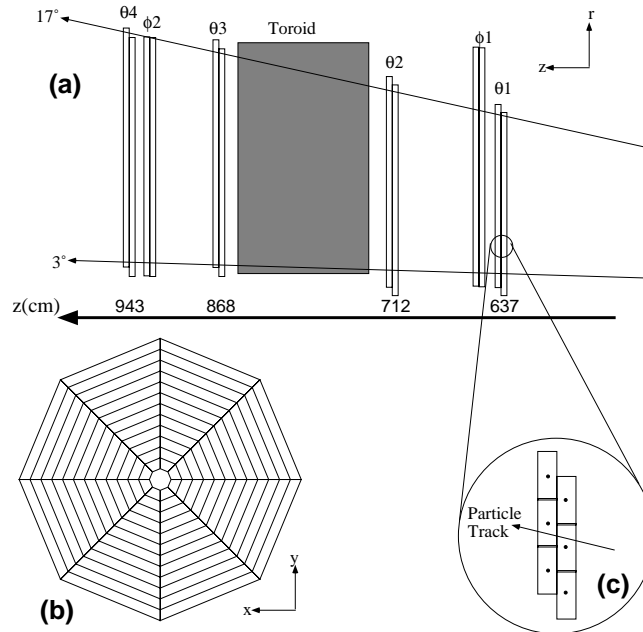


**Figure 2.11:** The forward muon detector. (a) shows the six pre- and post-toroid layers in the  $rz$ -projection. (b)  $xy$ -projection of a  $\theta$  layer. (c) Exploded profile of the drift cells comprising two sub-layers.

### The proton remnant tagger

The proton remnant tagger PRT [58] consists of seven pairs of scintillators shielded with lead and situated around and between the beam pipes at  $z = 24$  m. Each scintillator pair is operated in coincidence mode. Thus a signal is only registered if both pulses of a scintillator pair coincide with the expected time of arrival of particles emerging from the interaction region. The polar angular acceptance of the PRT is  $0.06^\circ \lesssim \theta \lesssim 0.17^\circ$ . A schematic view of the PRT is shown in Figure 2.12.

### 2.2.8 Trigger scheme

The H1 trigger system was designed to discriminate genuine  $ep$  interactions from background events. It consists of a partially pipelined 5 level trigger system L1, L2, L3<sup>5</sup>, L4 and L5. Trigger levels L1 and L2 are online hardware triggers, while L4 is an online software trigger. The fifth trigger level L5 runs offline and uses the full detector information

<sup>5</sup>The L3 trigger level has not yet been used

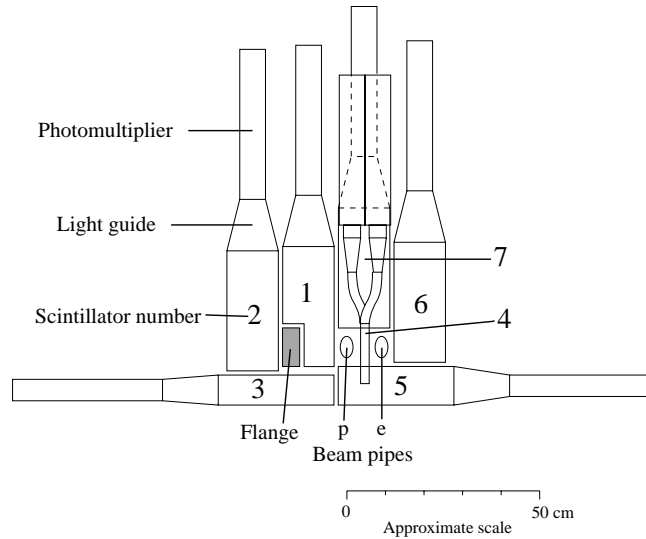


**Figure 2.12:** Schematic view of the proton remnant tagger PRT, looking towards the interaction point.

allowing for an event classification. The sketch of the multi-level trigger scheme together with the relevant rates and decision times is given in figure 2.13.

**L1** is the first trigger level where the signals provided by the different subdetectors (*trigger elements*) are combined logically into 128 *subtriggers*. Since the subdetector information can not be read out before the next bunch crossing occurs (96 ns) it has to be stored in front-end buffers (*pipelines*). The data are kept available for 24 bunch crossings ( $2.3 \mu\text{s}$ ) according to the time L1 needs to decide whether an event is accepted or not. If an event is triggered by one (or more) of the 128 subtriggers, an *L1 keep* signal is sent to all different subsystems, the pipeline is stopped and the detector information is passed to the next trigger level. The L1 trigger reduces the typical acquisition rate of non-empty H1 events (100 kHz) by roughly a factor of 50. The subsystems, which produce trigger elements used in this analysis, are discussed below.

**L2** is a trigger system based on *neural networks* (L2NN) and *topological correlations* (L2TT) between different trigger subsystems. The input rate of about 1 kHz is reduced to about 50 Hz. Every L2 trigger element is logically connected to one or more L1 subtriggers and hence used to reduce high rate of L1 subtriggers. If an event is accepted by L2 the detector signals are read out. The dead time between the *L2 keep* signal and the completion of the read-out is typically 1 – 2 ms per event. The L1 subtrigger used in this analysis has no L2 trigger requirement.

**L4** is a multi processor filter farm made up of 30 Power PC boards working in parallel. The L4 input rate of up to 50 Hz is reduced to about 10 Hz, whereby all accepted events are recorded to tape. With the full detector information available, a fast version of the event reconstruction (see Section 2.2.4) is performed. Thus

physics selection algorithms cutting on measured physical quantities such as invariant masses or the identification of the scattered positron can be applied. The performance of these *event finders* can be monitored using a fraction of around 1% of the rejected events (*L4 reject events*), which are retained. Until 1996 L4 was used just as a background filter. Since 1997, a fraction of physics processes with high rates, e.g. inclusive photoproduction events, were downscaled, due to the higher luminosity delivered by HERA.

**L5** is a dedicated computing farm where all events which have passed L4 are fully reconstructed. The events are assigned to certain physics event classes and are stored on *data summary tapes* (DSTs) which are the basis for physics analyses.

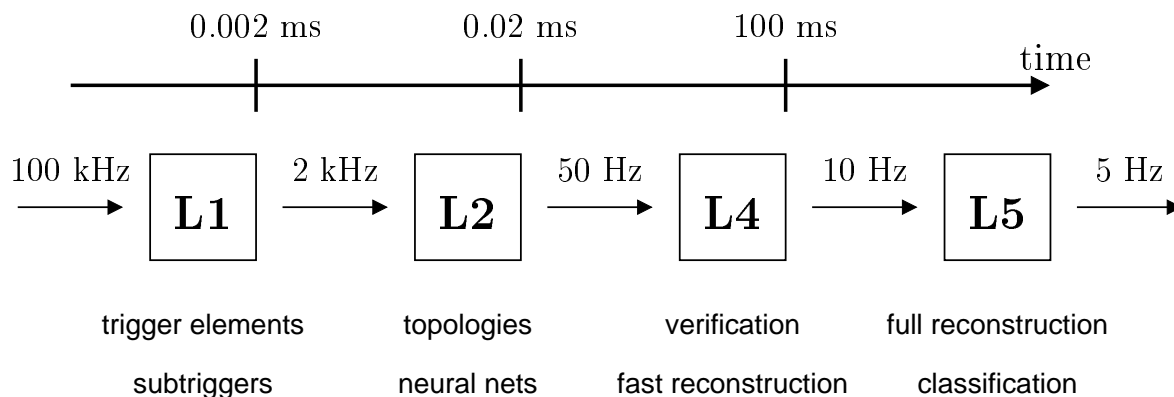


**Figure 2.13:** Trigger levels used during 1994 to 1997 data taking. Shown are typical rates and decision times for each level.

### L1 trigger elements

L1 consists of 192 trigger elements delivered by various detector subsystems. Those which are relevant for the analysis presented in this thesis are briefly explained here. More detailed descriptions can be found in the given references.

**The SpaCal trigger** [59] provides both a DIS electron candidate selection and a veto on proton beam induced background. The trigger comprises a ToF and an *Anti-ToF* AToF system. The ToF system recognizes signals in-time and the AToF system those out-of-time with respect to the nominal interaction timing and is thus able to discriminate against background from upstream proton beam gas collisions. The in-time region is defined by a time window of typically  $\approx 20$  ns within which the energy analog sum for so-called *sliding windows* is computed. These sliding windows are the basic unit of the *inclusive electron trigger* (IET) and consist of arrays of  $4 \times 4$  neighbouring cells defined for the electromagnetic part of the SpaCal. Adjacent sliding windows overlap to ensure triggering of showers which extend over cell boundaries. In each sliding window the measured energy deposit is compared to three different thresholds, namely  $\text{Spcl}_e\text{-IET}>0$ ,  $\text{Spcl}_e\text{-IET}>1$ , and  $\text{Spcl}_e\text{-IET}>2$ . They are adjustable in the range 100 MeV to 20 GeV with typical thresholds of 0.5, 2 and 6 GeV. If a signal in any of the sliding windows exceeds one of

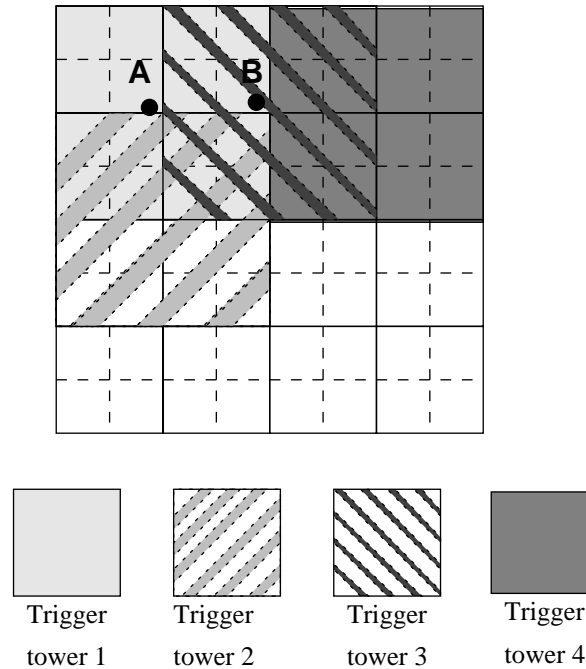


**Figure 2.14:** Principle of the inclusive electron trigger.

the thresholds the event is triggered. An illustration of the sliding window technique is shown in Figure 2.14.

During the analyzed data taking periods the SpaCal was affected by the *hot spot*, a beam related permanent activity in the region close to the beam pipe. This background source caused high rates for the inclusive electron trigger.

**The  $z$ -vertex trigger** [60, 61] provides a rough determination of the  $z$  position of the event vertex. This is achieved by the combination of the pad signals of the multi-wire proportional chambers (CIP, COP) and the first double-layer of the forward proportional chamber (FPC) into *rays*. A ray is defined as the coincidence of signals in four pads<sup>6</sup> that can be connected by a straight line in the  $rz$ -plane. The number of these rays enters a 16 bin wide histogram, whereby each bin is related to the origin of its respective rays along the  $z$ -axis. The resulting 16 histograms (one for each  $\phi$  sector) are combined to give the  $z$ -vertex histogram. It covers a range of  $\pm 44$  cm in  $z$  around the nominal interaction point. The bin with the largest number of entries is expected to contain the interaction vertex of the  $ep$  collision (Figure 2.15).

The  $z$ -vertex trigger logic provides a large variety of significance and multiplicity conditions. The most important one is the `zvtx_t0` trigger element which is set when at least one ray is found. It is used by most subtriggers to assign an event to its related bunch crossing. The trigger element `zvtx_mul<7` demands less than 200 entries in the  $z$ -vertex histogram and thus vetos background events with very high track multiplicities. The `zvtx_sig` trigger condition is fulfilled when the number of entries in the peak bin is significantly larger than the average number of entries in the remaining bins.

<sup>6</sup>Trigger inefficiencies due to dead pads can be regained by relaxing the coincidence to three pads that have fired (*3\_of\_4 option*).

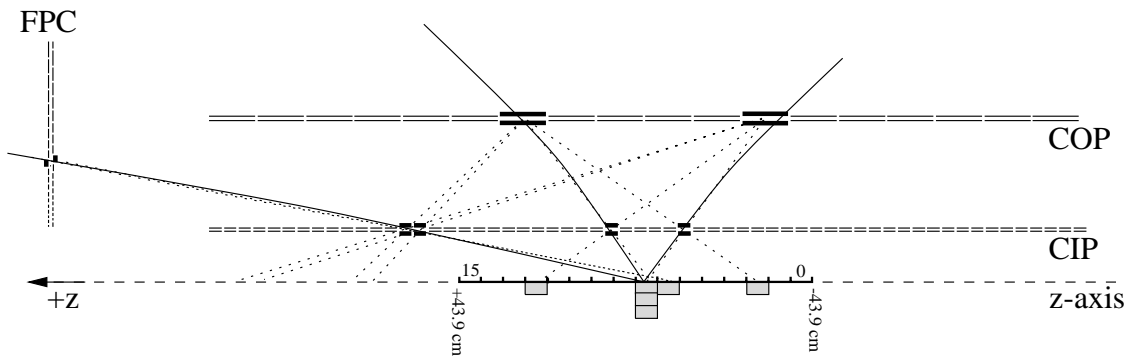


**Figure 2.15:** The  $z$ -vertex histogram in the  $rz$ -view for one  $\phi$  sector is shown. Rays originating from genuine particles are indicated by full lines, while the dotted lines indicate the wrong combinations.

The **central drift chamber trigger** was designed for triggering events containing high momentum tracks. The trigger, that is often referred to as the  $DCr\phi$ -trigger [62], uses the signals provided by the CJC1 and CJC2 (see Section 2.2.3). Thereby the digitized hits of 10 wire layers of CJC1 and the inner part of CJC2 are compared to a total of 10 000 predefined masks. Track candidates in the *low* ( $0.45 \lesssim p_T \lesssim 0.8$  GeV) and in the *high* (DCRPh\_THig with a momentum threshold of  $p_T \gtrsim 0.8$  GeV) region of transverse momentum are triggered separately for negative and positive charges. Since the masks are suited for tracks with a distance of closest approach of less than 2 cm, the  $DCr\phi$ -trigger efficiently rejects background due to beam wall interactions.

## 2.2.9 Detector simulation

Events generated by Monte Carlo programs are used to study the detector response in terms of acceptances and efficiencies. Four-vectors of particles are generated assuming a specific physics production mechanism. The tracking of these particles through the detector is performed by a GEANT [63] based application. It is the most time consuming part of the detailed event simulation done by the H1SIM program. The GEANT framework includes a fast simulation of the energy response of the calorimeter, where a parametrization of the development of electromagnetic and hadronic showers as implemented in H1FAST [64, 65] is used. Furthermore the trigger response is simulated.

Special data runs of randomly triggered events are used to study noise fluctuations in the calorimeters and forward detectors.

The simulated Monte Carlo events as well as the randomly triggered events are fed through the same reconstruction and analysis procedure as the data. It is self-evident that the simulation of the detector can only be used for analysis when its agreement with the data is guaranteed.

# Chapter 3

## Event Selection

In this chapter the method of selecting  $D^*$  mesons in diffractive deep inelastic scattering is described. The data used in this analysis were collected over the years 1995, 1996 and 1997. After a short description of the pre-selection, in terms of basic quality criteria the data have to fulfill, the selection of deep inelastic scattering events is explained. A short introduction to the detection of the scattered positron and the reconstruction of the kinematic variables is given. Thereafter the method of reconstructing  $D^*$  mesons through the decay chain  $D^* \rightarrow D^0 \pi_s \rightarrow (K \pi) \pi_s$  is explained. The kinematic region for which the cross sections are measured is defined. In the last section, the typical signature of diffractive events within the H1 detector is illustrated and the technical aspects of the selection are described.

### 3.1 Run selection

During the whole data taking period it was required that all parts of the detector essential for the analysis were fully operational in terms of their read-out and high voltage systems. These relevant components are the jet chambers (CJC1 and CJC2), the central proportional chambers (CIP and COP), the backward drift chamber (BDC), the liquid argon and the spaghetti calorimeter (LAr and SpaCal), all Time-of-Flight (ToF) devices and the luminosity system. The forward muon detector is used in this analysis for the selection of diffractive events and its full operation must also be guaranteed. At the start of the 1997 data taking this system suffered from read-out problems and therefore the corresponding run range 177920-184256 is excluded from the analysis. In addition only runs, recorded during trigger phases 2-4 of a luminosity fill, are analyzed. The very early period of a luminosity run (phase 1) is excluded due to heavily prescaled subtriggers (see Section 3.1.2) accounting for the corresponding high beam current and background rates. Only runs which are classified as *good* or *medium* quality<sup>1</sup> runs are accepted. Runs with special trigger settings (e.g. minimum bias runs) or a systematically shifted vertex position are also rejected.

---

<sup>1</sup>A run quality classification is performed online. A run is classified as *poor* when one or more essential detector components, for example the LAr or the CJC are not operational

	1995	1996	1997	$\Sigma$
$\int \mathcal{L} dt$ delivered by HERA [nb <sup>-1</sup> ]	10095	13299	32400	55794
$\int \mathcal{L} dt$ H1 on tape [nb <sup>-1</sup> ]	6196	8919	27344	42459
$\int \mathcal{L} dt$ for good and medium runs [nb <sup>-1</sup> ]	5538	8648	23706	37892
$\int \mathcal{L} dt$ after HV and run selection [nb <sup>-1</sup> ]	3184	8411	20245	31840
Average satellite correction (%)	3.8	7.3	6.7	—
Average prescale factor	1.775	1.032	1.519	—
$\int \mathcal{L} dt$ used in analysis [nb <sup>-1</sup> ]	1727	7559	12438	<b>21723</b>

**Table 3.1:** *Integrated luminosities 1995 to 1997. The luminosity used in this analysis amounts to 21.72 pb<sup>-1</sup>.*

At the beginning of 1995 the new backward detectors BDC and SpaCal came into operation for the first time. Due to many hardware problems during this period of data taking a special run selection [66] is applied, which guarantees that there is a reliable energy calibration and a properly working trigger.

### 3.1.1 The analysis subtrigger

The analyzed data were triggered on the first trigger level L1 (see Section 2.2.8) by subtrigger `s2 (s61)`<sup>2</sup>, which demands a signal from the inclusive electron trigger (`Spcl_e_IET>1`) in coincidence with a charged track signal from both the  $z$ -vertex trigger (`zvtx_sig`) and the  $DCr\phi$ -trigger (`DCRPh_THig`, where `_THig` means at least one track with a transverse momentum above a threshold of 800 MeV). In addition several veto conditions, concerning the timing of the event, are applied. During the data taking periods of 1996 and 1997 the subtrigger configuration was adjusted several times accounting for changing background rates due to varying beam conditions.

### 3.1.2 Luminosity

In addition to the selection criteria described in Section 3.1 the luminosity has to be corrected for a small fraction of events produced by the collisions of positrons with protons originating from *satellite bunches*. Protons can migrate from their bunches and accumulate into satellite bunches separated by  $\sim 5$  ns from the main bunches and hence collide with the positron beam at  $z$ -positions of the vertex  $|z_{vtx}| \gtrsim 40$  cm. In this analysis satellite bunch interactions are rejected by restricting the vertex with respect to the nominal interaction point to  $|z_{vtx} - \bar{z}| < 40$  cm. The luminosity has to be corrected according to the fraction of events rejected by this cut.

<sup>2</sup>The subtrigger conditions `s2` changed to `s61` during the data taking in 1997 for run numbers greater than 193432.

Due to the high specific luminosity delivered by HERA many subtriggers are *prescaled* such that only every  $p_i$ -th event of subtrigger  $i$  is accepted. To account for event losses due to pre-scaling the integrated luminosity  $\mathcal{L}_j$  of each run  $j$  is corrected as  $\mathcal{L}_i = \sum_j \mathcal{L}_j / p_{ij}$ , where the sum includes all runs where subtrigger  $i$  was active.

The contributions to the integrated luminosity from the three years 1995, 1996 and 1997 and the reduction due to the corrections are listed in Table 3.1. The luminosity that is finally used in this analysis amounts to  $21.72 \text{ pb}^{-1}$ .

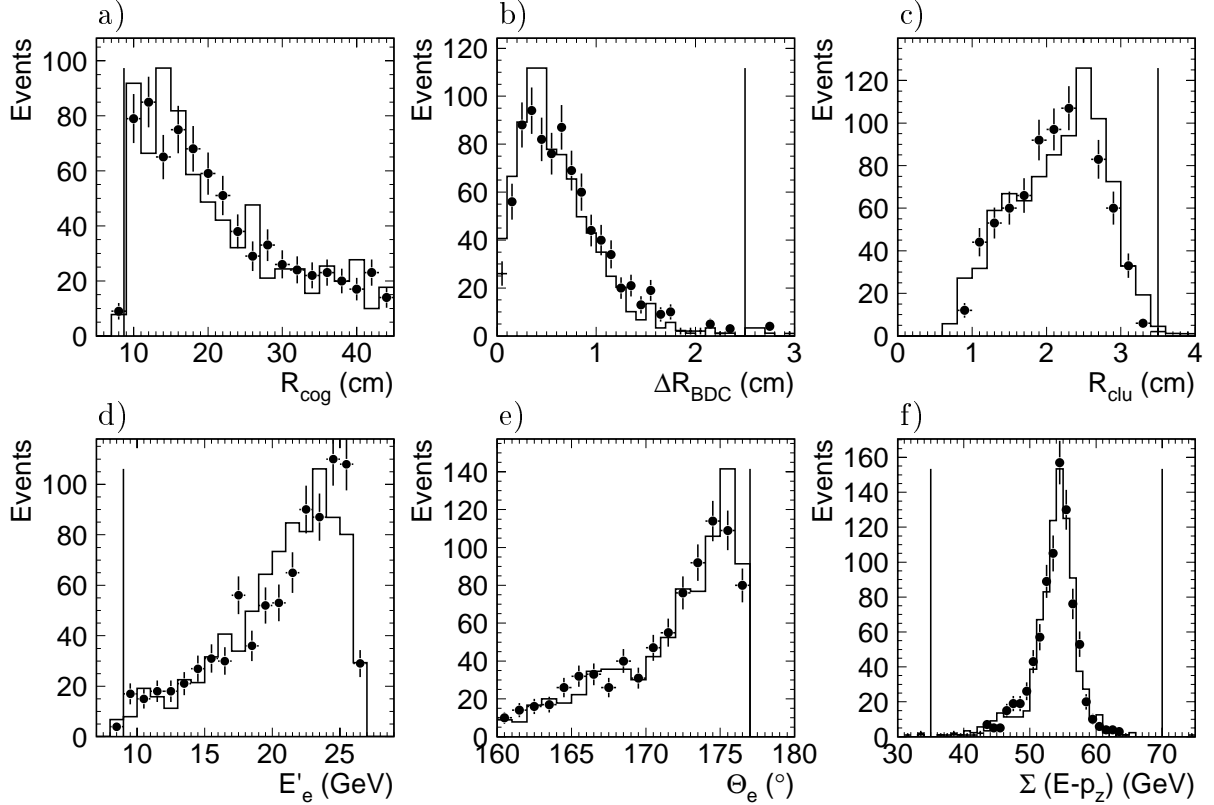


**Figure 3.1:** Selection of positron candidates; a) radial distance from the beam axis of the cluster's center of gravity  $R_{cog}$ , b) distance  $\Delta R_{BDC}$  of the cluster's center of gravity to track segment in the BDC and c) energy weighted cluster radius  $R_{clu}$ . d) energy and polar angle e) of the scattered positron. f) shows the  $\Sigma(E - p_z)$  distribution. For each histogram, all cuts (vertical lines) except the one shown are applied. The data are compared to RAPGAP Monte Carlo events shown as histograms normalized to the number of events in the data.

## 3.2 Deep inelastic scattering events

The presented analysis is restricted to events from deep inelastic  $e^+p$  scattering (DIS) processes. Therefore the scattered positron has to be detected and identified in the spaghetti calorimeter SpaCal and the backward drift chamber BDC, see Section 2.2.6. The selection criteria defining a good positron candidate and the reconstruction of the DIS kinematic variables are briefly described in the following.

### 3.2.1 Selection of DIS events

The fundamental measured quantity used to identify the scattered positron is the energy deposit in each cell of the SpaCal. The cells are assigned to clusters and the cluster energy is computed by summing over all cell energies  $E_i$ . If  $\vec{r}_i$  denotes the position of the  $i$ -th cell the center of gravity of the cluster  $\vec{r}_{cog}$  can be defined by

$$\vec{r}_{cog} = \frac{\sum w(E_i)\vec{r}_i}{\sum w(E_i)}, \quad (3.1)$$

where the sum runs over all cells  $i$  and  $w(E_i)$  is a square-root weighting function of the form  $w(E_i) = \sqrt{E_i}$ . The lateral size of a cluster can be estimated by the energy weighted cluster radius

$$R_{clu} = \frac{1}{E} \sum E_i |\vec{r}_i - \vec{r}_{cog}| \quad (3.2)$$

and is used to discriminate between electromagnetic and hadronic showers which tend to be broader. In this analysis the scattered positron is defined as the most energetic cluster in the electromagnetic part of the SpaCal with a radius smaller than 3.5 cm and an energy  $E'_e$  larger than 9 GeV. A cut  $R_{cog} > 8.7$  cm, where  $R_{cog}$  is the distance of the center of gravity of the cluster to the beam in the radial direction, is applied to ensure good reconstruction i.e. reduce losses into the inner region of the SpaCal. This cut is to a large extent covered by a cut on the angle of the scattered positron  $\theta_e < 177^\circ$ . In addition, the distance of the cluster's center of gravity to an associated charged track segment in the backward drift chamber BDC  $\Delta R_{BDC}$  has to be less than 2.5 cm. This cut reduces the background from photons which mainly originate from  $\pi^0$  decays and do not produce a track in the BDC but fake a positron candidate in the SpaCal. In Figure 3.1 the quantities  $R_{cog}$  (a),  $\Delta R_{BDC}$  (b) and  $R_{clu}$  (c) defining clusters of good quality are plotted for  $D^*$  candidates (see Section 3.3) lying in the range  $\pm 2$  MeV around the nominal mass difference  $\Delta M$ . The energy (d) and the polar angle (e) of the scattered positron are also shown. Except the one on the plotted quantity all cuts, which are indicated by horizontal lines, are applied. In Figure (f) the  $\sum(E - p_z)$  distribution is plotted. The data are reasonably well described by the simulation of  $D^*$  events shown as histograms. The events were generated with the Monte Carlo generator RAPGAP, see Section 1.4.2. In the simulation the cluster radius  $R_{clu}$  is multiplied by a factor 1.1 accounting for an imperfect modelling of the transverse showering of the cluster [53]. The position of the track segment together with the position of the primary vertex is used to improve the less precise measurement of the positron scattering angle  $\theta_e$  by the cluster position in the SpaCal.

From the measured hadronic final state the quantity  $\sum(E - p_z)$  can be calculated, where the difference between the energy and the  $z$ -component of the momentum has to be summed over all particles in the event. Assuming that all particles were measured in a perfect detector, the conservation of energy and momentum demands  $\sum(E - p_z)$  to be twice the energy (the proton rest mass is neglected) of the positron beam energy, i.e. 55 GeV. Any losses of particles, especially photoproduction events where the scattered positron escapes down the beam pipe, as well as initial state radiation, will lower this

<b>Selection of <math>D^*</math> mesons in DIS</b>	
Subtrigger condition: Spcle_IET $\wedge$ zvtx_sig $\wedge$ DCRPh_THig	
DIS events	Reconstruction of $D^* \rightarrow D^0 \pi_s \rightarrow (K\pi)\pi_s$
<ul style="list-style-type: none"> <li>• Most energetic cluster in electromagnetic SpaCal</li> <li><math>E_e &gt; 9 \text{ GeV}</math></li> <li><math>\theta_e &lt; 177^\circ</math></li> <li><math>R_{cog} &gt; 8.7 \text{ cm}</math></li> <li><math>\Delta R_{BDC} &lt; 2.5 \text{ cm}</math></li> <li><math>R_{clu} &lt; 3.5 \text{ cm}</math></li> <li><math>35 &lt; \sum(E - p_z) &lt; 70 \text{ GeV}</math></li> <li><math> z_{vtx} - \bar{z}  &lt; 40 \text{ cm}</math></li> </ul>	<ul style="list-style-type: none"> <li>• Primary vertex-fitted tracks</li> <li><math>dca(K, \pi, \pi_s) &lt; 2 \text{ cm}</math></li> <li><math>L_{r\phi}(K, \pi, \pi_s) &gt; 10 \text{ cm}</math></li> <li><math>R_{start}(K, \pi, \pi_s) &lt; 35 \text{ cm}</math> (1995/96)</li> <li><math>R_{start}(K, \pi, \pi_s) &lt; 50 \text{ cm}</math> (1997)</li> <li><math>20^\circ &lt; \theta(K, \pi, \pi_s) &lt; 160^\circ</math></li> <li><math>p_T(K, \pi) &gt; 250 \text{ MeV}</math></li> <li><math>p_T(\pi_s) &gt; 140 \text{ MeV}</math></li> <li><math> M(K, \pi) - M(D^0)  &lt; 80 \text{ MeV}</math></li> <li><math>z(D^*) &gt; 0.2</math> if <math>p_T(D^*) &lt; 3 \text{ GeV}</math></li> </ul>
Kinematic range	
$2 < Q^2 < 100 \text{ GeV}^2$	$p_T(D^*) > 2 \text{ GeV}$
$0.05 < y < 0.7$	$-1.5 < \eta(D^*) < 1.5$

**Table 3.2:** Summary of the selection criteria used to reconstruct  $D^*$  mesons through the decay chain  $D^* \rightarrow D^0 \pi_s \rightarrow (K\pi)\pi_s$  in deep inelastic scattering (DIS) events.

value. Therefore a cut  $35 < \sum(E - p_z) < 70 \text{ GeV}$  is applied, whereby the upper cut is imposed to reject poorly reconstructed events. Experimentally, the hadronic final state is reconstructed by the simultaneous use of tracks and clusters without double counting of energy. To benefit from the accurate momentum measurement first of all tracks are used. The tracks are extrapolated to the calorimeter and its energy is compared to the energy content in the calorimeter within a cylinder of 30 cm radius around the track. If the energy accumulated in the cylinder is larger than twice that of the track the energy in the calorimeter is taken, otherwise the track energy is used.

### 3.2.2 DIS kinematics

The kinematic quantities  $Q^2$  and  $y$  can be determined using various methods. In the *electron method* they are calculated from the energy  $E'_e$  and  $\theta_e$  of the scattered positron

$$Q^2 = 4E_e E'_e \cos^2 \frac{\theta_e}{2} \quad y = 1 - \frac{E'_e}{E_e} \sin^2 \frac{\theta_e}{2}. \quad (3.3)$$

The electron method provides an excellent resolution over the full kinematic range in  $Q^2$  and in the high  $y$  region. Towards lower values of  $y$  the electron method depends crucially on the precise calibration of the electromagnetic energy scale of the SpaCal and the resolution degrades as  $1/y$ . The electron method is sensitive to energy losses

Decay mode	Branching ratio (%)
$D^{*+} \rightarrow D^0 \pi_s^+$	$(68.3 \pm 1.4)$
$D^0 \rightarrow K^- \pi^+$	$(3.85 \pm 0.09)$
$D^{*+} \rightarrow K^- \pi^+ \pi_s^+$	$(2.63 \pm 0.08)$

**Table 3.3:** Branching ratios in the decay  $D^* \rightarrow D^0 \pi_s \rightarrow (K\pi)\pi_s$ .

due to photon radiation off the positron. The  $\Sigma$  method provides an alternative method to measure  $y$  that does not depend on the measurement of the energy of the scattered positron and is thus less sensitive to photon radiation. In this method  $y$  is given by the fraction  $\Sigma/\sum(E - p_z)$  with  $\Sigma = \sum(E - p_z)_{had}$ . To calculate  $\Sigma$  one has to sum over all hadrons of the final state only. The denominator then differs from the numerator by the contribution of the scattered positron  $E'_e(1 - \cos\theta_e)$  to  $\sum(E - p_z)$ . A comparison of the electron and the  $\Sigma$  method can be found in [67].

In this analysis the electron method is used to reconstruct  $Q^2$  and  $y$ . The kinematic region in  $y$  is restricted to the range  $0.05 < y < 0.7$ , where the lower cut is applied for the reasons discussed above. The upper cut roughly corresponds to the cut on the energy of the scattered positron candidate  $E'_e > 9$  GeV. The accepted geometrical region of the SpaCal (see Section 3.2.1) corresponds to the kinematic range  $2 < Q^2 < 100$  GeV<sup>2</sup>. For values of  $Q^2 > 100$  GeV the positron is scattered into the liquid argon calorimeter.

The applied cuts to tag a good positron candidate and the measured kinematic range of DIS events are summarized in Table 3.2.

### 3.3 Reconstruction of $D^*$ mesons

In this thesis  $D^*$  mesons are identified by the reconstruction of the decay chain

$$D^{*\pm} \rightarrow D^0 \pi_s^\pm \rightarrow (K^\mp \pi^\pm) \pi_s^\pm, \quad (3.4)$$

with an overall branching fraction of 2.63%. The branching ratios of the individual decays are listed in Table 3.3. All values for the particle properties are taken from [68]. The reconstruction method makes use of the  $D^*$  tagging technique that utilizes the tight kinematic constraint of the decay  $D^* \rightarrow D^0 \pi_s$  [69] leading to the correlation  $p(\pi_s) \approx m_\pi/m_{D^0} p(D^0)$  of the momenta of the  $\pi_s$  and the  $D^0$  in the laboratory frame. Therefore the  $\pi_s$  is usually referred to as the *slow* pion.

Tracks are selected fulfilling the criteria as defined in the following section and the invariant mass  $M(K, \pi)$  is calculated for all opposite charge track combinations in the event. Since no particle identification is used the combination  $M(\pi, K)$ , where the rest mass of the pion instead of the kaon is assigned to the first track of a pair, has also be taken into account. If this invariant mass lies in the range  $\pm 80$  MeV around the nominal mass of the  $D^0$  (*mass window*) the pion mass hypothesis is assigned to all remaining tracks in the event and the invariant mass  $M(K, \pi, \pi_s)$  of the three track combinations is computed.

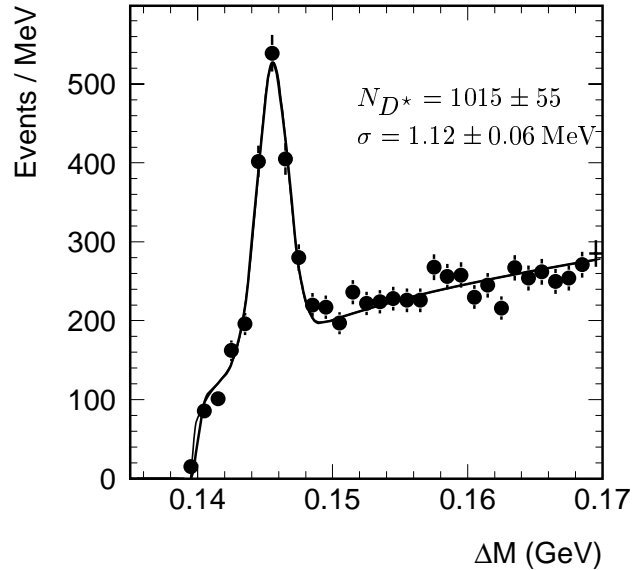


**Figure 3.2:** Total inclusive  $D^*$  signal fulfilling the cuts summarized in Table 3.2. A total of  $N_{D^*} = 1015 \pm 55$  candidates is extracted from the  $\Delta M = M(K, \pi, \pi_s) - M(K, \pi)$  distribution by a maximum likelihood fit of a Gaussian to describe the signal plus a term  $N_{bg}(\Delta M - m_\pi)^a$  for the background. The mean is  $145.6 \pm 0.07$  MeV and the width  $\sigma$  of the peak is  $1.12 \pm 0.06$  MeV. The signal-to-noise ratio is about 1.2.

Hereby the  $\pi_s$  has to have opposite sign of the kaon candidate.  $D^*$  production is observed as a distinct enhancement in the distributions of the mass difference

$$\Delta M = M(K, \pi, \pi_s) - M(K, \pi) \quad (3.5)$$

around the expected mass difference of 145.4 MeV.

### 3.3.1 Track selection

The decay products of the  $D^*$  are measured in the central jet chamber (CJC) (see Section 2.2.3). Therefore only charged particle tracks are considered which lie in the angular acceptance  $20^\circ < \theta < 160^\circ$  of the CJC. Since the CJC can not resolve the secondary vertices of the consecutive decays all tracks must be fitted to the primary vertex and have a distance of closest approach  $dca$  to the primary vertex of less than 2 cm. To protect further against badly reconstructed tracks, each track is required to have a length  $L_{r\phi}$  of at least 10 cm in the  $r\phi$ -plane and a start radius  $R_{start}$  in the inner section of the tracker. For the 1995 and 1996 data a cut  $R_{start} < 35$  cm is applied. In 1997 this cut is relaxed to 50 cm due to inefficient regions in the CJC1. The reconstruction efficiency for tracks with momenta  $p_T \lesssim 120$  MeV drops rapidly [70]. The transverse momentum of the  $\pi_s$  is kinematically correlated with the transverse momentum of the  $D^*$  (see Figure 3.3(a)) and therefore a low cut on  $p_T(\pi_s)$  is required. To guarantee a reliable and efficient track reconstruction a cut  $p_T(\pi_s) > 140$  MeV is applied. The  $p_T$  spectrum of the  $D^0$  decay

Data sample	Events $N_{D^*}$	Mean $\mu$ (MeV)	Width $\sigma$ (MeV)	Slope $a$
95	$130 \pm 20$	$145.4 \pm 0.15$	$1.12 \pm 0.21$	$0.33 \pm 0.08$
96	$340 \pm 31$	$145.5 \pm 0.09$	$1.10 \pm 0.10$	$0.30 \pm 0.04$
97	$548 \pm 41$	$145.6 \pm 0.09$	$1.12 \pm 0.09$	$0.31 \pm 0.03$
$\Sigma$	$1015 \pm 55$	$145.6 \pm 0.07$	$1.12 \pm 0.06$	$0.31 \pm 0.02$

**Table 3.4:** Results from a maximum likelihood fit to the  $\Delta M$  distribution of the 95, 96, 97 and the total event sample. The data are fitted to a function of the form  $N_{bg}(\Delta M - m_\pi)^a$  to describe the background and a Gaussian for the signal. The Gaussian is normalized to the number of entries in the signal  $N_{D^*}$ . The mean  $\mu$  of the peak position, the width  $\sigma$  and the slope  $a$  of the background are given.

products is harder than those originating from light quark production and from combinatorial background and therefore a higher  $p_T$  cut of at least 250 MeV is imposed for the  $K$  and the  $\pi$ .

### 3.3.2 Kinematic region

In Figure 3.3 the correlations between different kinematic variables are shown as predicted by the AROMA simulation (see Section 1.5.3) of inclusive  $D^*$  events. As can be seen from Figure (a), the slow pion carries typically less than 10% of the  $D^*$  momentum. The larger the value of  $y$  the higher the longitudinal momentum carried by the exchanged photon and the  $D^*$  is increasingly boosted in the backward direction which means low values of  $\eta$ , Figure (b). Figure (c) shows a slightly increasing  $p_T(D^*)$  with increasing values of  $Q^2$ . From the strong correlation between the azimuthal angles  $\phi$  of the  $D^*$  and the scattered positron shown in Figure (d) it can be seen that the particles are back-to-back in the plane perpendicular to the beam axis and the  $D^*$  meson gets additional transverse momentum from the recoil of the positron.

The  $D^*$  cross sections presented in this thesis are quoted for a *visible* kinematic region. This means the measurement is restricted to a range where the detector has full acceptance and a well understood efficiency. The transverse momentum of the  $D^*$   $p_T(D^*)$  is required to be larger than 2 GeV, which is dictated by the cut on the transverse momentum of the  $\pi_s$ . Its pseudorapidity  $\eta = -\ln \tan(\theta/2)$  has to be in the range  $-1.5 < \eta(D^*) < 1.5$ .

The signal to background ratio is improved by the cut  $z(D^*) > 0.2$  that has to be fulfilled for all candidates with  $p_T(D^*) < 3$  GeV. The quantity  $z(D^*)$  is explained in Section 1.3.

The number of  $D^*$  mesons is extracted from a maximum likelihood fit to the  $\Delta M$  distribution. The signal is described by a Gaussian and the background by a term of the form  $N_{bg}(\Delta M - m_\pi)^a$ . All fits have been performed using the software package MINUIT [71]. The inclusive  $\Delta M$  distribution which is obtained when applying all selection cuts listed in Table 3.2 is plotted in Figure 3.2. A total of  $N_{D^*} = 1015 \pm 55$  events is observed. The signal-to-noise ratio is about 1.2. The mean  $\mu$  of the peak is  $145.6 \pm 0.07$  MeV and

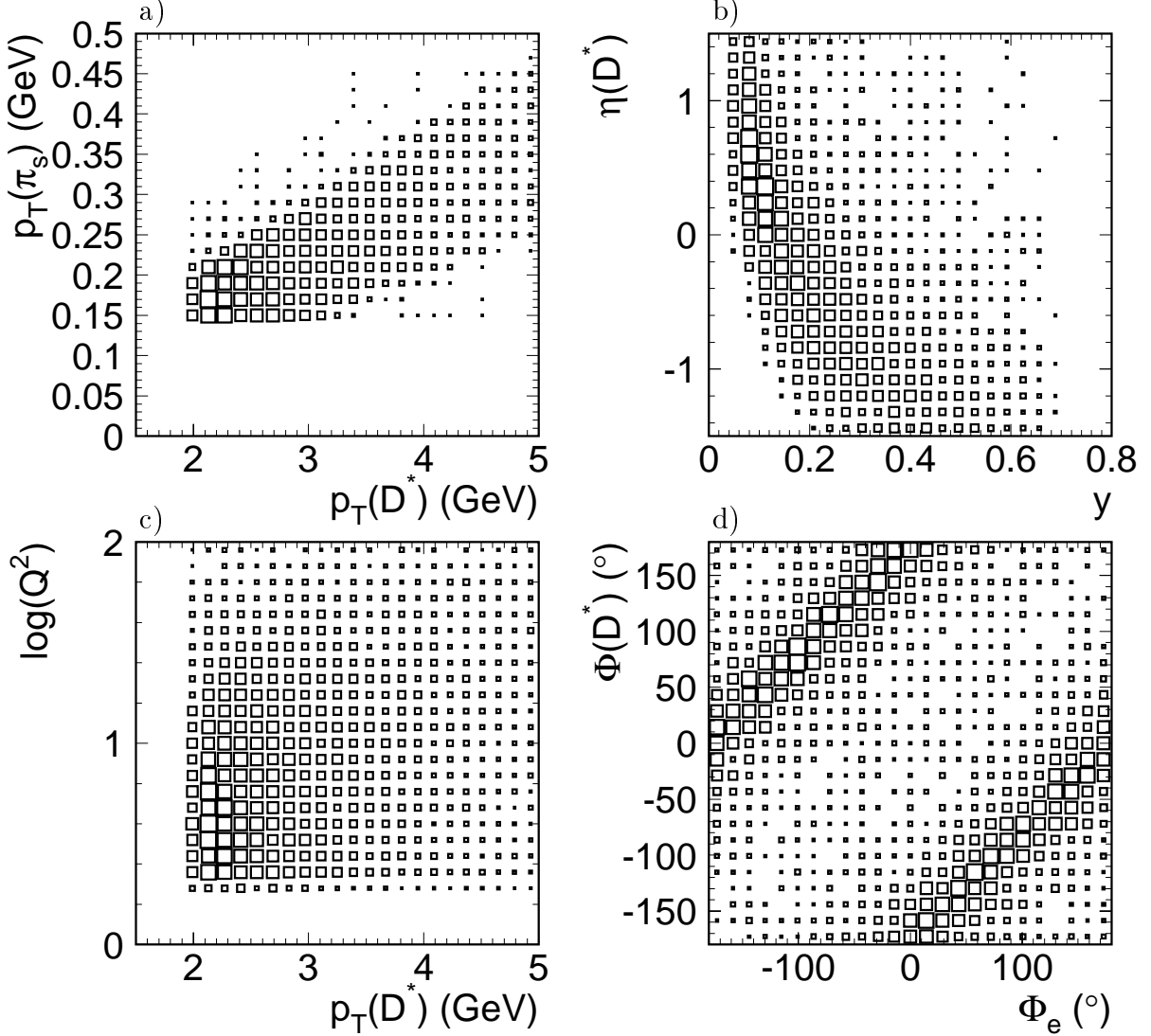


**Figure 3.3:** Correlation between the kinematic variables a)  $p_T(D^*)$  and  $p_T(\pi_s)$ , b)  $y$  and  $\eta(D^*)$ , c)  $p_T(D^*)$  and  $Q^2$  and d) between  $\phi_e$  and  $\phi(D^*)$ , as predicted by the simulation of inclusive  $D^*$  events generated with AROMA.

the width  $\sigma$  is  $1.12 \pm 0.06$  MeV. The results of the fit together with the results of the individual fits to the  $D^*$  samples of the years 95, 96 and 97 are summarized in Table 3.4.

### 3.4 Selection of diffractive events

In this section the selection of events of the form  $ep \rightarrow e(D^*X)Y$  is described. The hadronic final state is decomposed into two distinct systems,  $X$  and  $Y$  with the masses  $M_X$  and  $M_Y$  (see Section 1.4 and Figure 1.5). These two systems are separated by the largest region in pseudorapidity in which no hadrons are observed. Such events are referred to as *rapidity-gap* events. The gap indicates that a colorless object was exchanged between the systems  $X$  and  $Y$ . No strings of color flux connect the two parts of the hadronic final state and no energy deposition in the forward region is expected if the system  $Y$  has a

low mass. Thus the absence of signals in detector components, which are located in the forward part of the H1 apparatus and have acceptance at large values of pseudorapidity, characterizes diffractive events experimentally. These detector components are the liquid argon calorimeter LAr (Section 2.2.5), the forward muon system FMD and the proton remnant tagger PRT, see Sections 2.2.7 and 2.2.7.

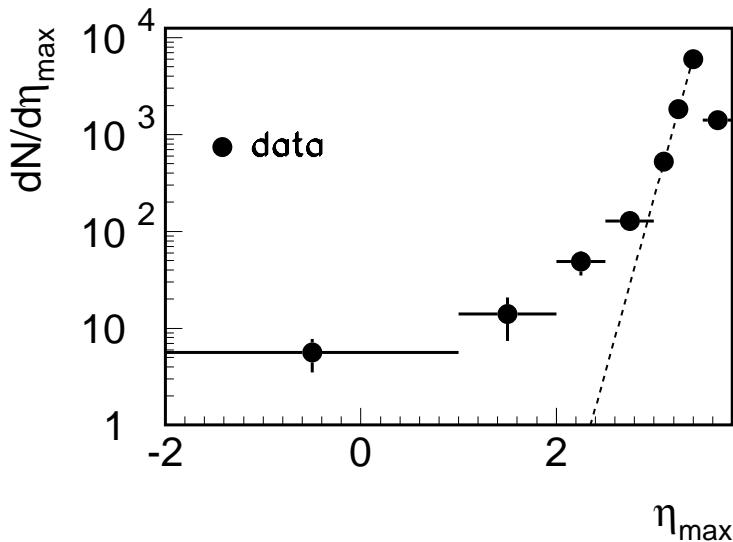


**Figure 3.4:** Number of  $D^*$  candidates as a function of  $\eta_{max}$ . No forward cuts are applied. The dashed line illustrates the exponential fall expected for non-diffractive events.

### 3.4.1 Forward cuts

In this analysis an event is called diffractive when it fulfills the *forward cuts*. These cuts are defined by the three requirements:

- $\eta_{max} < 3.3$ , where  $\eta_{max}$  measures the rapidity-gap in the outgoing proton direction and is defined as the pseudorapidity of the most forward cluster in the LAr with energy  $E > 300$  MeV. Clusters can be detected up to  $\eta_{max} \approx 3.5$ , at the lower edge of the LAr.
- Not more than one hit-pair in the three pre-toroid layers of the FMD,  $N_{FMD} \leq 1$ .
- No hit in any scintillator of the PRT,  $N_{PRT} = 0$ .

The quantity  $\eta_{max}$  measures the size of the rapidity-gap between the final state proton and the system  $X$ . The energy threshold of 300 MeV excludes the majority of random noise in the LAr. The cut  $\eta_{max} < 3.3$  provides good acceptance and is the same which was used for the measurements of the diffractive structure function  $F_2^{D(3)}$  [25]. Figure 3.4 shows the number of  $D^*$  candidates as a function of  $\eta_{max}$ . The distribution shows a tail to low values of  $\eta_{max}$ . The dashed line illustrates the exponential fall expected for

non-diffractive  $D^*$  mesons in DIS as for example predicted by the AROMA Monte Carlo without soft color interaction. The FMD is sensitive to particles from the proton remnant that scatter in the beam pipe wall or in the collimators. Only hit-pairs  $N_{FMD}$  detected in the pre-toroidal layers are counted since they are shielded by the iron toroid against synchrotron radiation from the incoming positron. The noise level for hit-pairs, that can be obtained from random triggered events, is approximately 25% (see Section 4.1.1). Therefore the selection tolerates one measured hit-pair to avoid large event losses. The PRT was designed to veto proton dissociative events by detecting particles in the very forward direction. The noise level in the PRT is found to be negligible and an event is rejected if a signal in any of the seven scintillators is measured.

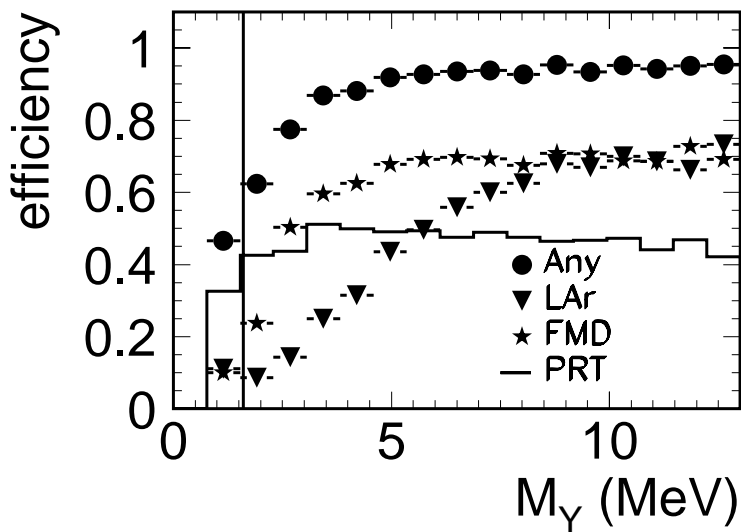


**Figure 3.5:** Acceptance for tagging the dissociated proton as a function of  $M_Y$  as predicted by the simulation of  $\rho$  meson events generated with DIFFVM. Shown are the acceptances of the Forward Muon Detector FMD, the Proton Remnant Tagger PRT, the LAr calorimeter ( $\eta_{max} < 3.3$ ) and any of the three forward detectors.

### 3.4.2 Diffractive kinematic region

The forward cuts restrict the mass  $M_Y$  of the dissociative system  $Y$ . Figure 3.5 and 3.6 show the acceptance of the forward cuts for simulated events, which were generated with the Monte Carlo Generator DIFFVM [72, 73]. This generator provides a detailed description of the proton dissociative final state. In Figure 3.5 the acceptance for tagging the dissociated proton as a function of  $M_Y$  is plotted for the different detector components. The curve labeled *Any* means that any of the components have tagged the event where the curve labeled *LAr* shows the detection efficiency of the cut  $\eta_{max} < 3.3$ . It should be noted that for values of  $M_Y \gtrsim 3$  GeV the acceptance is greater than 90% but decreases steeply towards lower values. At  $M_Y = 1.6$  GeV the acceptance is about 50 – 60%. The dotted curve in Figure 3.6 shows that the acceptance for tagging dissociative events as a function of  $|t|$  is above 80% just slightly dropping to about 70% at  $|t| = 0$  GeV<sup>2</sup>. The

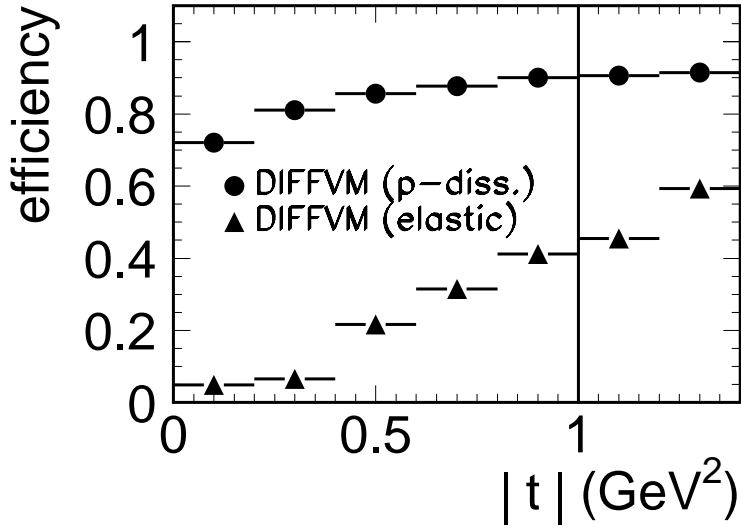


**Figure 3.6:** Comparison of the acceptance of the forward cuts as a function of  $|t|$  for proton dissociative (dots) and elastic (triangles) events. The kinematic cuts in  $M_Y$  and  $|t|$  are indicated.

distribution marked by triangles shows the acceptance for purely elastic DIFFVM events, where  $M_Y = m_p$  holds. With rising values of  $|t|$  the tagging efficiency reaches approximately 40% at  $|t| = 1 \text{ GeV}^2$ . This threshold is not particularly sharp but one should note that the cross section falls steeply as  $d\sigma/d|t| \sim e^{-b|t|}$  where  $b \approx 6 \text{ GeV}^{-2}$ . From the plots one can conclude that it is not possible to distinguish genuine elastic events from those where the proton scatters diffractively into a low mass state. Therefore all cross section measurements presented in this thesis are restricted to the diffractive kinematic region:

$$M_Y < 1.6 \text{ GeV} \quad (3.6)$$

$$|t| < 1 \text{ GeV}^2 \quad (3.7)$$

Figure 3.7 shows the correlation between  $x_P$  and  $\eta_{max}$ , as predicted by the simulation of events generated with RAPGAP. In this analysis  $x_P$  is restricted to the kinematic range

$$x_P < 0.04 \quad (3.8)$$

When neglecting the rest masses the four-momenta of the incoming positron and proton are  $l = (0, 0, -E_e, E_e)$  and  $p = (0, 0, E_p, E_p)$  and one can write

$$X_{e'} = (x_P \cdot p + l) \quad (3.9)$$

where  $X_{e'} = (p_x^{Xe'}, p_y^{Xe'}, p_z^{Xe'}, E^{Xe'})$  is the four-momentum of the hadronic system  $X$  including the scattered positron  $e'$ . Multiplying Equation 3.9 with  $l$  leads to

$$x_P = \frac{l \cdot X_{e'}}{l \cdot p} = \frac{E^{Xe'} + p_z^{Xe'}}{2 \cdot E_p} \quad (3.10)$$

which is equivalent to

$$x_P = \frac{\sum_{Xe'}(E + p_z)}{2 \cdot E_p} \quad (3.11)$$

when summing over all particles of the hadronic system  $X$  including the scattered positron. This formula is less sensitive to energy losses in the reconstruction of  $M_X$  and to initial state radiation than the relation  $x_P = (Q^2 + M_X^2)/(Q^2 + W^2)$  [75] (see Section 1.4) and is therefore used in this analysis for the reconstruction of  $x_P$ . To build the sum in Equation 3.11 again a combination of tracks and calorimeter clusters is used (see Section 3.2.1).

As can be seen from Figure 3.8(a), a good correlation of the generated (and on the hadron level calculated)  $x_P$  and the reconstructed  $x_P$  is achieved for RAPGAP events. The resolution  $\delta x_P = (x_P^{rec} - x_P^{gen})/x_P^{gen}$  is plotted in Figure 3.8(b) and is about 20%. The small shift in  $\delta x_P$  of 4.5% indicates only small losses in the measurement of the hadronic energy of system  $X$ .

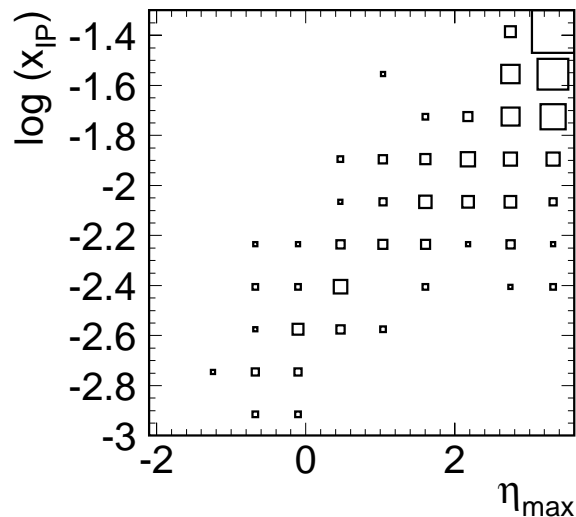


**Figure 3.7:** Correlation between  $x_P$  and  $\eta_{max}$  as predicted by the simulation of RAPGAP events.

### 3.4.3 Diffractive $D^*$ production

Figure 3.9 shows the  $D^*$  signal which is obtained when applying all diffractive cuts in addition to the selection cuts listed in Table 3.2. The number of diffractively produced  $D^*$  mesons in the kinematic range  $x_P < 0.04$ ,  $M_V < 1.6$  GeV and  $|t| < 1$  GeV<sup>2</sup> is  $N_{D^*} = 41 \pm 9$  and is extracted from a fit to the  $\Delta M$  distribution as described in Section 3.3.2. The position and the width of the Gaussian is fixed to the values taken from the high statistics, inclusive sample, see Figure 3.2 and Table 3.4. Figure 3.10 and 3.11 show a side and front view of a diffractive event with a  $D^*$  candidate. The event<sup>3</sup>, which was taken

<sup>3</sup>H1 run 195601 event 78029

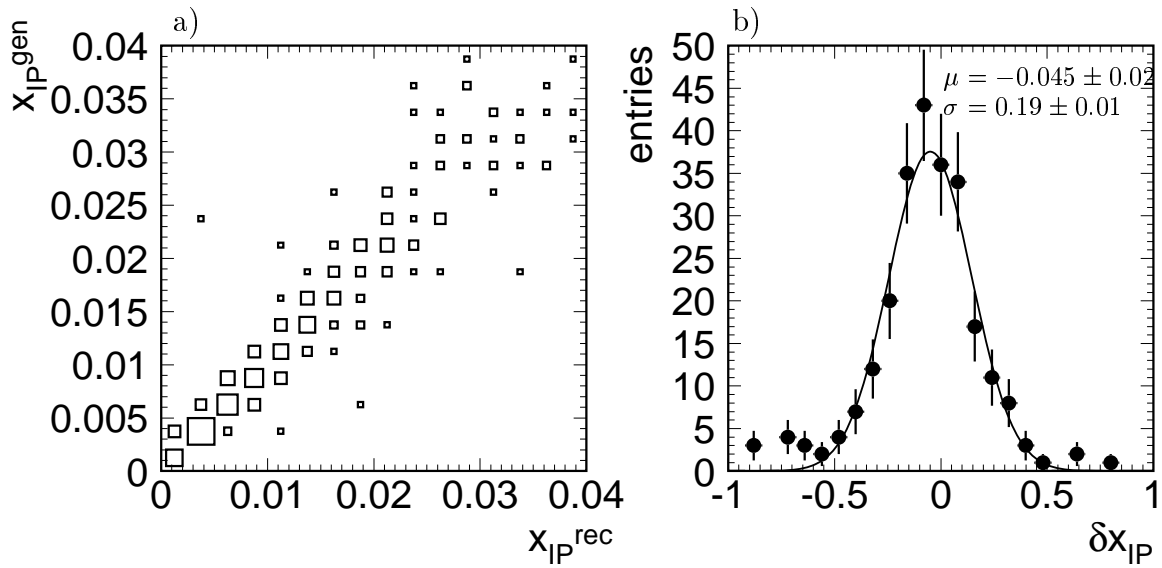


**Figure 3.8:** a) shows the correlation of the generated and reconstructed  $x_P$ . In (b) the resolution is estimated from a fit to the distribution  $\delta x_P = (x_P^{rec} - x_P^{gen})/x_P^{gen}$ . The mean  $\mu$  and the width  $\sigma$  of the Gaussian are given.

during the 1997 running period, shows the typical signature of diffraction. No signals are measured in the forward muon system and the proton remnant tagger, which are not shown in the schematic view.

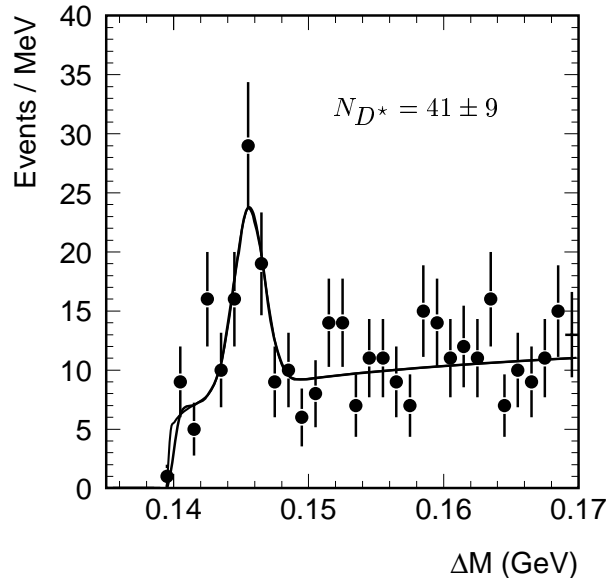


**Figure 3.9:** Total diffractive  $D^*$  signal. The solid line represents the result from the fit as described in Section 3.3.2 with a fixed position and width of the Gaussian to the values of the inclusive  $\Delta M$  distribution (see Figure 3.2 and Table `refincls:tab`). The number of diffractive  $D^*$  mesons in the kinematic range  $x_P < 0.04$ ,  $M_Y < 1.6$  GeV and  $|t| < 1$  GeV<sup>2</sup> is  $N_{D^*} = 41 \pm 9$ .

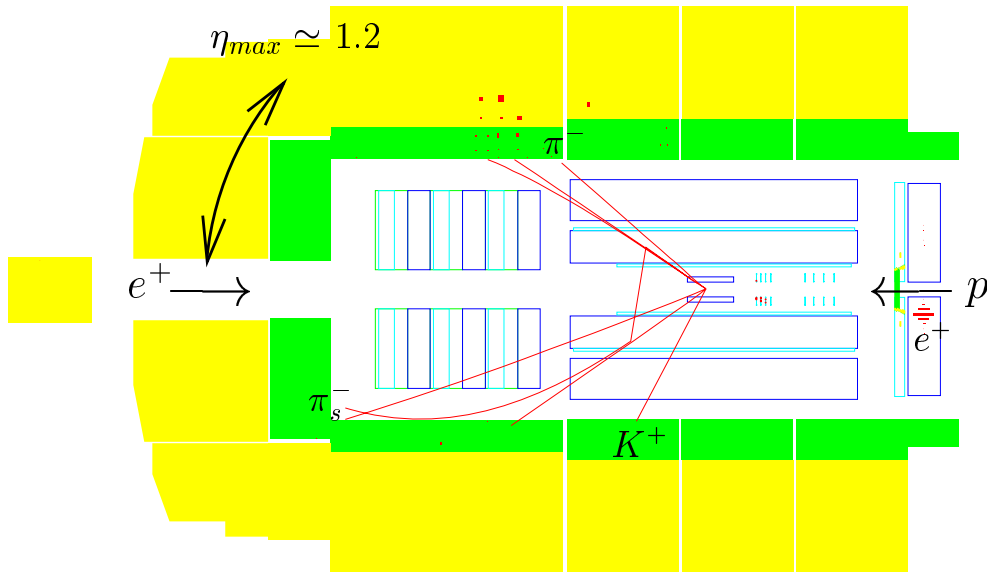


**Figure 3.10:** Side view of a diffractive event with a  $D^*$  candidate. The forward detectors *PRT* and *FMD*, which are not shown, have no activity.

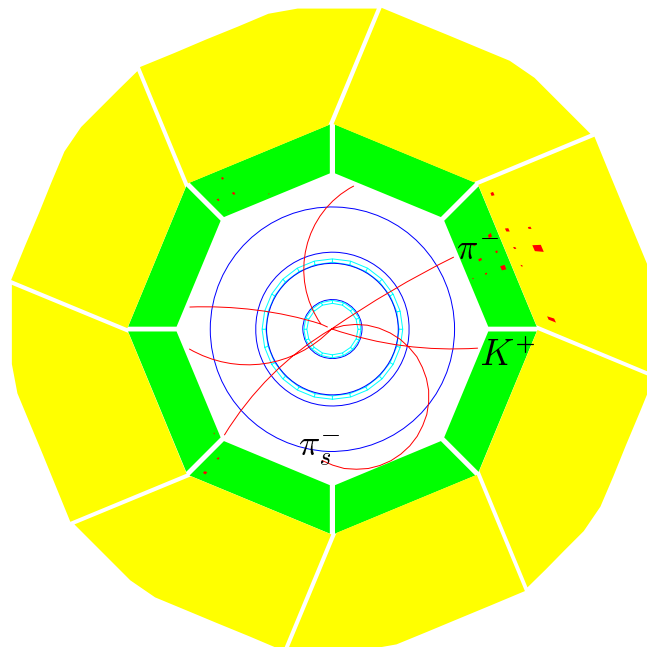


**Figure 3.11:** Front view of a diffractive  $D^*$  candidate.

# Chapter 4

## Cross Section Measurement

In the previous chapter the selection procedure of diffractive  $D^*$  mesons in deep inelastic scattering has been established. This chapter starts by introducing the method used to determine the cross section. After the explanation of the corrections that are applied to the observed number of diffractive charm events the systematic uncertainties on the cross sections are discussed. Finally the results are presented in comparison with the models for diffractive charm production.

### 4.1 Determination of the cross section

The diffractive cross section is calculated using the formula:

$$\sigma(ep \rightarrow e(D^* X)Y) = \frac{N_{D^*} \cdot (1 - r)}{\mathcal{L}_{int} \cdot BR \cdot \varepsilon_{trig} \cdot A \cdot \nu \cdot S} \quad (4.1)$$

where

$N_{D^*}$  is the number of  $D^*$  mesons obtained from a maximum likelihood fit to the  $\Delta M$  distribution as described in Section 3.3.

$r$  is the fraction of events from mass reflections. Decay channels other than the one analyzed can contribute to the  $\Delta M$  signal and hence to  $N_{D^*}$ .

$\mathcal{L}_{int}$  is the integrated luminosity of  $21.72 \text{ pb}^{-1}$ , see Section 2.2.2.

$BR$  is the branching fraction of the measured decay mode  $D^* \rightarrow D^0 \pi_s \rightarrow (K\pi)\pi_s$  and the value of 2.63% (see Table 3.3) is used.

$A$  is the detector acceptance and the efficiency of the reconstruction and the selection cuts as determined from the Monte Carlo simulation.

$\varepsilon_{trig}$  is the efficiency of the used subtriggers as determined from the Monte Carlo simulation.

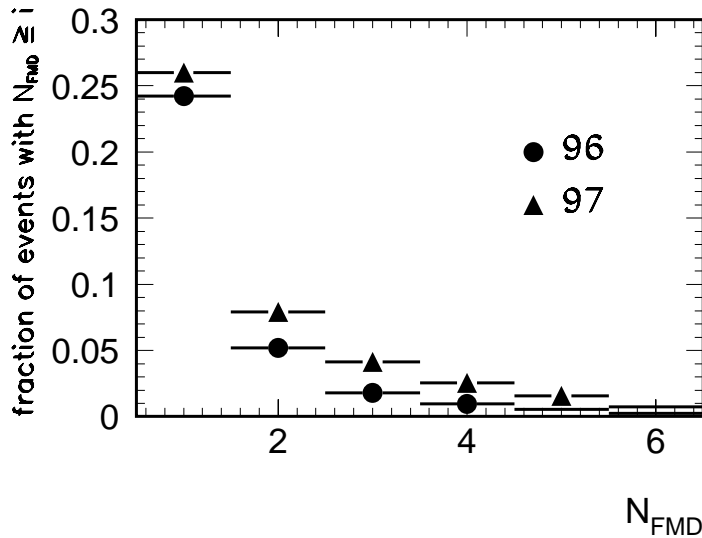


**Figure 4.1:** Noise level in the forward muon detector. The noise level in bin  $i$  refers to the fraction of events which have  $i$  or more hits  $N_{FMD}$  in the pre-toroid layers of the FMD.

$\nu$  is a correction accounting for event losses due to noise in the forward detectors.  $\nu$  is determined using random triggered events.

$S$  is a correction due to smearing of events across the boundary  $M_\gamma = 1.6$  GeV.  $S$  is estimated using a special simulation of the dissociating proton remnant, since this, in contrast to the smearing in other cut variables, is not included in the standard Monte Carlo simulation used to calculate the acceptance.

#### 4.1.1 Noise correction $\nu$

In this analysis the detector components such as the liquid argon calorimeter LAr, the forward muon detector FMD and the proton remnant tagger PRT are used to identify diffractive events, see Section 3.4. A diffractive event may be rejected coincidentally by the forward cuts due to noise caused by either beam backgrounds or electronic noise. In contrast to the LAr, where the noise is implemented in the detector simulation, the noise in the FMD and PRT is not simulated and a correction  $\nu$  to the acceptance has to be applied. Figure 4.1 shows the noise level for hit-pairs in the three pre-toroid layers of the FMD during the years 96 and 97 obtained from a sample of random read-outs of the detector. The noise level in 95 is found to be slightly lower than in 96 and 97 [74]. The loss of diffractive events due to noise fluctuations in the FMD is below 8% when one hit pair is allowed by the selection. In each of the three years the noise level in the PRT is found to be less than 1% and thus is neglected. The corrections  $\nu$  that are applied to the data samples of 95, 96 and 97 are quoted in Table 4.3.

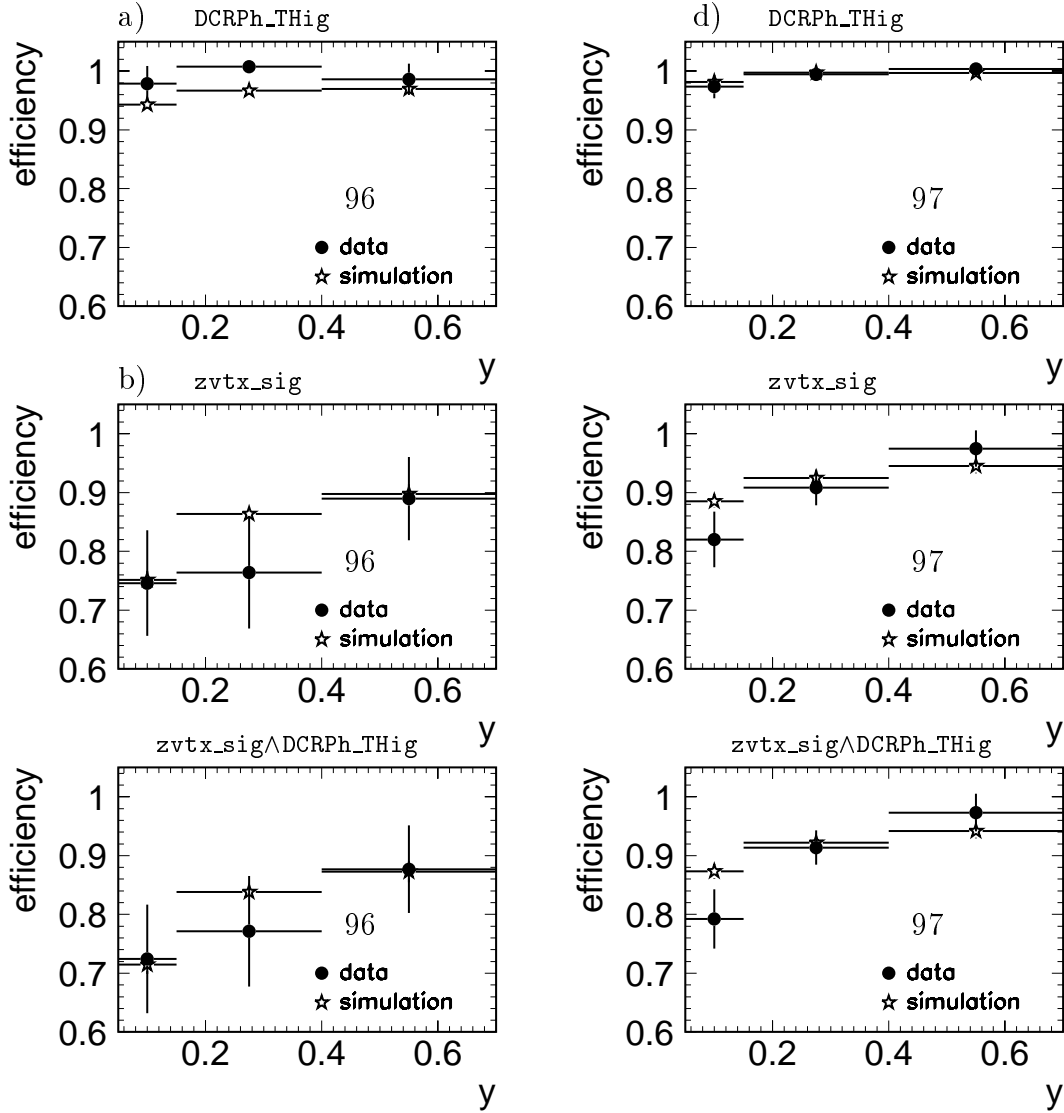


Figure 4.2: Trigger efficiencies 96 and 97.

### 4.1.2 Reflections

Decay channels other than  $D^* \rightarrow D^0 \pi_s \rightarrow (K\pi)\pi_s$  can contribute to the  $\Delta M$  signal. These contributions are referred to as *reflections* and are determined using events generated with AROMA. Events where the  $D^*$  decays into other particles than in the analyzed decay mode were simulated and passed through the same reconstruction method described in Section 3.3.  $D^0$  mesons from the decays  $D^0 \rightarrow K^- K^+$  and  $D^0 \rightarrow \pi^+ \pi^-$  can pass the cut  $\pm 80$  MeV around the nominal mass of the  $D^0$ . If the  $D^0$  is produced by  $D^* \rightarrow D^0 \pi$  decays and the wrong  $K$  or  $\pi$  mass hypothesis is assigned to one of the decay products, the  $\Delta M = M(K, \pi, \pi_s) - M(K, \pi)$  distribution peaks around 145.4 MeV. The main contribution to the  $\Delta M$  signal is due to the misidentification of such decays and a correction of  $r = (3.5 \pm 1.5)\%$  is made. Appendix A gives a detailed description of the determination of the reflection background.

Trigger efficiency (%)	96		97	
	Data	Simulation	Data	Simulation
DCRPh_THig	$98.9 \pm 1.3$	$95.9 \pm 0.5$	$98.8 \pm 0.8$	$99.2 \pm 0.2$
zvtx_sig	$78.4 \pm 5.2$	$83.0 \pm 0.9$	$88.6 \pm 2.4$	$91.5 \pm 0.6$
zvtx_sig $\wedge$ DCRPh_THig	$77.3 \pm 5.3$	$80.0 \pm 0.8$	$87.9 \pm 2.4$	$90.8 \pm 0.6$

**Table 4.1:** Trigger efficiencies 96 and 97.

### 4.1.3 Trigger efficiency

The data used for the cross section measurement were triggered on the first trigger level L1 by subtrigger s2. The trigger condition requires a signal from the inclusive electron trigger (Spcl\_e\_IET>1) in coincidence with a charged track signal from both the  $z$ -vertex trigger (zvtx\_sig) and the  $DCr\phi$ -trigger (DCRPh\_THig) (see Section 3.1.1). The maximum energy threshold of the inclusive electron trigger has been 6 GeV which is well below the applied cut on the energy of the scattered positron of 9 GeV during the years 95, 96 and 97 and is therefore expected to be  $\approx 100\%$  [76] and neglected in this analysis. The systematic uncertainty of the IET efficiency is 1% [53].

The efficiency for the track trigger conditions zvtx\_sig and DCRPh\_THig is taken from the detector simulation. For the 95 data sample a weaker condition was applied, which had an efficiency of  $\approx 100\%$  and was found to be in good agreement with the Monte Carlo simulation [67]. Figure 4.2 shows the efficiency for the years 96 and 97 as a function of  $y$  calculated from the data and as predicted by the RAPGAP Monte Carlo. The efficiencies of the individual conditions DCRPh\_THig (a) and zvtx\_sig (b) and the combination of both (c) are shown. The efficiencies are calculated from the data as the ratio of the number of  $D^*$  mesons triggered by both the track independent *monitor trigger* and the track trigger condition to the number of  $D^*$  mesons triggered by the monitor trigger only. Thereby the number of  $D^*$  mesons is obtained from the  $\Delta M$ -fit. To increase statistics, no diffractive selection is applied. Since the Monte Carlo predicts the trigger efficiency to be the same for diffractive and non-diffractive events, this cross check holds for the diffractive case, too. The efficiency of the  $DCr\phi$ -trigger obtained from the data is  $\approx 99\%$  for the data samples of 96 and 97 where the latter is well modelled by the simulation. In 96 the Monte Carlo slightly underestimates the  $DCr\phi$  efficiency. For the 97 data taking the zvtx\_sig criterion has been especially tuned for triggering  $D^*$  mesons [67] resulting in a higher efficiency for both the data and the simulation. Since forward rays combined from the signals of the CIP and FPC (see Section 2.2.8) have a poorer  $z$ -resolution than central rays defined by CIP and COP the zvtx\_sig efficiency drops with decreasing values of  $y$  where the hadronic final state is predominantly boosted in the forward direction. Within the accuracy limited by the monitor trigger statistics in the data the simulation of the combined  $z$ -vertex and  $DCr\phi$ -trigger requirement gives a fair description of the efficiency. The results of the average trigger efficiencies are summarized in Table 4.1. An uncertainty of the trigger efficiency of 6% is estimated using the maximum difference between the data and the simulation for the DCRPh\_THig and zvtx\_sig trigger elements, observed for 96,

Selection cuts		Efficiency (%)	
	Number of generated $D^*$ mesons in kinematic range	relat. to previous	total
			100
1	DIS, $D^*$ selection and $x_p < 0.04$	78.1	78.1
2	$\eta_{max} < 3.3$	73.1	57.1
3	$N_{FMD} \leq 1$ and $N_{PRT} = 0$	94.9	54.2
4	$z(D^*) > 0.2$ if $p_T(D^*) < 3$ GeV	87.6	47.5
5	Subtrigger: Spcle_IET $\wedge$ zvtx_sig $\wedge$ DCRPh_THig	89.1	42.3
6	$\nu \times S$	96.5	<b>40.8</b>

**Table 4.2:** Efficiency of the consecutively applied selection cuts as predicted by the simulation of RAPGAP  $D^*$  events. The number of the respective selection step corresponds to the histograms in Figure 4.3 where the efficiencies are plotted in the same bins of variables for which differential cross sections are measured. For further explanations see Section 4.1.4.

added in quadrature.

#### 4.1.4 Acceptance and reconstruction efficiency

Monte Carlo simulations are used to correct the data for the effects of event losses and migrations due to the limited acceptance and reconstruction efficiency of the detector. Therefore a sample of events containing  $D^*$  mesons decaying into the analyzed decay mode has been generated using the generator RAPGAP, where the resolved pomeron model has been used to produce diffractive charm events (see Section 1.5.1). Since RAPGAP models elastic diffractive events in the kinematic range  $x_p < 0.1$  and  $M_Y = m_p$  a  $D^*$  event sample generated with AROMA is used to model the kinematic region  $x_p > 0.1$  or  $M_Y > 5$  GeV. DIFFVM events are used to model low mass dissociation ( $m_p < M_Y < 5$  GeV) in order to describe the full phase space (see Section 4.1.5). The events are passed through the 95, 96 and 97 detector simulation. The acceptance and reconstruction efficiency is calculated as the ratio of the number of  $D^*$  mesons reconstructed in the visible kinematic range to the number of  $D^*$  mesons generated in the kinematic region. This method accounts for both losses, where the  $D^*$  meson is not reconstructed and the event is rejected, and migrations. Even though a  $D^*$  meson is generated outside it can migrate inside the required kinematic range due to resolution effects at the kinematic boundaries.

The efficiencies of the consecutively applied selection cuts as determined from the RAPGAP simulation are listed in Table 4.2. Ratios are given for both events passing the current selection step compared to the previous sample and compared to the original sample of events generated in the measured kinematic range. For the measurement of differential cross sections the efficiency is calculated bin-wise and the result for various

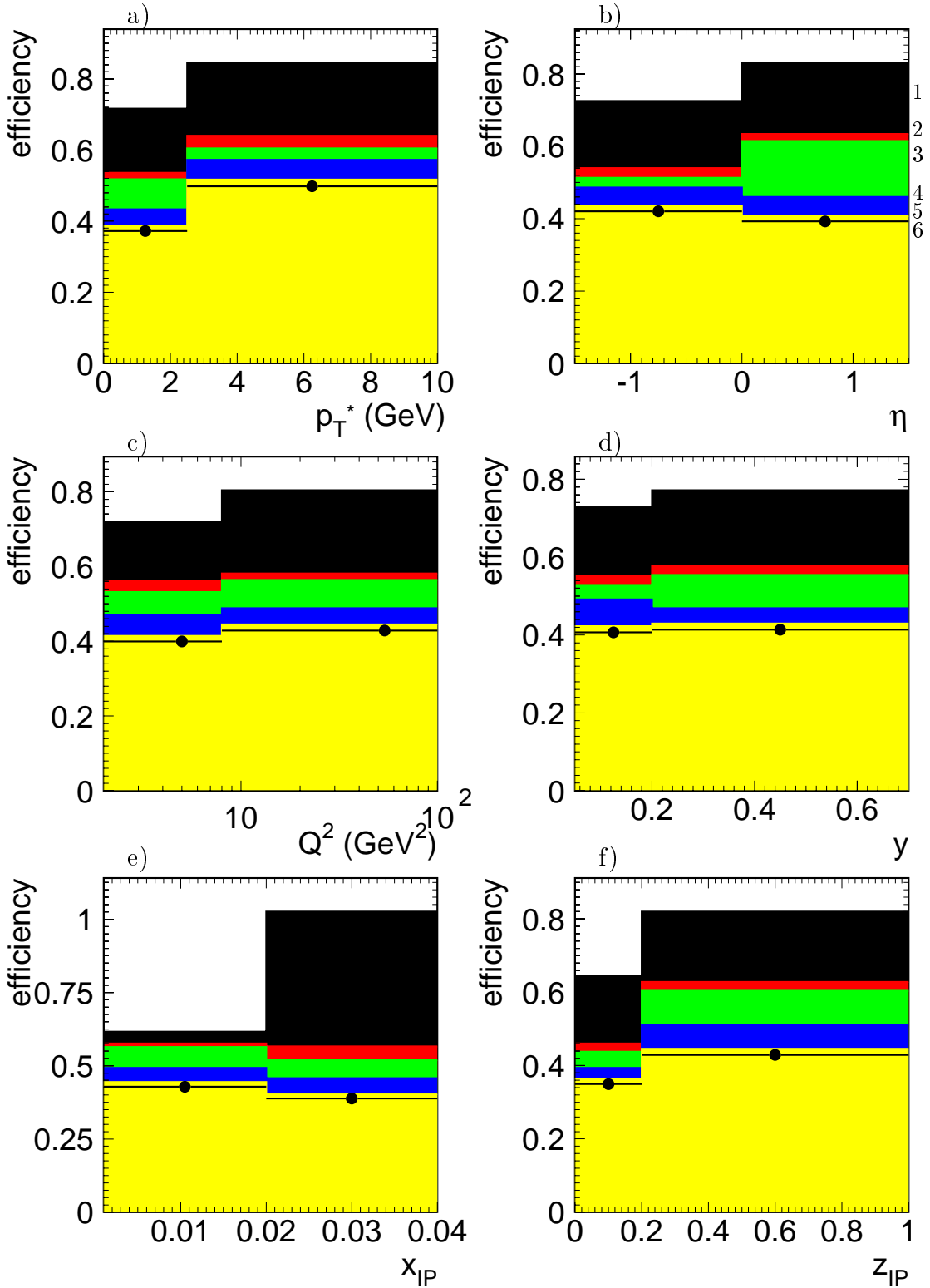


**Figure 4.3:** Efficiency of selection cuts as a function of (a)  $p_T^*$ , (b)  $\eta$ , (c)  $Q^2$ , (d)  $y$ , (e)  $x_{IP}$  and (f)  $z_{IP}$  as determined from RAPGAP. The given numbers refer to the selection step (see Table 4.2 and Section 4.1.4). The points represent the final, combined correction  $\varepsilon_{trig} \cdot A \cdot \nu \cdot S$  (compare Equation 4.1) for the measurement of the differential cross sections.

kinematic variables is shown in Figure 4.2. In step 1 the selection of good positron candidates measured in the kinematic range of DIS events is performed. The track quality cuts are applied and the  $D^*$  mesons are reconstructed in the visible range  $p_T(D^*) > 2$  GeV and  $|\eta(D^*)| < 1.5$ . The diffractive kinematic range is restricted to  $x_P < 0.04$ . Slightly more events than generated are reconstructed in the region  $0.02 < x_P < 0.04$ , which is reflected in Figure 4.2(e) where the efficiency is greater than one in the second bin of the distribution. These migrations are due to the limited resolution for large values of  $x_P$  (see Figure 3.8). The events are rejected by the forward cuts  $\eta_{max} < 3.3$  (step 2),  $N_{FMD} \leq 1$  and  $N_{PRT} = 0$  (step 3). The efficiency after applying the  $z(D^*)$  cut (step 4) is 47.5%. The subtrigger condition is required in step 5 and is multiplied in step 6 by the corrections due to noise  $\nu$  and  $M_Y$  smearing  $S$  (see Table 4.3) yielding to the final, combined efficiency correction  $\varepsilon_{trig} \cdot A \cdot \nu \cdot S$  (see Equation 4.1) of 40.8%. From Figure 4.2, where the final efficiencies are represented by the points, it should be noted that no large variations are seen for any kinematic variables.

### Simulation of forward detectors

The efficiency of the forward cuts (see Section 3.4) is determined from the Monte Carlo and hence the diffractive cross section measurement depends crucially on the correct simulation of the forward detector response. Discrepancies between data and Monte Carlo are found in the response of the PRT, particularly for the 97 data sample. The efficiency of each individual scintillator of the PRT is calibrated in the simulation and additional overall correction factors for the years 95, 96 and 97 are applied accounting for remaining discrepancies between the efficiencies given by the simulation and the data. The calibration is performed using both data and Monte Carlo events with high activity in the forward region. Inclusive  $D^*$  events measured in a wider region of phase space than it is defined in this analysis are selected and the response of the forward detectors is studied in comparison to the simulation of events generated with the ARIADNE [77] Monte Carlo generator. ARIADNE gives a good description of forward particle production for DIS processes using the color dipole model [78]. Rapidity gap events are produced by a simple implementation of the resolved pomeron model. Figure 4.4 shows the response of the FMD (a), the PRT (b) and the LAr (c) for 97 data after the calibration of the PRT. An event enters the relevant histogram if the activity in both other detector components satisfies *anti-diffractive* cuts. All distributions show good agreement between data and simulation.

A detailed description of the PRT calibration method can be found in [74].

#### 4.1.5 $M_Y$ smearing $S$

The smearing  $S$  across the boundary of  $M_Y = 1.6$  GeV is determined from the simulation of proton dissociative and elastic events generated with the DIFFVM Monte Carlo. This correction can not be determined from the RAPGAP simulation because RAPGAP generates only elastic diffractive events. Events where the proton dissociates ( $M_Y > m_p$ ) are not modelled. As it has been demonstrated in Section 3.4.2 (see Figure 3.5) the diffractive

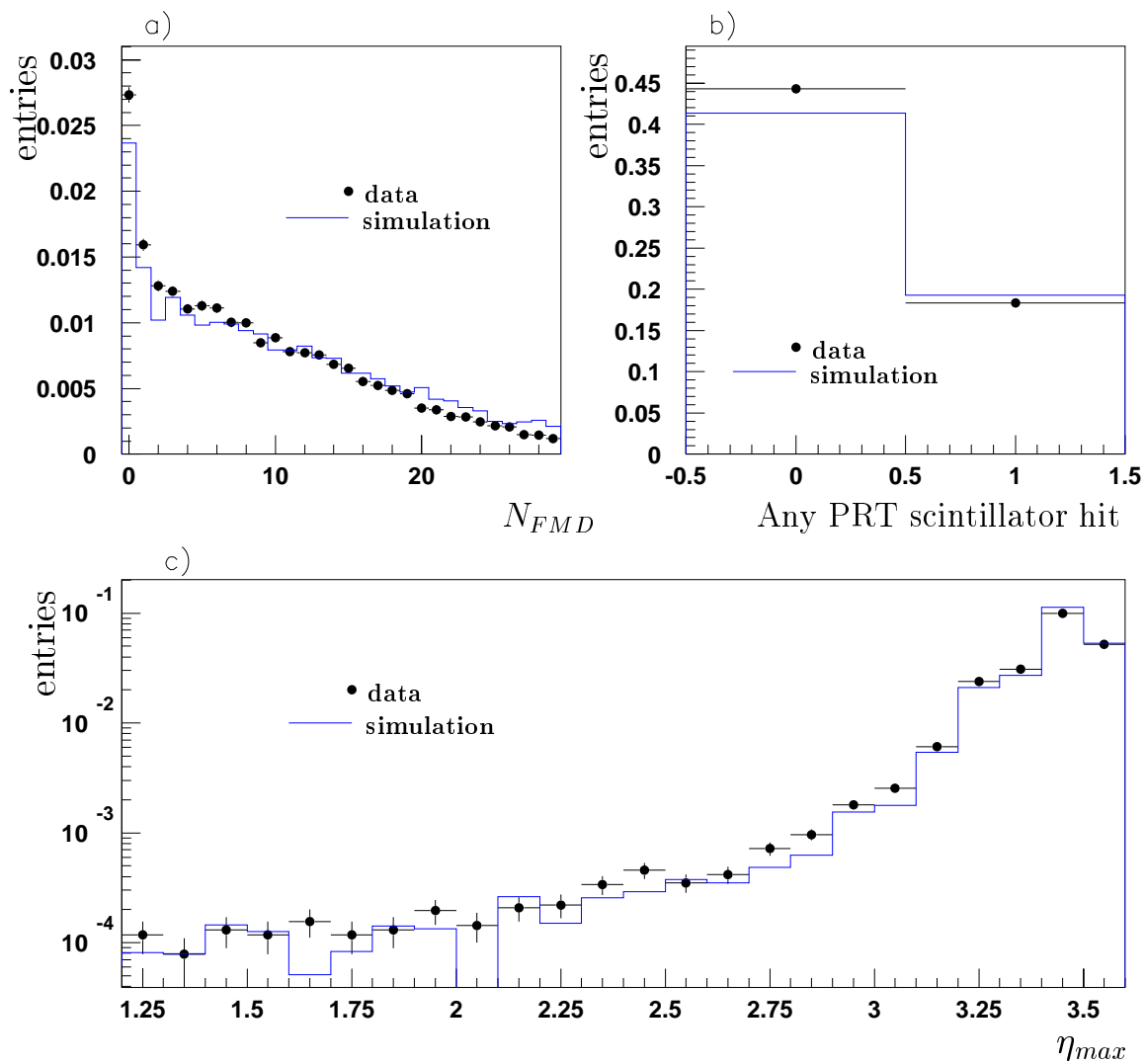


**Figure 4.4:** Comparison of the response of the forward detectors between 97 data (points) and a simulation of ARIADNE Monte Carlo (solid line). a) shows the number of pre-toroid hit-pairs in the FMD if anti-diffractive cuts  $\eta_{max} > 3.3$  and  $N_{PRT} > 0$  are applied. b) shows the activity in the PRT if  $\eta_{max} > 3.3$  and  $N_{FMD} > 1$  is fulfilled and c) the  $\eta_{max}$  distribution for events with  $N_{FMD} > 1$  and  $N_{PRT} > 0$ . The distributions are normalized to the number of events in the data passing the DIS selection. The distributions are shown after the calibration of the PRT as described in [74].

Correction	95	96	97
Noise $\nu$	0.932	0.923	0.922
$M_Y$ smearing $S$	$1.032 \pm 0.038$	$1.040 \pm 0.043$	$1.076 \pm 0.062$

**Table 4.3:** Noise and  $M_Y$  smearing corrections for the years 95, 96 and 97.

cross section can not directly be measured for purely elastic events due to the limited acceptance of the forward detectors towards low values of  $M_Y$ . Therefore the cross section is defined in a wider range  $M_Y < 1.6$  GeV. The Monte Carlo generator DIFFVM predicts a reduction of the cross section of  $\approx 8\%$  when this cut is changed to  $M_Y = m_p$  if the ratio of the proton elastic to the proton dissociative cross section equals one. This factor increases to  $\approx 30\%$  without any forward detectors information.

The correction  $S$  is calculated using the formula:

$$S = 1 - \frac{N_{gen}^{pd} - N_{rec}^{pd}}{N_{gen}^{pd} + (R \cdot N_{gen}^{el})} \quad (4.2)$$

where  $N_{gen}^{pd}$  ( $N_{rec}^{pd}$ ) is the number of dissociative events generated (reconstructed) in the kinematic range  $M_Y < 1.6$  GeV and  $|t| < 1$  GeV<sup>2</sup>.  $R \cdot N_{gen}^{el}$  is the number of generated elastic events weighted by the ratio  $R$  of the elastic to the proton dissociative cross section. The correction factors and the related systematic errors for the years 95, 96 and 97 are given in Table 4.3. For the correction factors  $S > 1$  holds which reflects an inward migration into the range  $M_Y < 1.6$  GeV. The uncertainty in the correction  $S$  is estimated by varying

- the ratio of proton elastic to proton dissociative cross sections to either 1:2 or 2:1, so that the range covers that measured in various proton dissociation processes in both fixed target and DIS experiments [79, 80, 81].
- the generated  $M_Y$  distribution by  $1/M_Y^{2 \pm 0.3}$ ,
- the simulated  $t$  dependence ( $d\sigma/d|t| \sim e^{-b|t|}$ ) by changing the slope parameter of the distribution in the proton dissociation simulation by  $\pm 1$  GeV<sup>-2</sup> and  $\pm 2$  GeV<sup>-2</sup> for the proton elastic simulation around the central value of  $\approx 6$  GeV<sup>-2</sup>,
- and the efficiency of the forward detectors based on the studies in [74]. The efficiency of the FMD is altered by  $\pm 4\%$  and the value of the overall correction made in the calibration of the PRT is varied by  $\pm 100\%$ .

All systematic uncertainties are added in quadrature.

#### 4.1.6 Cross check with the inclusive measurement

The inclusive cross section  $\sigma(ep \rightarrow eD^*X)$  can be measured according to Equation 4.1. The forward cuts are omitted in the event selection and no corrections due to noise and

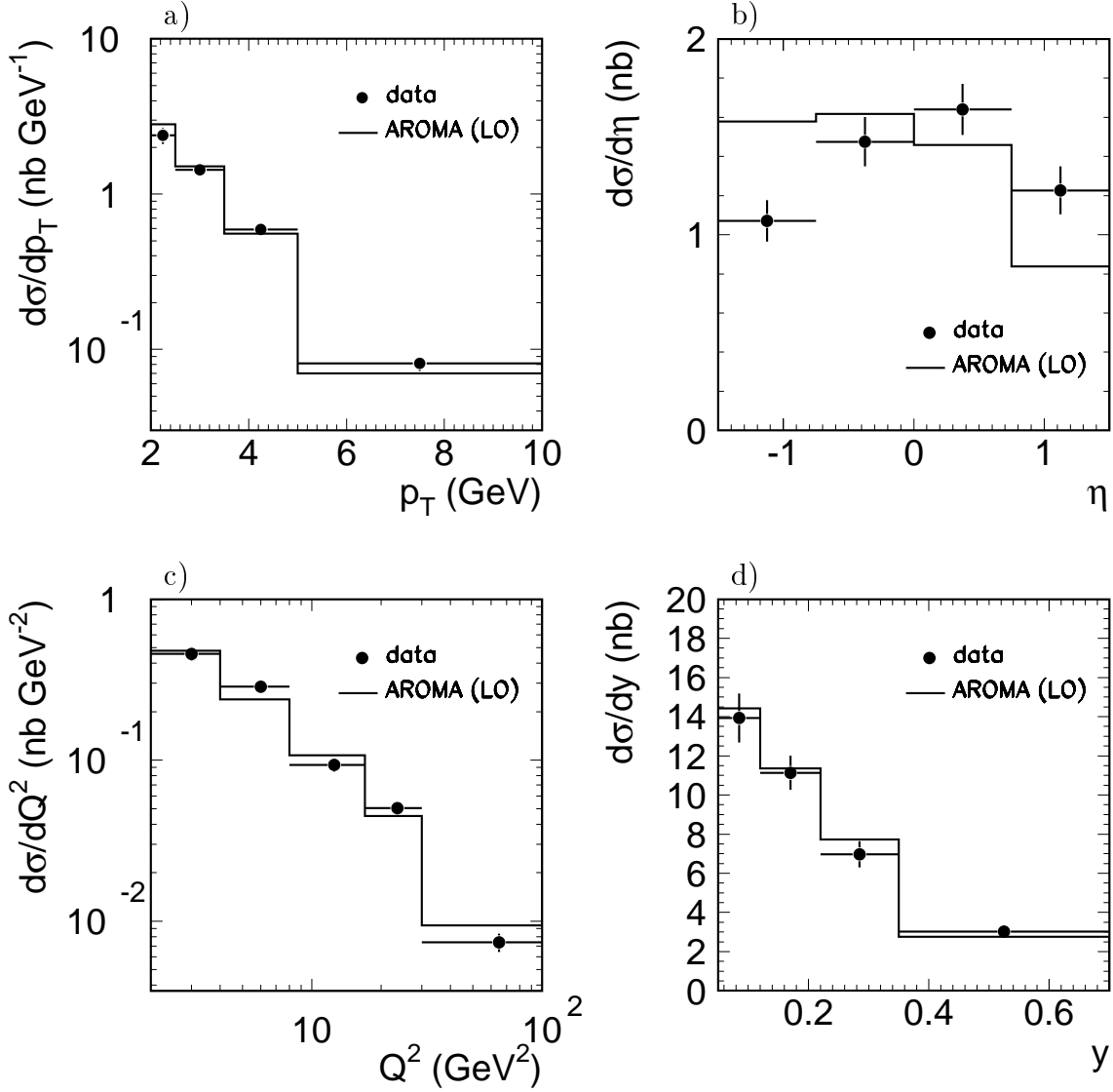


**Figure 4.5:** Inclusive cross sections  $\sigma(ep \rightarrow eD^*X)$  as a function of (a)  $p_T$ , (b)  $\eta$ , (c)  $Q^2$  and (d)  $y$ . The data are shown as full points with statistical errors and are compared to the leading order AROMA prediction represented by the solid line.

$M_Y$  smearing are applied. The efficiency for the positron and  $D^*$  reconstruction and the trigger efficiency are determined from the AROMA Monte Carlo simulation. The total number of inclusive  $D^*$  mesons measured is  $N_{D^*} = 1015 \pm 55$ , see Section 3.3.2. The corresponding cross section in the kinematic range  $2 < Q^2 < 100 \text{ GeV}^2$ ,  $0.05 < y < 0.7$ ,  $p_T(D^*) > 2 \text{ GeV}$  and  $|\eta(D^*)| < 1.5$  is

$$\sigma(ep \rightarrow eD^*X) = 4.06 \pm 0.19 \text{ (stat.) nb} \quad (4.3)$$

which is in good agreement with the leading order AROMA prediction of 4.12 nb. In Figure 4.5 the cross sections are presented differentially as a function of  $p_T$ ,  $\eta$ ,  $Q^2$  and  $y$ . The generated AROMA spectra give a good description of the measured  $p_T$ ,  $Q^2$  and  $y$  distribution. The discrepancy in the  $\eta$  spectrum can be reduced by altering parameters

such as the QCD scale and parton distribution functions within acceptable ranges [10]. The results of the inclusive measurement allow the conclusion that the efficiencies of the  $D^*$  and DIS selection cuts (see Table 3.2) are understood.

## 4.2 Error calculation

The statistical error of the cross section measurement is given by the error as obtained from the fit to the  $\Delta M$  distribution. Systematic uncertainties in the cross section determination have been estimated by varying the measurement conditions, in particular using the Monte Carlo simulations. For differential distributions this has been performed in each bin separately. The following sources of systematic errors are considered:

- The largest systematic error is due to uncertainties in the physics model for  $D^*$  production used to compute the acceptance corrections. This error is estimated from the difference in the acceptance calculated using the resolved pomeron model as implemented in RAPGAP and the SCI model as implemented in AROMA which have different underlying kinematic distributions. The error is 17.5% when averaged over all bins of the differential cross sections.
- In the fitting procedure the position and the width of the Gaussian is fixed to the values obtained from the inclusive sample (see Section 3.4.3). The variation of the width by  $\pm 1\sigma$  yield an error of 12% when averaging over all differential cross sections.
- The difference of the measured cross sections calculated when either applying or not applying the  $z(D^*)$  cut is used to estimate the uncertainty of its efficiency. This procedure yields an error of 9% when averaging over all differential cross sections.
- The uncertainty in the reconstruction efficiency of the central tracker for the three tracks is estimated as 7.5%.
- The uncertainty in the trigger efficiency gives a contribution of 6% to the systematic error, see Section 4.1.3.
- The uncertainty in the electromagnetic energy scale of the SpaCal of 1% (3%) at 27.5(8) GeV and the uncertainty in the angle of the scattered positron of 0.5 mrad affects the reconstruction of the event kinematics and hence leads to a systematic error of 5% when averaging over all differential cross sections.
- The average uncertainty of 5% due to the  $M_x$  reconstruction reflects a 3% uncertainty in the fraction of the final state energy contained in the tracks affecting in particular the  $x_p$  reconstruction (see Section 3.4.2) and an uncertainty in the hadronic energy scale of the LAr (4%) and SpaCal (7%) calorimeters.

- The uncertainty in the correction due to the smearing of events across the boundary of  $M_Y = 1.6 \text{ GeV}$  is estimated by varying in the DIFFVM simulation the efficiency of the proton remnant tagger and by varying the ratio of double to single dissociation as described in Section 4.1.5. This contributes 6% to the error.
- The uncertainty in the fraction of events lost due to noise in the forward detectors is estimated as 6%.
- The error of the branching fraction is 3% [68] and the uncertainty of the luminosity measurement is 1.5% [83].
- The error due to reflections is 1.5%, see Section 4.1.2.

The contamination of the  $D^*$  signal of both photoproduction events and events from beauty production are small and the uncertainty is of the order of  $\lesssim 1\%$  [10] and thus neglected in this analysis. All contributions are added in quadrature amounting to a total combined systematic error of 25%.

## 4.3 Results

### 4.3.1 Diffractive charm cross section

The total number of diffractive  $D^*$  mesons as obtained from the  $\Delta M$ -fit is  $N_{D^*} = 41 \pm 9$  (see Section 3.4.3). The corresponding diffractive cross section defined in the visible kinematic region  $2 < Q^2 < 100 \text{ GeV}^2$ ,  $0.05 < y < 0.7$ ,  $p_T(D^*) > 2 \text{ GeV}$ ,  $|\eta(D^*)| < 1.5$ ,  $x_p < 0.04$ ,  $M_Y < 1.6 \text{ GeV}$  and  $|t| < 1 \text{ GeV}^2$  is

$$\sigma(ep \rightarrow e(D^*X)Y) = (184 \pm 42 \pm 46) \text{ pb} , \quad (4.4)$$

where the first error is statistical and the second systematic.

The ratio of the diffractive to the inclusive cross section, which is defined in the same kinematic range in terms of  $Q^2$ ,  $y$ ,  $p_T(D^*)$  and  $\eta(D^*)$  (see Section 4.1.6) is  $4.5 \pm 1.0(\text{stat.})\%$ .

### 4.3.2 Comparison with models

The measured diffractive cross section is compared to the predictions of the resolved pomeron model, the two-gluon model and the soft color interaction (SCI) model in Table 4.4. For the former two models the cross sections are calculated in the measured kinematic region for various assumptions on the factorization scale  $\mu^2$ , the fragmentation scheme, the QCD scale  $\Lambda_{QCD}$ , the number of active flavors  $N_f$  and the charm quark mass  $m_c$ . For the resolved IP model the cross sections are calculated using parton distributions extracted from QCD fits to  $F_2^{D(3)}$  which are dominated by quarks (fit 1) and gluons (fit 2 and 3) at the starting scale (see Section 1.4.2 and Figure 1.9). The pomeron flux is described in terms of Regge theory where the proton can couple to a pomeron (IP) or a

Resolved pomeron model							
Scale	Frag.	$\Lambda_{QCD}$	$N_f$	$m_c$	$F_2^{D^{(3)}}$ fit	IP-flux	$\sigma$ (pb)
$\mu^2 = p_T^2 + Q^2 + 4m_c^2$	Pet.	0.25	5	1.5	2 LO	IP + IR	<b>540</b>
	Lund	0.25	5	1.5	2 LO	IP + IR	535
	Pet.	0.239	4	1.5	2 LO	IP + IR	502
	Pet.	0.25	5	1.35	2 LO	IP + IR	613
	Pet.	0.25	5	1.6	2 LO	IP + IR	478
	Pet.	0.25	5	1.5	3 LO	IP + IR	638
	Pet.	0.25	5	1.5	2 NLO	IP + IR	453
	Pet.	0.25	5	1.5	1 LO	IP + IR	60
$\mu^2 \rightarrow 1/4\mu^2$	Pet.	0.25	5	1.5	2 LO	IP + IR	536
$\mu^2 \rightarrow 4\mu^2$	Pet.	0.25	5	1.5	2 LO	IP + IR	517
$\mu^2 = 4m_c^2$	Pet.	0.25	5	1.5	2 LO	IP + IR	690
$\mu^2 = p_T^2 + 4m_c^2$	Pet.	0.25	5	1.5	2 LO	IP + IR	640
$\mu^2 = \hat{s}$	Pet.	0.25	5	1.5	2 LO	IP + IR	505
	Pet.	0.25	5	1.5	2 LO	IP	490
Two-gluon model							
Scale	Frag.	$\Lambda_{QCD}$	$N_f$	$m_c$	PDF		$\sigma$ (pb)
$\mu^2 = p_T^2 + Q^2 + 4m_c^2$	Pet.	0.25	5	1.5	GRV LO		<b>123</b>
	Lund	0.25	5	1.5	GRV LO		122
	Pet.	0.239	4	1.5	GRV LO		104
	Pet.	0.25	5	1.35	GRV LO		130
	Pet.	0.25	5	1.6	GRV LO		119
	Pet.	0.25	5	1.5	GRV HO		77
Soft color interaction model							
Scale	Frag.	$\Lambda_{QCD}$	$N_f$	$m_c$	PDF		$\sigma$ (pb)
$\mu^2 = \hat{s}$	Pet.	0.2	4	1.5	GRV LO		<b>400</b>

**Table 4.4:** Predictions for the cross section  $\sigma(ep \rightarrow e(D^*X)Y)$  of the resolved pomeron, the two-gluon and the soft color interaction model in the kinematic range  $2 < Q^2 < 100 \text{ GeV}^2$ ,  $0.05 < y < 0.7$ ,  $p_T(D^*) > 2 \text{ GeV}$ ,  $|\eta(D^*)| < 1.5$ ,  $x_p < 0.04$ ,  $M_Y < 1.6 \text{ GeV}$  and  $|t| < 1 \text{ GeV}^2$ . The varied QCD parameter (see Section 4.3) is highlighted. The measured cross section is  $184 \pm 42 \pm 46 \text{ pb}$ .

meson ( $\mathbb{R}$ ). Predictions for the 2-gluon model are given for both a leading order (LO) and a higher order (HO) parameterization of the gluon density within the proton.

The prediction of the resolved IP model of 540 pb is a factor of about 3 larger than the data when using fit 2 and a factorization scale  $\mu^2 = p_T^2 + Q^2 + 4m_c^2$ . The cross section decreases by about 7% when changing simultaneously  $\Lambda_{QCD}$  from 0.25 to 0.239 and  $N_f$  from 4 to 5. Decreasing (increasing) the charm mass from 1.5 GeV to 1.35 GeV (1.6 GeV) decreases (increases) the cross section by  $\approx 10\%$ . Fit 3 produces an increase of the predicted cross section of  $\approx 18\%$ . Applying a next-to-leading order (NLO) fit 2 reduces the cross section by  $\approx 16\%$ . A cross section of 60 pb, which is a factor of 3 below the measured one, is calculated assuming a quark dominated pomeron as described by fit 1. However, this parameterization gives a poor description of  $F_2^{D(3)}$  and other diffractive hadronic final state measurements [82]. But the comparison indicates a very strong sensitivity of the prediction to the assumed parton densities in the pomeron. The cross section prediction for fit 2 shows no significant changes when varying  $\mu^2$  to  $4 \cdot \mu^2$  or  $1/4 \cdot \mu^2$ . The discrepancy to the data remains if  $\mu^2$  changes from  $p_T^2 + Q^2 + 4m_c^2$  to  $4m_c^2$ ,  $p_T^2 + 4m_c^2$  and  $\hat{s}$ . A drop of  $\approx 10\%$  of the cross section is observed if no  $\mathbb{R}$ -exchange is allowed.

The prediction of the 2-gluon model is 123 pb and agrees with the data within the errors. The cross section varies in a similar way but seems to be slightly more sensitive to the change of  $\Lambda_{QCD}$  and  $N_f$  than to the change of  $m_c$  in comparison to the resolved IP model. No significant change in the cross section is seen when using the Lund instead of the Peterson fragmentation process for both the 2-gluon and the resolved IP model. Since the cross section in the 2-gluon model is essentially proportional to the squared of the gluon density in the proton a strong dependency on the parameterization is predicted.

The prediction of the SCI model is 400 pb which is a factor of about 2 above the data. In this model the probability for soft color interactions to occur is a free parameter and hence the overall normalization can be steered. For the prediction in Table 4.4 a probability of 0.5 is used which is found to be suitable for the description of  $F_2^{D(3)}$  and diffractive dijet production [86].

The cross sections are shown differentially as a function of (a)  $p_T^*$ , (b)  $x_P$ , (c)  $z_P^{obs}$  and (d)  $Q^2$  in Figure 4.6 and as a function of (a)  $\beta$ , (b)  $y$ , (c)  $\eta$ , (d)  $p_T$  and (e)  $\phi^*$  in Figure 4.7. The data are represented by the points with error bars where the inner corresponds to the statistical and the outer to the total error. The models discussed above are plotted for comparison. The resolved IP model is normalized by a factor of 1/3 and the SCI model by a factor of 1/2. The bin-size for the individual distribution is chosen such that each bin contains approximately the same number of  $D^*$  mesons. The  $\Delta M$  signals in bins of  $p_T^*$ ,  $x_P$  and  $z_P$  are shown in Figure 4.8. The statistics with about  $20 \pm 6$  events in each bin is rather poor which is reflected by the large error bars. The resolved pomeron approach reproduces well the shape of all the spectra and in particular the fact that the data show a sizeable fraction of charm production in the low  $z_P^{obs}$  (high  $M_X$ ) region. Most of the spectra are also well described in shape by the SCI model. However, this model is not appropriate to describe the regions of high masses of system  $X$  for the reasons discussed in Section 1.5.3 and hence it does not reproduce well the shape of the  $z_P^{obs}$ ,  $x_P$  and  $\beta$  distributions.

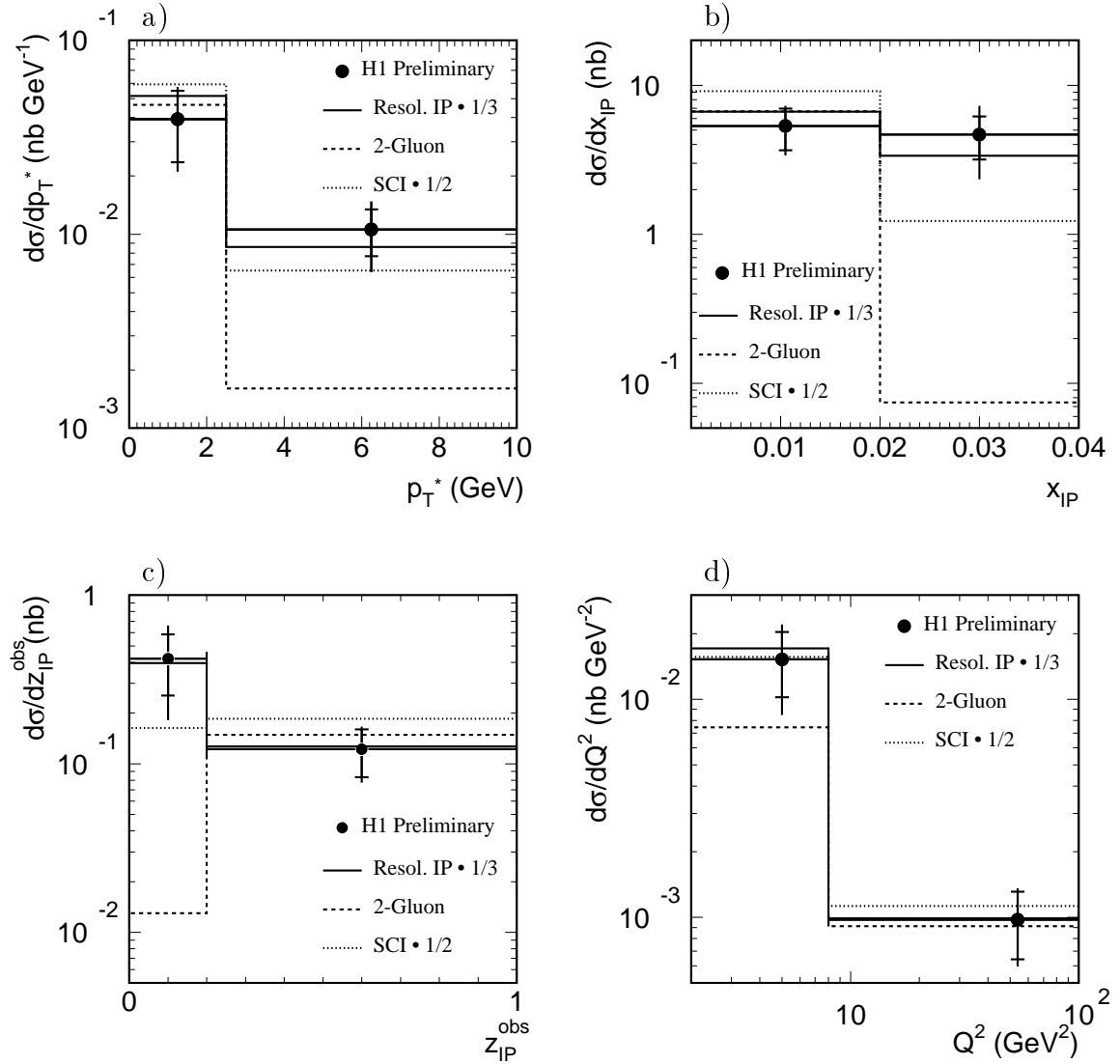


**Figure 4.6:** Differential cross sections  $\sigma(ep \rightarrow e(D^*X)Y)$  as a function of (a)  $p_T^*$ , where  $p_T^*$  denotes the transverse momentum of the  $D^*$  in the  $\gamma^*p$  center of mass system, (b) the fraction  $x_P$  of the proton momentum carried by the pomeron, (c)  $z_P^{\text{obs}}$ , which is an approximation to the momentum fraction of the pomeron carried by the gluon and (d)  $Q^2$ . The data are shown as points with error bars (inner: statistical, outer: total) and are compared to the resolved  $\mathbb{P}$  model (solid line), the 2-gluon model (dashed line) and the SCI model (dotted line). The resolved  $\mathbb{P}$  model is normalized by a factor of  $1/3$  and the SCI model by a factor of  $1/2$ .

The 2-gluon model, in contrast to the resolved  $\mathbb{P}$  model, does not describe the regions of higher mass for the system  $X$  i.e. low  $M_{c\bar{c}}/M_X$ , low  $z_P^{\text{obs}}$ . It is apparent, also from the  $p_T^*$  distribution, that higher order contributions such as  $\gamma^* + p \rightarrow c\bar{c}g + p'$  are needed. The discrepancy at low  $\beta$  reflects the behavior at high  $x_P$ . It is, however, interesting to note that the data in regions where the hadronic system  $X$  predominantly consists of the  $c\bar{c}$  system alone (e.g. high  $z_P^{\text{obs}}$ ) are well reproduced in magnitude.

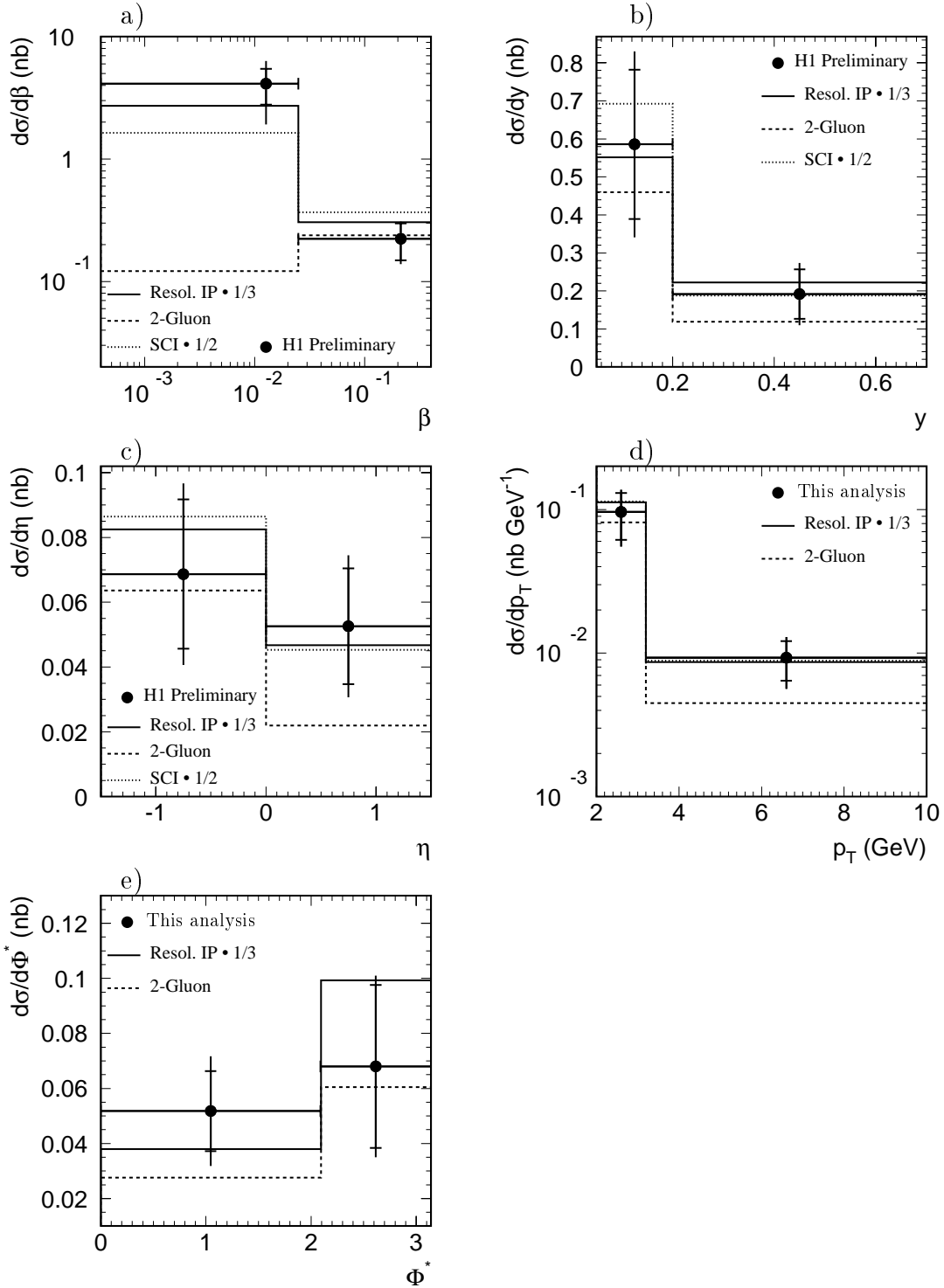


**Figure 4.7:** Differential cross sections  $\sigma(ep \rightarrow e(D^*X)Y)$  as a function of (a)  $\beta = Q^2/(M_X^2 + Q^2)$ , (b)  $y$ , (c)  $\eta$ , (d)  $p_T$  and (e)  $\Phi^*$ , where  $\Phi^*$  is defined as the absolute value of the angle between the positron scattering plane and the  $c\bar{c}$ -plane in the  $\gamma^*IP$  center of mass system. The models used for comparison are described in Figure 4.6. The resolved IP model is normalized by a factor of 1/3 and the SCI model by a factor of 1/2.

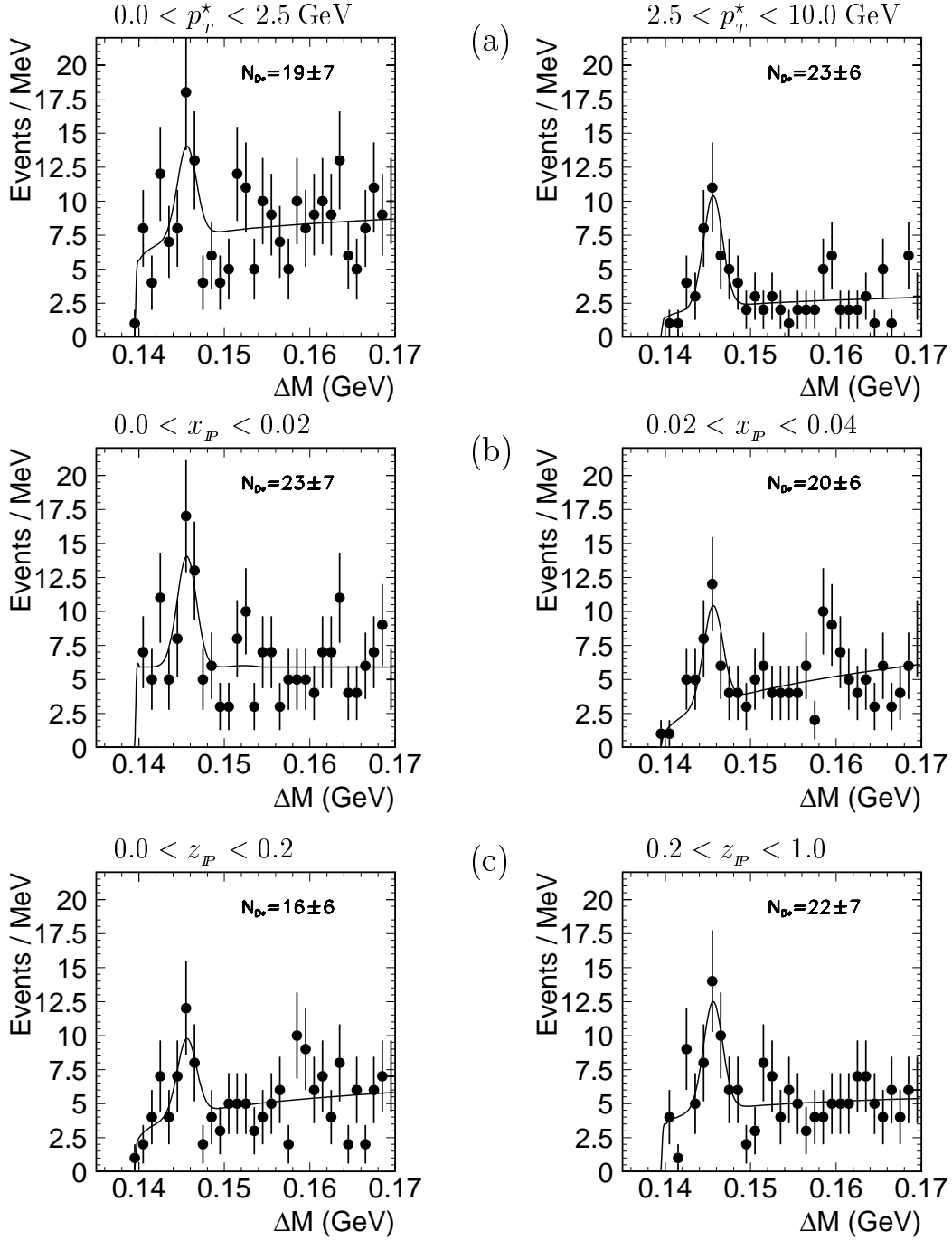


**Figure 4.8:**  $\Delta M$  signals in bins of (a)  $p_T^*$ , (b)  $x_P$  and (c)  $z_P$ . The numbers of  $D^*$  mesons  $N_{D^*}$  and the bin sizes used for the measurement of the differential cross sections  $\sigma(ep \rightarrow e(D^* X)Y)$  are given.

### 4.3.3 Comparison with ZEUS results

The ZEUS collaboration also measures diffractive  $D^*$  production in DIS using 1995-1997 data amounting to an integrated luminosity of  $43.3 \text{ pb}^{-1}$  [84]. The kinematic region is substantially different from the one measured in this analysis, specifically  $3 < Q^2 < 150 \text{ GeV}^2$ ,  $0.02 < y < 0.7$ ,  $p_T(D^*) > 1.5 \text{ GeV}$ ,  $|\eta(D^*)| < 1.5$ ,  $x_p < 0.012$  and  $\beta < 0.8$ . The accessible range of  $x_p$  is restricted to values less than 0.012 since the phase space available for the hadronic final state is reduced by requiring a large rapidity-gap in the event of  $\eta_{max} < 1.5$ . The quantity  $\eta_{max}$  is similarly defined to the one used in this analysis (see Section 3.4.1). In this range ZEUS yield a signal of  $59 \pm 9$  events, extracted through the decay chain  $D^* \rightarrow D^0 \pi_s \rightarrow (K\pi)\pi_s$ . After the subtraction of  $31 \pm 15\%$  proton dissociation background estimated from inclusive diffractive ZEUS results the corresponding diffractive cross section is

$$\sigma(ep \rightarrow e(D^*X)Y) = 379 \pm 66(stat.)_{-140}^{+99}(syst.) \text{ pb} . \quad (4.5)$$

ZEUS corrects the data for detector acceptance using the RAPGAP resolved IP model with a gluon dominated pomeron. This model predicts a cross section of 326 pb which is in agreement with the data. However, the errors are large and within about  $1.3\sigma$  ZEUS is compatible with being a factor of 3 below the RAPGAP prediction. The different kinematic regions measured by ZEUS and H1 and the obtained cross sections  $\sigma(ep \rightarrow e(D^*X)Y)$  are summarized in Table 4.5.

H1	ZEUS
$2 < Q^2 < 100 \text{ GeV}^2$	$3 < Q^2 < 150 \text{ GeV}^2$
$0.05 < y < 0.7$	$0.02 < y < 0.7$
$p_T(D^*) > 2 \text{ GeV}$	$p_T(D^*) > 1.5 \text{ GeV}$
$-1.5 < \eta(D^*) < 1.5$	$-1.5 < \eta(D^*) < 1.5$
$\eta_{max} < 3.3$	$\eta_{max} < 1.5$
$0 < x_p < 0.04$	$0.002 < x_p < 0.012$
$M_Y < 1.6 \text{ GeV} \quad  t  < 1 \text{ GeV}^2$	$M_Y = m_p$
$0 < \beta < 1.0$	$0 < \beta < 0.8$
Results	
$N_{D^*} = 41 \pm 9 \quad (\mathcal{L} = 21.72 \text{ pb}^{-1})$	$N_{D^*} = 59 \pm 9 \quad (\mathcal{L} = 43.3 \text{ pb}^{-1})$
$184 \pm 42(stat.) \pm 46(syst.) \text{ pb}$	$379 \pm 66(stat.)_{-140}^{+99}(syst.) \text{ pb}$

**Table 4.5:** Kinematic regions measured by H1 and ZEUS.

ZEUS also presents results from their combined 1996-1997 data sample ( $37.0 \text{ pb}^{-1}$ ) using the  $D^{*+} \rightarrow (D^0 \rightarrow K^- \pi^+ \pi^- \pi^+) \pi_s^+ (+c.c.)$  decay channel [85]. This analysis is performed in a kinematic range different to the one used in the  $D^* \rightarrow D^0 \pi_s \rightarrow (K\pi)\pi_s$  analysis. The cross section is interpolated to the  $D^* \rightarrow D^0 \pi_s \rightarrow (K\pi)\pi_s$  kinematic region using

the RAPGAP Monte Carlo and is found to be in good agreement with the result quoted in Equation 4.5.

In order to make a more direct comparison, which does not rely on a particular model needed to relate measurements, performed in different kinematic regions, to each other, a study is made where ZEUS cuts are applied to H1 data. Figure 4.9 shows the  $\Delta M$  distribution when adapting the ZEUS cuts in terms of  $Q^2$ ,  $p_T(D^*)$  and  $x_{\mathbb{P}}$ , as given in Table 4.5. The remaining signal corresponds to  $14 \pm 6$   $D^*$  mesons. The final combined acceptance and efficiency correction decreases from about 40% (see Section 4.1.4) to approximately 10%, which is in agreement with the efficiency quoted by ZEUS. A cross section  $\sigma = 166 \pm 74(stat.)$  pb is obtained, which still disagrees by a factor of almost 2 from the prediction of the resolved IP model of 314 pb, but the discrepancy is only of the order of  $2\sigma$  of the statistical uncertainty alone.

Both the ZEUS and H1 collaborations measure  $D^*$  mesons in diffractive processes. The H1 measurement is below the expectation of the resolved IP model, which is not confirmed by the ZEUS data. The present experimental precision does not allow to solve the discrepancy.

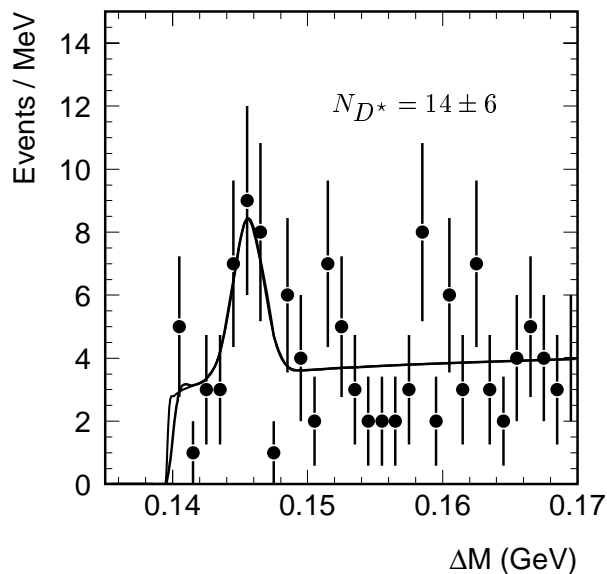


**Figure 4.9:** Diffractive  $D^*$  signal after applying the ZEUS kinematic cuts  $3 < Q^2 < 150$   $GeV^2$ ,  $0.02 < y < 0.7$ ,  $p_T(D^*) > 1.5$   $GeV$ ,  $|\eta(D^*)| < 1.5$ ,  $x_{\mathbb{P}} < 0.012$  and  $\beta < 0.8$ .

#### 4.3.4 Results from diffractive dijet production

The partonic structure of diffractive interactions can also be tested by the analysis of dijet production in DIS. High transverse momentum jets introduce an additional hard scale  $\mu^2$  and are directly sensitive to the gluon content of the diffractive exchange since the leading order production mechanism is photo-gluon fusion, see Figure 4.10(a). In the most recent analysis of 1996-1997 H1 data [87], diffractive dijets are selected in the

kinematic range  $4 < Q^2 < 80 \text{ GeV}^2$ ,  $0.1 < y < 0.7$ ,  $x_p < 0.05$ ,  $M_Y < 1.6 \text{ GeV}$  and  $|t| < 1 \text{ GeV}^2$ . (The kinematic range for the diffractive  $D^*$  analysis presented in this thesis is  $2 < Q^2 < 100 \text{ GeV}^2$ ,  $0.05 < y < 0.7$ ,  $x_p < 0.04$ ,  $M_Y < 1.6 \text{ GeV}$  and  $|t| < 1 \text{ GeV}^2$ ). The jets are defined by the cone algorithm [88]. The transverse momentum of the jets  $p_{T,jets}^*$  is measured in the  $\gamma^*p$  center of mass system and is required to be greater than  $4 \text{ GeV}$ . The observable  $z_P^{jets}$  approximately measures the energy fraction of the hadronic final state of the system  $X$  which is contained in the two jets, defined as

$$z_P^{jets} = \frac{M_{12}^2 + Q^2}{M_X^2 + Q^2}, \quad (4.6)$$

where  $M_{12}$  denotes the invariant dijet mass calculated from the massless jet four-vector. Figure 4.10(b) shows the diffractive dijet cross section as a function of  $z_P^{jets}$ . The resolved IP model with a gluon density according to fit 2 is in perfect agreement with the measurement. The fit 3 parameterization overestimates the data at high values of  $z_P^{jets}$ , however it describes the cross section in the overall normalization.

In conclusion, diffractive dijet data support the resolved IP model with a gluon dominated partonic structure of the pomeron.

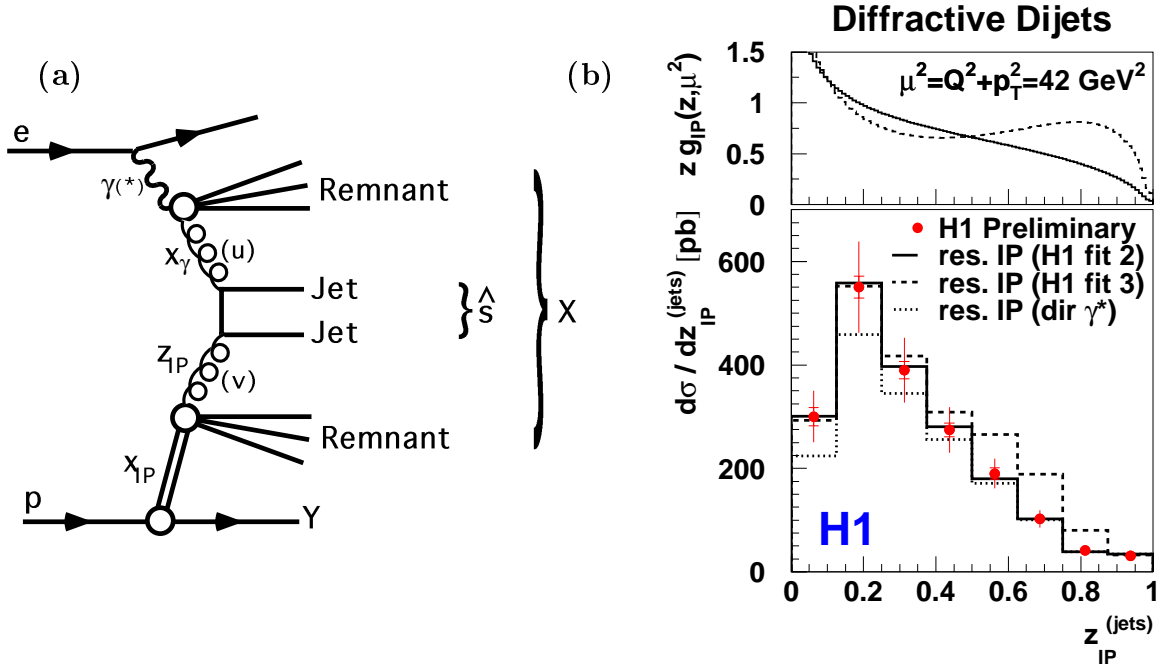


**Figure 4.10:** (a) Kinematics of diffractive dijet production at HERA. (b) Diffractive dijet cross section as a function of  $z_P^{jets}$  [87]. The data are compared to the resolved IP model with gluon densities (H1 fit 2 and 3) as extracted from QCD fits to  $F_2^{D(3)}$  evolved to a scale  $\mu^2 = p_T^2 + Q^2 = 42 \text{ GeV}^2$ , corresponding to the mean value of the event sample. The predictions are shown for the sum of direct and resolved photon contributions. The size of the direct photon contribution alone is indicated by the dotted line.

# Chapter 5

## Summary and Outlook

In this thesis an analysis is presented of open charm production in diffractive deep inelastic scattering (DIS). The data have been collected with the H1 detector at the  $ep$  collider HERA during the years 1995, 1996 and 1997 and correspond to an integrated luminosity of about  $22 \text{ pb}^{-1}$ . The analysis is restricted to events in which the scattered positron is detected and identified in the backward calorimeter SPACAL allowing for a precise reconstruction of the DIS kinematics. Diffractive events are selected utilizing their typical experimental signature of a rapidity gap dividing the hadronic final state into two distinct systems  $X$  and  $Y$ . Open charm events are measured via the reconstruction of  $D^*$  mesons through the decay chain  $D^{*\pm} \rightarrow D^0 \pi_s^\pm \rightarrow (K^\mp \pi^\pm) \pi_s^\pm$ .

The diffractive cross section for  $D^*$  meson production  $\sigma(ep \rightarrow e(D^*X)Y)$  is measured. In the probed kinematic range about 4.5% of the open charm events are produced diffractively. This is a factor of about 3 below the expectation based on the resolved pomeron model, where the parton distributions derived from a QCD analysis of the inclusive diffractive structure function  $F_2^{D(3)}$  are dominated by gluons at the starting scale. The predictions of the resolved pomeron model show a strong sensitivity to the assumed parton density in the pomeron.

Differential cross sections are presented as a function of various kinematic variables to shed further light on the dynamics of diffractive charm production, showing striking differences depending on the underlying model. This holds in particular for the variable  $z_P$  which directly probes the gluons taking part in the interaction. All differential distributions are found to be well described in shape by the resolved pomeron model. The model fits the data in regions of high masses  $M_X$  of the hadronic system  $X$ , low values of the hadronic observable  $z_P^{obs}$ , where a sizeable fraction of charm is produced. In the resolved pomeron picture  $z_P^{obs} \approx M_{c\bar{c}}/M_X$  is an approximation to the momentum fraction of the pomeron carried by the interacting gluon.

The data are compared with the predictions of two alternative models for diffractive open charm production.

The Soft Color Interaction (SCI) model as implemented in the Monte Carlo generator AROMA 2.2, which describes rapidity gap events without the introduction of a pomeron.

The  $c\bar{c}$  pair is produced via photon-gluon fusion and is transformed with a certain probability into a color singlet state by soft color interactions between the partons of the hard sub-process. Gluon radiation from the  $c\bar{c}$  pair is suppressed by the large charm mass and hence the mass  $M_X$  of the system  $X$  is relatively small.

The two-gluon model as implemented in the Monte Carlo generator RAPGAP is a calculation of the process  $\gamma^* + p \rightarrow c\bar{c} + p'$  where two perturbative gluons are exchanged between the proton and the  $c\bar{c}$  pair. The mass  $M_X$  is restricted to the invariant mass  $M_{c\bar{c}}$  of the  $c\bar{c}$  pair.

The SCI model suffers from a similar normalization problem as the resolved pomeron model. The ratio of diffractive to inclusive charm production in this model is predicted to be about 10%. This could be compensated by altering the probability of soft color interactions to occur, which is a free parameter in the model. The shape of the cross sections as a function of  $z_P^{obs}$  and  $x_P$  are not well described.

The two-gluon model predicts an overall cross section which is in agreement with the data. However, this model does not reproduce well the shape of the differential spectra. This holds in particular for the regions of higher mass for the system  $X$ . It is apparent that higher order contributions such as  $\gamma^* + p \rightarrow c\bar{c}g + p'$  are needed.

Diffractive charm production turned out as an ideal testing ground to probe the nature of diffractive interactions. None of the discussed models describes the dynamics of diffractive charm in all aspects, thus they are clearly in need of refinement.

The most obvious improvement to the analysis presented here would be a significant increase of the integrated luminosity. A total amount of luminosity of the order of  $100\text{pb}^{-1}$  has already become available and will substantially be increased after the luminosity upgrade, allowing future analyses a much more precise insight into the structure of the pomeron.

# Appendix A

## Reflection Background

Contributions to an invariant mass difference distribution from decay modes other than the one used for the cross section measurement are referred to as *reflections* (see Section 4.1.2). If they contribute to the signal, they constitute a background which must be corrected for. In a previous measurement of the diffractive  $D^*$  cross section using 1994 data [89] the reflection background was estimated from Monte Carlo (MC) events containing  $D^{*\pm}$  mesons decaying via channels other than the analyzed one  $D^{*\pm} \rightarrow D^0 \pi_s^\pm \rightarrow (K^\mp \pi^\pm) \pi_s^\pm$ . The simulated events were passed through the detector simulation and the size of the resulting  $\Delta M$  signal gives an estimate of the fraction of the data signal that is due to reflections. In the 1994 analysis the reflection background was quoted to be  $(20 \pm 19)\%$ , where the error is dominated by the limited Monte Carlo statistics. This large uncertainty could in principle be reduced by simply increasing the MC statistics. It will be shown below that only a few  $D^*$  decay channels with small branching ratios contribute to the reflection background. Large MC files, consuming much computing power during their generation and simulation, are required to reach an acceptable level of precision. A more practical method to determine the reflection background is introduced in the following.

### A.1.1 Reconstruction of $D^*$ decays on generator level

$D^*$  events are generated with the AROMA MC program. The generator is steered such that the  $D^*$  and the  $D^0$  meson is forced to decay through a certain decay mode which possibly contribute to the reflection background. The selected decays have a multiplicity not greater than four and consist of two oppositely charged particles (see Table A.1). On the basis of these MC files the kinematics of the decay products are studied at generator level. The particle momenta for each event stored in generator banks are treated like the measured tracks and the invariant mass  $M(K, \pi)$  and the mass difference  $\Delta M = M(K, \pi, \pi_s) - M(K, \pi)$  is computed for all particle combinations analog to the  $D^*$  reconstruction technique which is explained in Section 3.3. The generated particles have to satisfy the same cuts as the data tracks, namely  $20^\circ < \theta < 160^\circ$ ,  $p_T(K, \pi) > 250 \text{ MeV}$ , and  $p_T(\pi_s) > 140 \text{ MeV}$ . The transverse momentum and the pseudorapidity of the  $D^*$  meson

$D^*$ decay mode	BR (%)	$D^0$ decay mode	BR (%)
$D^*(2010)^+ \rightarrow D^0 \pi_s^+$	$(68.3 \pm 1.4)$	$D^0 \rightarrow K^- \pi^+$	$(3.85 \pm 0.09)$
		$D^0 \rightarrow K^- K^+$	$(0.43 \pm 0.02)$
		$D^0 \rightarrow \pi^+ \pi^-$	$(0.15 \pm 0.01)$
		$D^0 \rightarrow K^- \pi^+ \pi^0$	$(13.9 \pm 0.9)$
		$D^0 \rightarrow \pi^+ \pi^- \pi^0$	$(1.6 \pm 1.1)$
		Semileptonic modes	
		$D^0 \rightarrow K^- e^+ \nu_e$	$(3.66 \pm 0.18)$
		$D^0 \rightarrow K^- \mu^+ \nu_\mu$	$(3.23 \pm 0.17)$
		$D^0 \rightarrow \bar{K}^*(892)^- e^+ \nu_e$	$(2.02 \pm 0.33)$
$D^*(2007)^0 \rightarrow D^0 \pi^0$	$(61.9 \pm 2.9)$	$D^0 \rightarrow K^- \pi^+$	
$D^*(2007)^0 \rightarrow D^0 \gamma$	$(38.1 \pm 2.9)$	$\pi (\gamma)$ conversion into electrons	

**Table A.1:**  $D^*$  decay modes and branching ratios (BR). The numbers are taken from [68] and should be compared to the branching ratio of the decay channel used for the  $D^*$  cross section measurement, which is highlighted in the first row.

calculated from the three-particle combination is restricted to the range  $p_T(D^*) > 2$  GeV and  $-1.5 < \eta(D^*) < 1.5$ . If the  $\Delta M$  distribution of the considered decay mode indicates an enhancement at or near  $\Delta M = 145.4$  MeV for real  $D^{*\pm} \rightarrow D^0 \pi_s^\pm \rightarrow (K^\mp \pi^\pm) \pi_s^\pm$  decays, the events are fed through the detector simulation to determine their contribution to the reflection background (see Section A.1.2).

Considering decays such as  $D^{*\pm} \rightarrow D^0 \pi_s^\pm$  where the  $D^0$  decays subsequently into two oppositely charged kaons ( $D^0 \rightarrow K^- K^+$ ) a mass hypothesis of a pion instead of a kaon is wrongly assigned to one of the decay products. The invariant mass of the two-body decay is therefore underestimated according to the difference of the rest masses of the kaon and the pion. This is reflected in a shift of the invariant mass distribution  $M(K, \pi)$  towards lower values than the nominal  $D^0$  mass of 1.8646 GeV [68] which can be seen in Figure A.1(a). For the same reason  $D^0 \rightarrow \pi^+ \pi^-$  decays are reconstructed above the nominal  $D^0$  mass if the kaon hypothesis is assigned to one particle. The detector resolution effects can be approximated by a Gaussian smearing of the  $M(K, \pi)$  distribution according to the measured  $D^0$  width of  $\approx 25$  MeV. A significant fraction of events pass the cut on the range  $\pm 80$  MeV around the nominal  $D^0$  mass indicated in Figure A.1(b). This is also visible in Figure A.1(c) where the mass difference  $\Delta M = M(K, \pi, \pi_s) - M(K, \pi)$  is plotted versus  $M(K, \pi)$ <sup>1</sup>. Since the  $D^0$  is produced by  $D^{*\pm} \rightarrow D^0 \pi_s^\pm$  decays the  $\Delta M$  distribution peaks at around 145.4 MeV shown in Figure A.1(d).

As can be seen from Figure A.2 no contribution to the  $\Delta M$  signal is expected from  $D^0 \rightarrow K^- \pi^+ \pi^0$  decays. The three-body decay is just partially reconstructed and the events from the  $\Delta M$  signal region cluster well below the lower cut on the  $M(K, \pi)$  dis-

<sup>1</sup>Events which are far outside the expected signal region of the  $\Delta M$  and the  $M(K, \pi)$  distribution are rejected by a pre-selection.

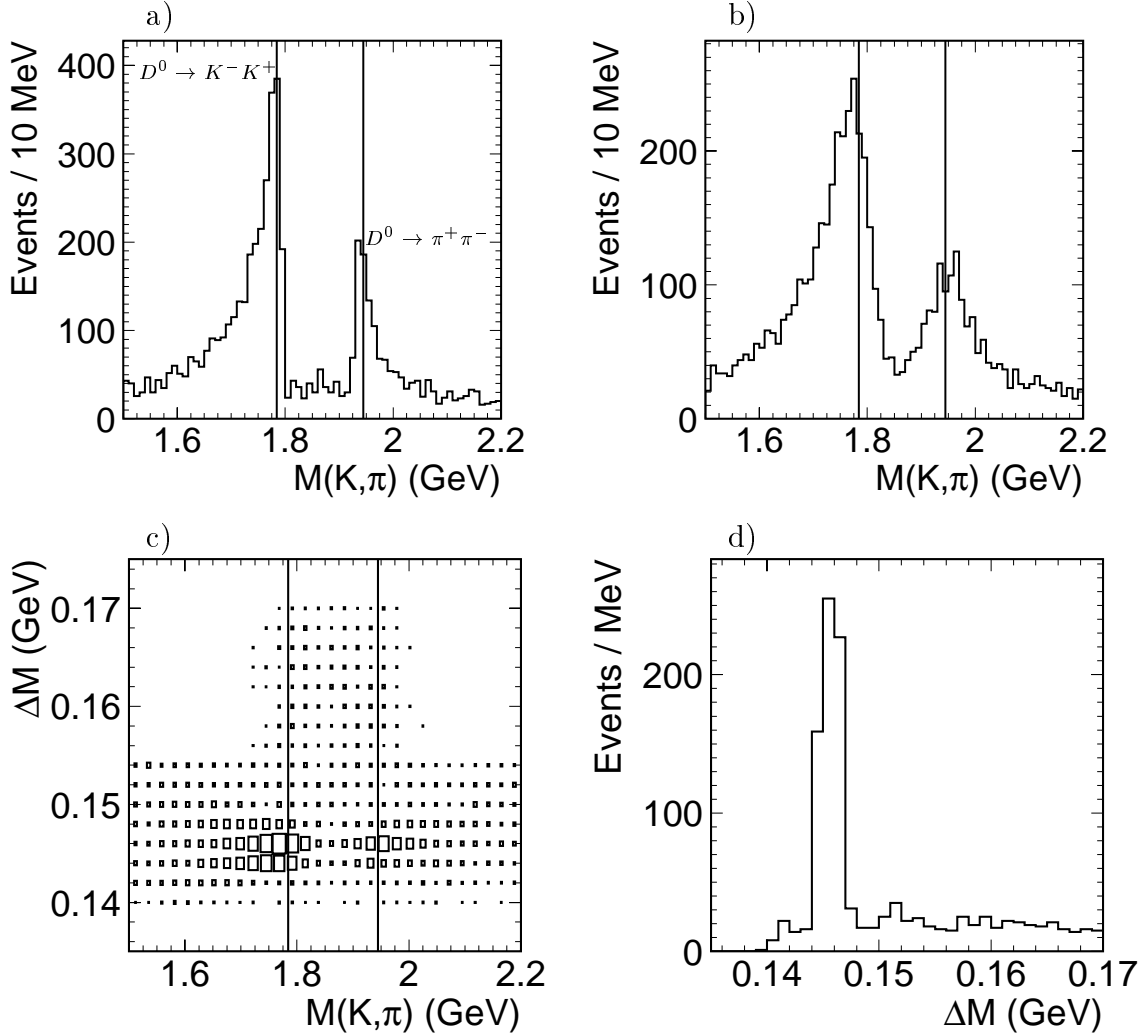


**Figure A.1:** a) Invariant mass  $M(K, \pi)$  for MC events containing  $D^0 \rightarrow K^- K^+$  and  $D^0 \rightarrow \pi^+ \pi^-$  decays and b)  $M(K, \pi)$  smeared with a Gaussian of variance 25 MeV. c) Invariant mass  $\Delta M = M(K, \pi, \pi_s) - M(K, \pi)$  versus  $M(K, \pi)$  and d)  $\Delta M$  distribution (both smeared). The MC event sample corresponds to a luminosity of  $\mathcal{L} \simeq 200 \text{ pb}^{-1}$ .

tribution. In contrast events from  $D^0 \rightarrow \pi^+ \pi^- \pi^0$  decays can migrate into the range  $|M(K, \pi) - M(D^0)| < 80 \text{ MeV}$  because the  $M(K, \pi)$  distribution is shifted to higher values due to the wrong mass assignment to one of the pions, see Figure A.3. The  $\Delta M$  distribution shows a falling combinatorial background and peaks around the  $\Delta M$  signal region. It can be concluded from the investigation of the three-body decays, that events where the  $D^0$  decays into more than three particles, e.g.  $D^0 \rightarrow K^- \pi^+ \pi^+ \pi^-$ , are rejected by the cut on the  $D^0$  mass window.

The distributions shown in Figure A.4 suggest a small contribution to the reflection background from  $D^0 \rightarrow K^- \mu^+ \nu_\mu$  decays. This is not the case for the semileptonic decays  $D^0 \rightarrow K^- e^+ \nu_e$  and  $D^0 \rightarrow \bar{K}^*(892)^- e^+ \nu_e$  for which no enhancement in the  $\Delta M$  distribution is observed.

Finally, events are investigated where the  $D^0$  meson decays into a  $K^-\pi^+$  but is produced through the decay of a  $D^*(2007)^0$  meson. The  $\pi^0$  or the  $\gamma$  produced together with the  $D^0$  can fake a  $\pi_s$  candidate by electron conversion. Such decays are found not to contribute to the  $\Delta M$  signal.

### A.1.2 Determination of the background

Events with  $D^*$  decays contributing to the reflection background as suggested by the above described generator study are passed through the detector simulation. They are mixed with simulated  $D^* \rightarrow D^0\pi_s \rightarrow (K\pi)\pi_s$  events accounting for their branching ratios. The number of  $D^*$  mesons is reconstructed from the  $\Delta M$  fit. Comparing this number to the number of  $D^*$  mesons extracted from the  $\Delta M$  distribution based upon the pure  $D^* \rightarrow D^0\pi_s \rightarrow (K\pi)\pi_s$  event sample a reflection background of  $r = (3.5 \pm 1.5)\%$  is obtained. The main contribution of  $\approx 3\%$  is caused by  $D^0 \rightarrow K^-K^+$  and  $D^0 \rightarrow \pi^+\pi^-$  decays. About 0.5% is attributed to the decays  $D^0 \rightarrow \pi^+\pi^-\pi^0$  and  $D^0 \rightarrow K^-\mu^+\nu_\mu$ . Contributions from other decay modes are sufficiently suppressed by the cut on the  $D^0$  mass window. No significant change of  $r$  is seen when varying the minimum required transverse momentum of the  $D^*$  candidate within the range  $1.5 < p_T(D^*) < 2.5$  GeV. A systematic uncertainty of 1.5% accounts for decay modes which are not considered or do not contribute, within the precision of this study, to the reflection background.

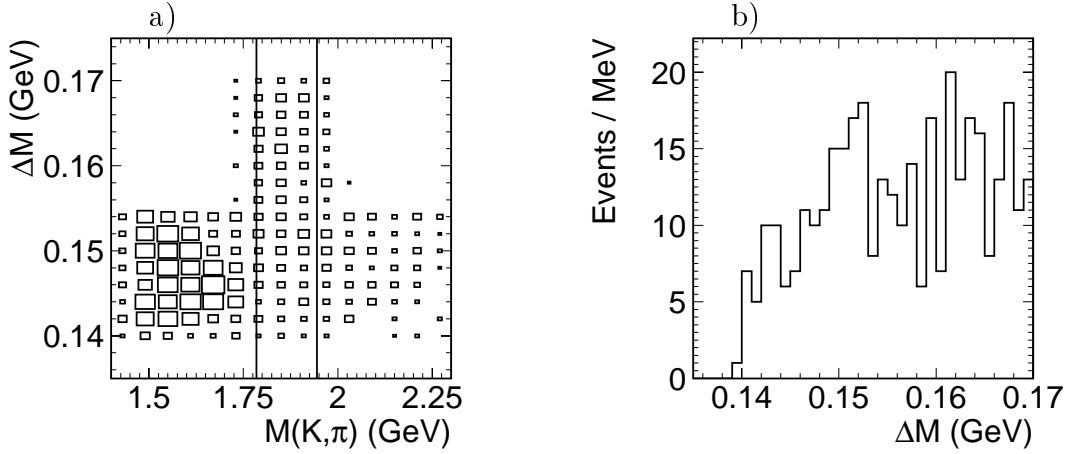


**Figure A.2:** Invariant mass distribution  $\Delta M$  versus  $M(K, \pi)$  (a) and  $\Delta M$  (b) for  $D^0 \rightarrow K^- \pi^+ \pi^0$  decays. The luminosity of the MC event sample is  $\mathcal{L} \simeq 7.5 \text{ pb}^{-1}$ .

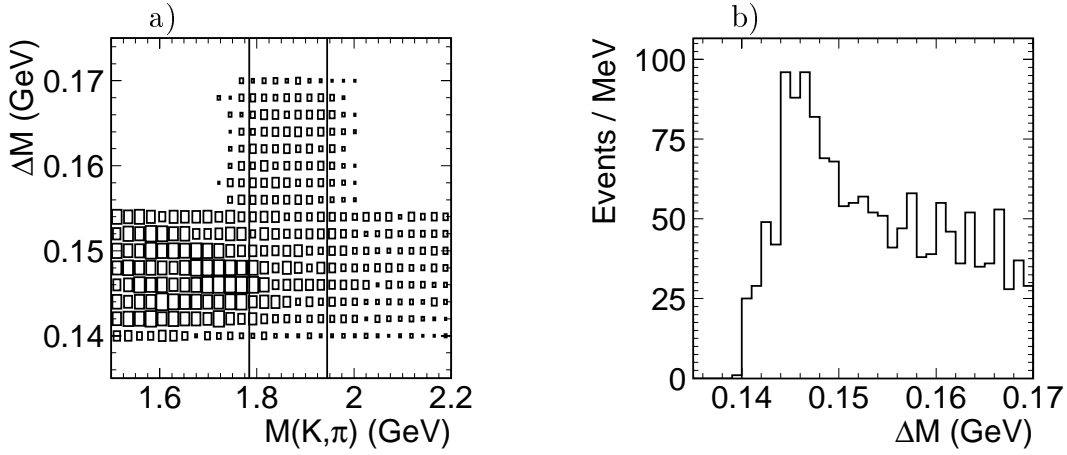


**Figure A.3:** Invariant mass distribution  $\Delta M$  versus  $M(K, \pi)$  (a) and  $\Delta M$  (b) for  $D^0 \rightarrow \pi^+ \pi^- \pi^0$  decays. The luminosity of the MC event sample is  $\mathcal{L} \simeq 80 \text{ pb}^{-1}$ .

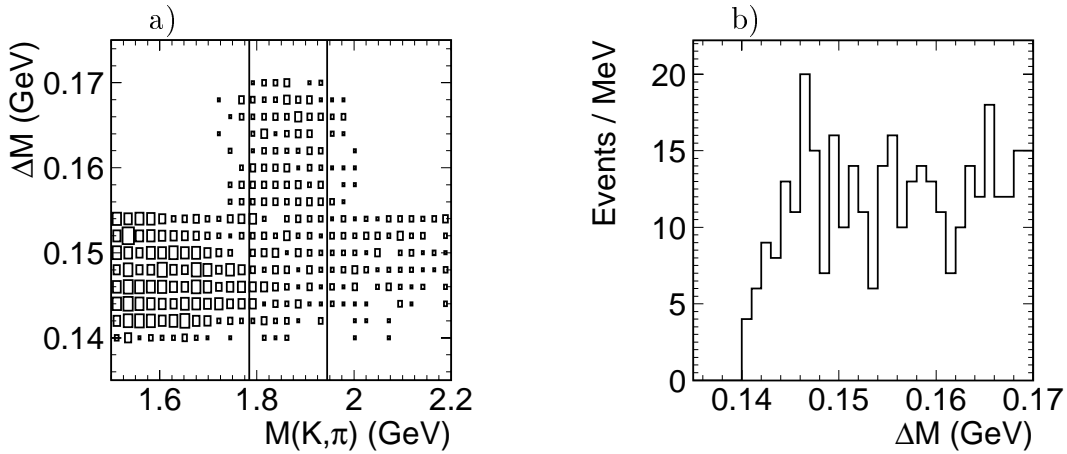


**Figure A.4:** Invariant mass distribution  $\Delta M$  versus  $M(K, \pi)$  (a) and  $\Delta M$  (b) for  $D^0 \rightarrow K^- \mu^+ \nu_\mu$  decays. The luminosity of the MC event sample is  $\mathcal{L} \simeq 35 \text{ pb}^{-1}$ .

# Appendix B

## Reconstruction of Charm Mesons with the CST

The central silicon tracker CST has been integrated into regular data taking in 1997. Some technical details about the design and the performance of the detector have already been outlined in Section 2.2.3. The main purpose of the CST is the precision measurement of secondary vertices produced by the decays of heavy quark hadrons. The track parameters as measured by the central jet chamber (CJC) are improved by the CST. The performance is investigated using a sample of  $D^* \rightarrow D^0 \pi_s \rightarrow (K\pi)\pi_s$  decays reconstructed with the CJC. On the basis of this sample two aspects are studied; the gain in the invariant mass resolution for both the  $M(K, \pi)$  and the  $\Delta M$  distribution and the secondary vertex resolution caused by the decay of the  $D^0$  meson with a mean lifetime of  $\tau_{D^0} = 124.4 \mu\text{m}$  [68].

### B.1 CST tracks

The CST hits are linked to the tracks measured in the CJC by extrapolating the track on the surface of the two CST layers at radii 5.75cm and 9.75cm. The calculated hit *residuals* must lie within a certain tolerance given in units of the track extrapolation error. The hit with the smallest residuum is then assigned to the track. The linking is performed using the CJC track parameters which are fitted to the vertex (see Section 2.2.4). A CST improved set of parameters in the  $r\phi$ -plane  $\vec{T} = (\kappa, dca, \phi)$  is then obtained by minimizing the  $\chi^2$ -function

$$\chi^2 = (\vec{T} - \vec{T}_{CJC})^t V_{CJC}^{-1} (\vec{T} - \vec{T}_{CJC}) + \sum_i \frac{d(T, hit_i)^2}{\sigma_d^2}, \quad (\text{B.1})$$

where  $d(T, hit_i)$  denotes the Euclidean distance between the track circle  $\vec{T}$  and the  $i$ -th CST hit and  $\sigma_d^2$  the corresponding error calculated from the covariance of the hit. In contrast to the hit-track linking, the track fit uses the non-vertex-fitted CJC tracks with parameters  $\vec{T}_{CJC}$  and covariance  $V_{CJC}$  as input to be almost unbiased by the vertex hypothesis. Instead of fitting the CST and CJC hits simultaneously the determination of

the  $r\phi$ -coordinates according to Equation B.1 uses the CST hits alone. This procedure reduces the computing time considerably and can be performed using the data stored on the data summary tapes (DSTs) (Section 2.2.8) which do not contain the CJC hit information.

The polar angle  $\theta$  and the  $z$ -axis intercept  $z_0$  at the  $dca$  are determined from the  $Sz$ -coordinates of the hits measured in the CJC, CIZ, COZ and CST by minimizing

$$\chi^2 = \sum_i \left( \frac{z_i - z_0 - \tau \cdot S_i}{\sigma(z_i)} \right)^2, \quad (\text{B.2})$$

where  $S$  is the arc-length from the  $dca$  point to hit  $i$  in the  $r\phi$ -plane and  $\sigma(z_i)$  is the covariance of the  $z$ -position.  $\theta$  is related to the slope  $\tau$  of the track in the  $Sz$ -plane by  $\tau = \coth \theta$ .

Selection	$N_{D^*}$	Acceptance (%)	Efficiency (%)
Full $D^*$ sample	635	100	-
$K \pi$ in CST	408	64.3	-
$K \pi \pi_s$ in CST	403	63.5	100
$N_{hit}(K) \cdot N_{hit}(\pi) \geq 2$	385	60.9	96.0
$N_{hit}(K, \pi) \geq 2$	221	34.8	54.8
$N_{hit}(K, \pi, \pi_s) \geq 2$	175	27.6	43.4

**Table B.1:** Acceptance and efficiency for tagging  $D^* \rightarrow D^0 \pi_s \rightarrow (K\pi)\pi_s$  decays with the CST.

## B.2 Reconstructing $D^*$ mesons with the CST

The acceptance and efficiency of the CST is studied using an event sample of  $D^*$  mesons reconstructed with the CJC in 1997 data. The angular acceptance of the CST covers a range of  $30^\circ \lesssim \theta \lesssim 150^\circ$  for a particle originating from the nominal interaction point and penetrating both layers with an active length of  $-17.8 < z < 17.8$  cm (compare Table 2.1). As can be seen from Table B.1 the  $D^*$  sample is reduced on average by  $\approx 36\%$  when requiring the reconstructed tracks associated with the  $K$ ,  $\pi$  and the  $\pi_s$  to lie within the geometrical acceptance of the outer CST layer. The efficiency of the silicon detector as determined using cosmic tracks is 97% for the p-side and 92% for the n-side [45]. With an additional inefficiency of  $\approx 5\%$  due to dead regions a single hit efficiency of  $\approx 85\%$  is obtained. This is consistent with an event loss of nearly 50% when demanding at least two hits for both the  $K$  and the  $\pi$ . A much better efficiency of about 96% is achieved when requiring at least two linked hits for only one of the two tracks while the other one is allowed to have just one,  $N_{hit}(K) \cdot N_{hit}(\pi) \geq 2$ . This cut is suitable for a secondary vertex

reconstruction with sufficiently high resolution [92] and is hence used for the following studies of  $D^* \rightarrow D^0 \pi_s \rightarrow (K \pi) \pi_s$  decays using the CST improved track information.

### B.3 Reconstruction of the $D^0$ decay length

The secondary vertex caused by the decay of the  $D^0$  meson is reconstructed using a three-dimensional vertex fitting method as described in [90, 91]. The  $K$  and the  $\pi$  candidates, which are defined by the CST improved track parameters  $\vec{T} = (\kappa, \phi, \theta, dca, z_0)$ , are fitted to the most probable common origin point  $\vec{V}' = (V'_x, V'_y, V'_z)$ . Thereby the weighted distances between the input tracks  $\vec{T}$  and the tracks  $\vec{T}'(\vec{V}', \vec{Q})$ , where  $\vec{Q} = (\kappa', \phi', \theta')$  denotes the parameters fitted to the point  $\vec{V}'$ , are minimized simultaneously. The  $D^0$  decay length in the  $r\phi$ -plane is then given by

$$d_{r\phi} = \sqrt{(V'_x - V_x)^2 + (V'_y - V_y)^2}, \quad (\text{B.3})$$

where  $\vec{V} = (V_x, V_y)$  is the position of the primary vertex (Section 2.2.4). The significance of the decay length is defined as the ratio  $d_{r\phi}/\sigma_{r\phi}$ , where the error  $\sigma_{r\phi}$  on the position of the secondary vertex is taken from the fit and the error on the position of the primary vertex is given by the transverse profile of the interaction region (*beam-spot*) of about  $150 \mu\text{m}$  in  $x$  and  $30 \mu\text{m}$  in  $y$  [45]. The combinatorial background in the  $\Delta M$  distribution due to hadrons decaying at the primary vertex can be reduced by a cut on the significance. This is demonstrated in Figure B.1 where a considerable improvement of the  $\Delta M$  signal-to-noise ratio (*SNR*) is observed when applying a cut  $d_{r\phi}/\sigma_{r\phi} > 1.5$ .

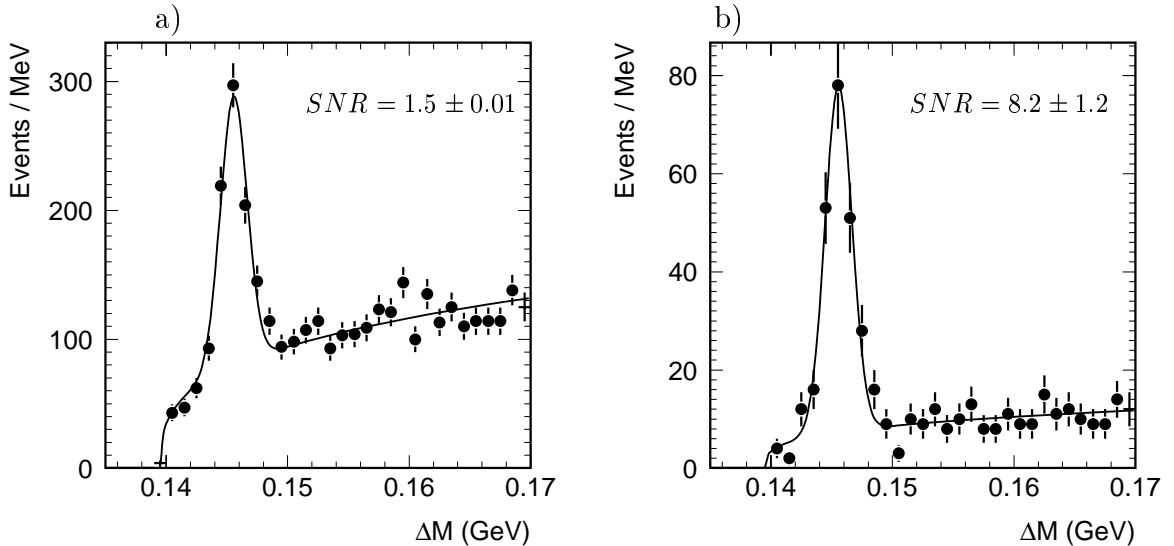


**Figure B.1:**  $\Delta M$  distribution before (a) and (b) after a cut on the significance of the decay length  $d_{r\phi}/\sigma_{r\phi} > 1.5$ . The signal to noise ratio *SNR* as extracted from the  $\Delta M$  fit is quoted.

### B.3.1 Mass resolution of the $D^*$ and the $D^0$ meson

The  $\Delta M = M(K, \pi, \pi_s) - M(K, \pi)$  mass difference distributions shown in Figure B.1 are reconstructed using the track parameters as measured with the CJC. The invariant masses  $M(K, \pi, \pi_s)$  and  $M(K, \pi)$  are re-calculated using the CST improved track parameters. In spite of the improved single track resolution no significant gain in the  $\Delta M$  resolution is observed. A detailed study of  $\Delta M$  distributions reconstructed using partially the CJC and the CST track information reveals that this is mainly due to wrongly linked hits on the n-side<sup>1</sup>, which spoil the precision of the  $z$ -coordinate and  $\theta$ -coordinate respectively. Taking  $\kappa$  and  $\phi$  from the CST and  $\theta$  from the CJC the width of the  $\Delta M$  signal decreases by about 15%. This improvement is mainly due to the improved resolution of the  $\pi_s$  candidate which is much more affected by multiple scattering than the *faster*  $K$  and  $\pi$  candidates. The width of the  $M(K, \pi)$  distribution, plotted for the range  $\pm 1.5$  MeV around the nominal  $\Delta M$  mass of 145.4 MeV, is reduced by  $\approx 6\%$ . Again only  $\kappa$  and  $\phi$  are taken from the CST. A more obvious improvement of the  $D^0$  resolution of about 15% is achieved when at least two CST hits are linked to both the  $K$  and the  $\pi$  track (see Section B.2). The fit to the  $D^0$  signal yield a width of  $24.2 \pm 2.1$  MeV.

## B.4 $D^0$ lifetime

The lifetime  $\tau$  in the rest frame of the  $D^0$  meson can be related to its decay length in the  $r\phi$ -plane by

$$\tau = \frac{m(D^0)}{p_T(D^0)} \cdot d_{r\phi} \cdot \cos \vartheta, \quad (\text{B.4})$$

where  $\vartheta$  denotes the angle between the flight direction ( $\vec{V} - \vec{V}'$ ) measured by the vertex fit and the momentum  $\vec{p}_T(D^0)$  of the  $D^0$  meson in the plane transverse to the beam, see Figure B.2. The projection  $d_{r\phi} \cdot \cos \vartheta$  provides a more accurate estimate for the true  $D^0$  flight distance. Figure B.3 shows the number of  $D^0$  mesons as extracted from a fit to the  $\Delta M$  distribution as a function of the lifetime expressed in units of the  $D^0$  mean lifetime. The data are fitted to a convolution of a Gaussian and an exponential function according to the decay law. The resolution given by the Gaussian width of the distribution is of the same order as the measured lifetime of  $\tau = (145 \pm 21) \mu\text{m}$ , where the quoted error is the statistical. This result is within the error in agreement with the mean lifetime of  $\tau_{D^0} = 124.4 \mu\text{m}$  [68].

The  $D^0$  lifetime distribution may also be used to select beauty decays.  $D^*$  mesons produced via the decay of beauty mesons such as  $B \rightarrow D^* X$  would be measured at large values of the reconstructed lifetime. The study of charm mesons with the CST thus provides a new opportunity to measure beauty production at HERA.

---

<sup>1</sup>The linking on the n-side is much less reliable than on the p-side mainly caused by a significantly lower signal to noise ratio [46]

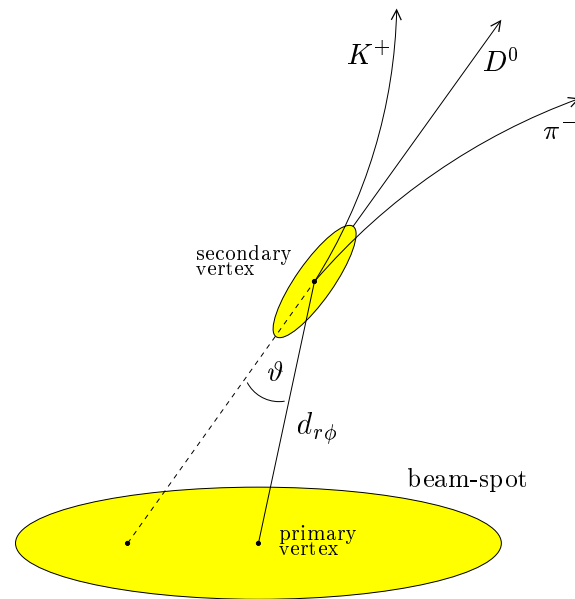


**Figure B.2:**  $D^0$  decay in the  $r\phi$ -plane. The lifetime  $\tau$  is defined as the projection of the decay length  $d_{r\phi}$  on the  $D^0$  momentum according to Equation B.4.

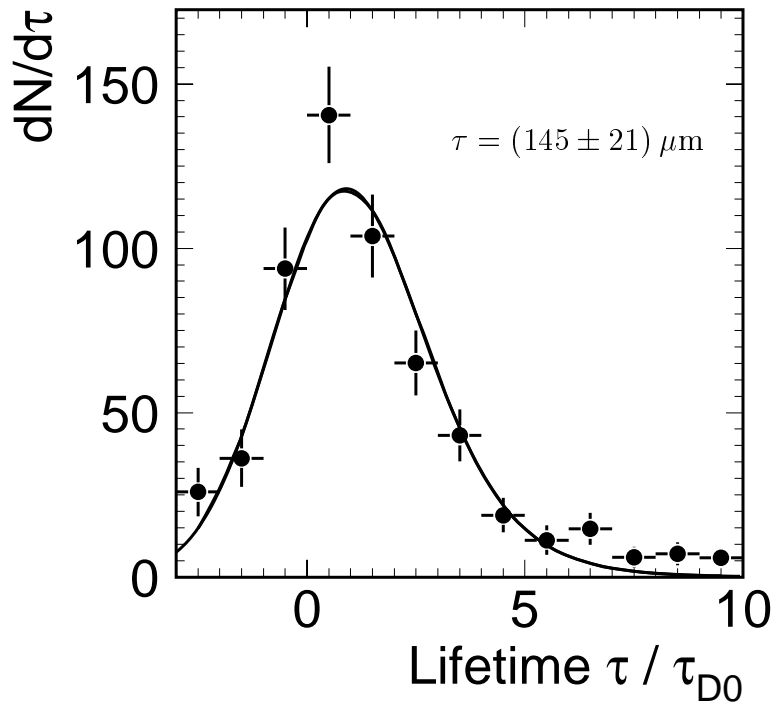


**Figure B.3:** Lifetime distribution of  $D^0$  mesons in units of the  $D^0$  mean lifetime. The curve corresponds to a convolution of a Gaussian and an exponential function describing the decay.

# Appendix C

## Calibration of the Z-Chambers

The central inner and outer  $z$ -chambers CIZ and COZ have been briefly introduced in Section 2.2.3. With wires strung perpendicular around the beam axis the chambers allow a much better measurement of the track position in the  $z$ -coordinate than achieved by charge division of the CJC signals. After a short outline of the space point hit reconstruction the calibration of the  $z$ -chambers, with emphasis on the use of the central silicon detector (CST), is discussed. A new method for a simultaneous offline calibration and alignment of the CIZ and COZ within the framework of the so called *superfit* ansatz is introduced.

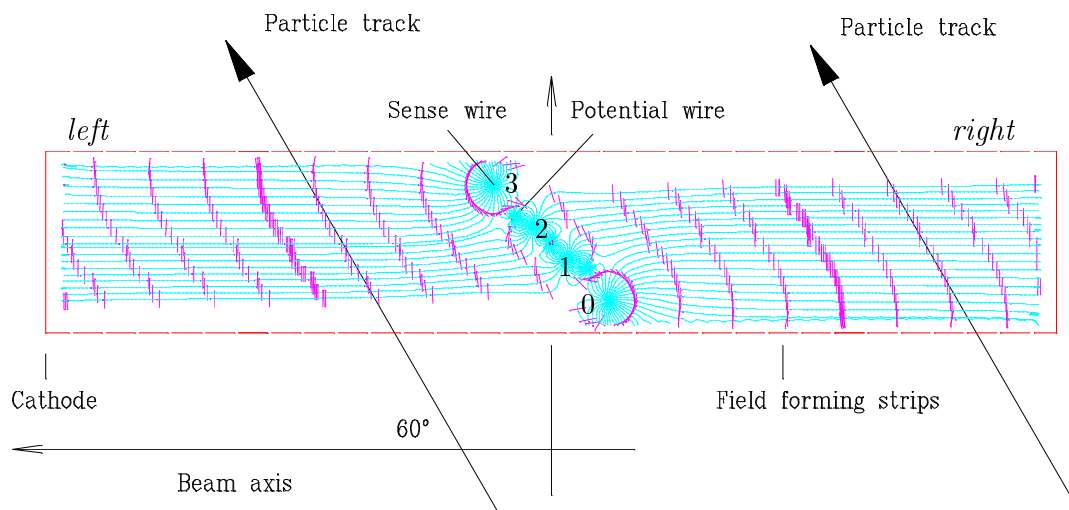


**Figure C.1:** CIZ drift cell cross section. The isochrones are not perpendicular but tilted to the beam axis by about  $60^\circ$ .

### C.1 Space point reconstruction

The basic quantities measured by the  $z$ -chambers are the drift time and the charge of a hit as obtained from the analysis of the pulse-charge integral and the signal timing (*Qt analysis*). Using this information the spatial position of a hit within a drift cell can be

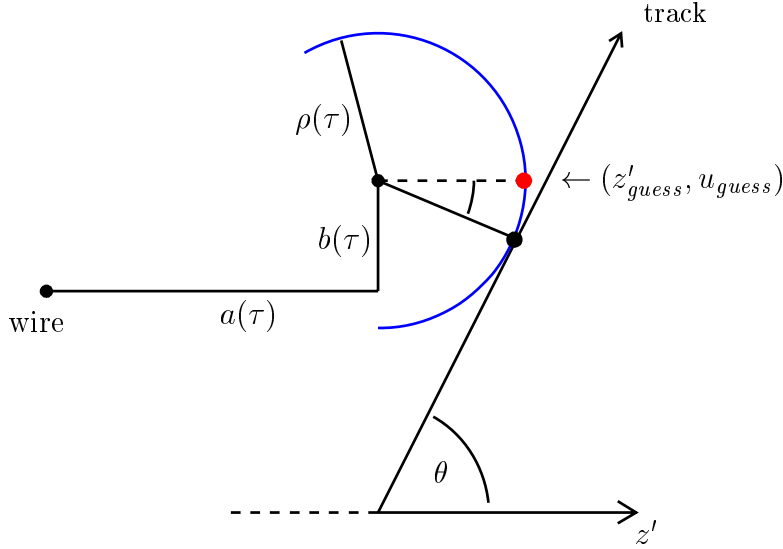


**Figure C.2:** Isochrone correction for CIZ.

reconstructed. Before this is described some technical details about the layout of the CIZ drift cell are explained.

Figure C.1 shows a cross section of a CIZ drift cell. The sense and potential wire planes are tilted with respect to the beam axis by  $45^\circ$ . This leads to a tilt of the drift field isochrones of about  $30^\circ$  which is in contrast to the COZ where the sense wire plane is normal to the beam axis. The field lines are distorted such that a track penetrating the cell leaves signals on only three of the four sense wires. Tracks crossing on the *right* side produce signals on the wires 0,1 and 2, and those crossing on the *left* side give signals on the wires 1,2 and 3. The orientation of the wire plane as shown in Figure C.1 corresponds to the ring numbers 9-14 of the positive  $z$ -region. The tilt changes to the opposite direction for the negative  $z$ -region (rings 0-8). *Cell coordinates*  $(z', u)$  are defined with the  $z'$ -axis parallel to the beam axis and the  $u$ -axis normal to the wire and the beam axis and the origin at the center of the drift cell. Geometrical parameters of the CIZ and the COZ relevant for the calibration are summarized in Table C.1

The reconstruction of the hit space point position  $(z', r)$  depends crucially on the correct description of the isochrones in the drift cells which are parameterized for the CIZ<sup>1</sup> by circular arcs of the form

$$(z' - a(\tau))^2 + (u - b(\tau))^2 = \rho(\tau)^2, \quad (\text{C.1})$$

where  $z'$  and  $x$  are the cell coordinates and  $a$ ,  $b$  and  $\rho$  are functions of the drift time  $\tau$  and the wire number. In Equation C.1  $\tau$  is corrected for time shifts  $t_0$  as

$$\tau = \beta_v \cdot v_d \cdot (t - t_0), \quad (\text{C.2})$$

where  $\beta_v$  is a correction factor accounting for relative changes in the drift velocity  $v_d$ . Before correcting for the polygon shape of the chamber, the radial distance of the hit to the beam axis is given by  $r = r_0 + u$ , where  $r_0$  denotes the radius of the cell center

<sup>1</sup>The COZ isochrones are parameterized by ellipses

(Table C.1). For a measured drift time the isochrone parameters are computed by interpolation using *look up tables* containing simulated values of  $a$ ,  $b$  and  $\rho$  in time steps of 100 ns [93]. Thereby  $z'$  and  $u$  are free to vary between minimal and maximal values determined by the cell geometry. A first guess for the  $(z', r)$  position is given by

$$z'_{guess} = a(\tau) + \rho(\tau) \quad \text{and} \quad r_{guess} = r_0 + u_{guess} = r_0 + b(\tau) \quad (\text{C.3})$$

corresponding to hits produced by tracks with crossing angles of  $\theta = 90^\circ$ . The values for  $z', r$  are corrected as

$$z' = a(\tau) + \rho(\tau) \sin \theta \quad (\text{C.4})$$

$$r = r_0 + b(\tau) - \rho(\tau) \cos \theta \quad (\text{C.5})$$

using the polar angle  $\theta$  of the track. After the isochrone correction has been performed the radial coordinate  $r$  is corrected according to the polygone shape of the wires. The radial distance  $r'$  to an arbitrary point on a polygone edge with the azimuthal coordinate  $\phi$  is given by  $r' = r_c / \cos(|\phi - \phi_c|)$ , where  $r_c$  denotes the radius and  $\phi_c$  the azimuthal angle at its center. The  $\phi$ -coordinate of the hit that is used for the polygone correction can be calculated iteratively. A first value  $\phi_1$  is calculated for the intercept of the track with the radius at the cell center. Using  $\phi_1$  and the radius of the center of the wire where the hit has been measured a polygone correction is performed. For the obtained point on the wire a new angle  $\phi_2$  is calculated which is then used for the polygone correction of the hit coordinate  $r$  as given by Equation C.5. Another value  $\phi_3$  is calculated for the intercept of the track with  $r$  defining the final  $\phi$ -coordinate of the hit.

From the above explained space point reconstruction it should be noted that the determination of the  $z'$  and  $r$  coordinate require the knowledge of the track parameters in both the  $r\phi$  and  $Sz$ -projection. Therefore they can only be determined during the track reconstruction procedure. When they are compared to special reference tracks used for the alignment and calibration, they need to be re-determined, where different values from those found in the standard track reconstruction may be obtained.

## C.2 CST reference tracks

The CST track parameters can be determined from the hits in both projections and in both layers of the CST with the curvature taken from the CJC. These tracks, often referred to as *CST radical tracks*, provide a largely unbiased reference and can be used for comparison with the tracks measured in the CJC and the  $z$ -chambers alone. For cosmic events so called *CST 4-hit cosmic tracks* are defined which provide the most precise reference tracks of the central tracking system. These are cosmic tracks leaving at least one hit in each layer of the upper and lower half of the CST. An efficient outlier rejection of wrongly linked CST hits is applied by comparing the upper and lower half of the CST radical track. This is necessary since the  $z$ -coordinate is measured with the n-side of the CST having a signal-to-noise ratio of a factor of  $\approx 3$  worse than the p-side [45]. For  $ep$  events the outlier rejection can be done by exploiting the vertex constraint.

A special track selection has been developed for the calibration purposes outlined here.

		CIZ	COZ
Active length in $z$	(cm)	$-108.0 < z < 72.0$	$-110.5 < z < 105.5$
Acceptance in $\theta$	( $^\circ$ )	$13.6 \lesssim \theta \lesssim 170.8$	$23.6 \lesssim \theta \lesssim 157.3$
Number of rings		15	24
Drift cells per ring		16	24
Drift cell length	(cm)	12.0	9.0
Drift cell height	(cm)	2.0	2.4
Sense wires per ring		4	4
Tilt of sense wire plane	( $^\circ$ )	45	0
Radius at cell center	(cm)	18.81	47.25
Sense wire position ( $z', u$ ) with respect to cell center	Wire 0 (mm)	$z' = 7.0 \quad u = -7.0$	$z' = 0.0 \quad u = -9.0$
	Wire 1 (mm)	$z' = 2.0 \quad u = -2.0$	$z' = 0.0 \quad u = -3.0$
	Wire 2 (mm)	$z' = -2.0 \quad u = -2.0$	$z' = 0.0 \quad u = 3.0$
	Wire 3 (mm)	$z' = -7.0 \quad u = 7.0$	$z' = 0.0 \quad u = 9.0$

**Table C.1:** Geometrical parameters of CIZ and COZ.

### Z-chamber performance

The improvement of  $\theta$  and  $z_0$  achieved when linking the  $z$ -chamber hits can be studied by comparing the CST radical tracks with the tracks measured in the CJC and the  $z$ -chambers alone. The difference in the parameters  $\Delta\theta = \theta - \theta_{CST}$  is plotted in Figure C.3(a) for tracks with no linked  $z$ -chamber hits and in Figure C.3(b) for those having at least two linked hits in each the CIZ and COZ. The distribution is based upon data collected in the first part of the 1999 running period. Only tracks satisfying quality criteria and having a transverse momentum of  $p_T > 1$  GeV are considered. The precision of the  $\theta$  measurement benefits considerably from the  $z$ -chamber information.

## C.3 Calibration constants and their determination

The determination of the hit space points depends on several calibration constants and parameters. The drift velocity depends e.g. on the electric field and the gas mixture and may therefore change quite frequently with changing running conditions. Furthermore the read-out and signal electronics influence the drift time measurement. Mechanical stress as well as electrostatic and gravitational forces may change the wire position, which can be accounted for by geometrical alignment parameters. In the following the calibration methods for the  $z$ -chambers, which are used so far, will be explained with emphasis on the procedure used for the CIZ. Thereafter an ansatz for a simultaneous re-calibration of the CIZ and COZ on the basis of the precise CST track information is introduced.

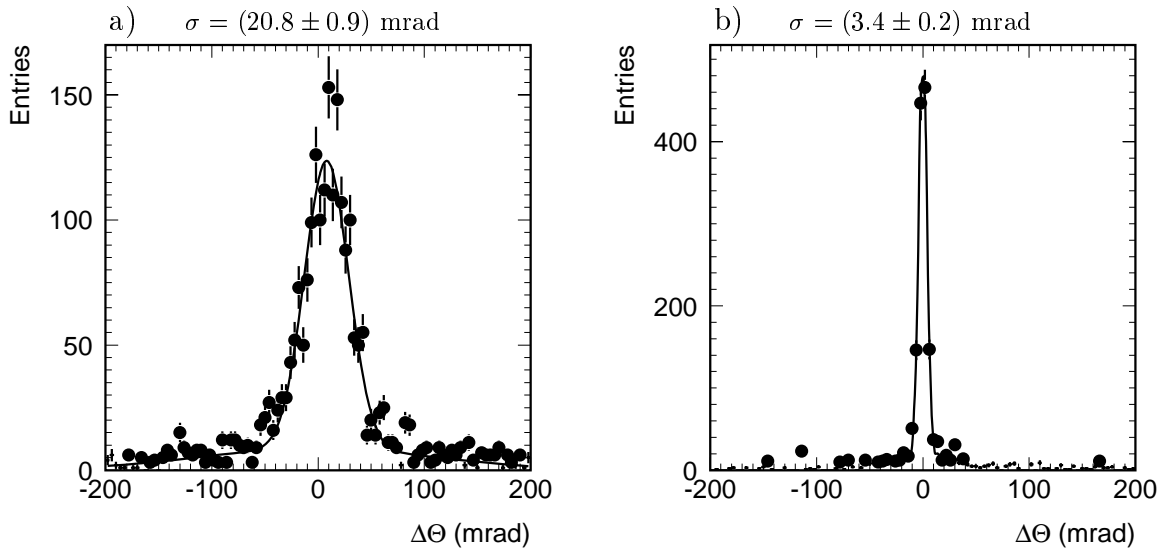


**Figure C.3:** Effect of the  $z$ -chamber information on the  $\theta$  resolution studied by comparing CST radical tracks (see text) with tracks measured in the drift chambers alone. The  $\Delta\theta$  distribution is shown for tracks with no linked  $z$ -chamber hits (a) and (b) for tracks having at least two linked hits in both the CIZ and COZ. The Gaussian width  $\sigma$  of the  $\Delta\theta$  distributions is quoted.

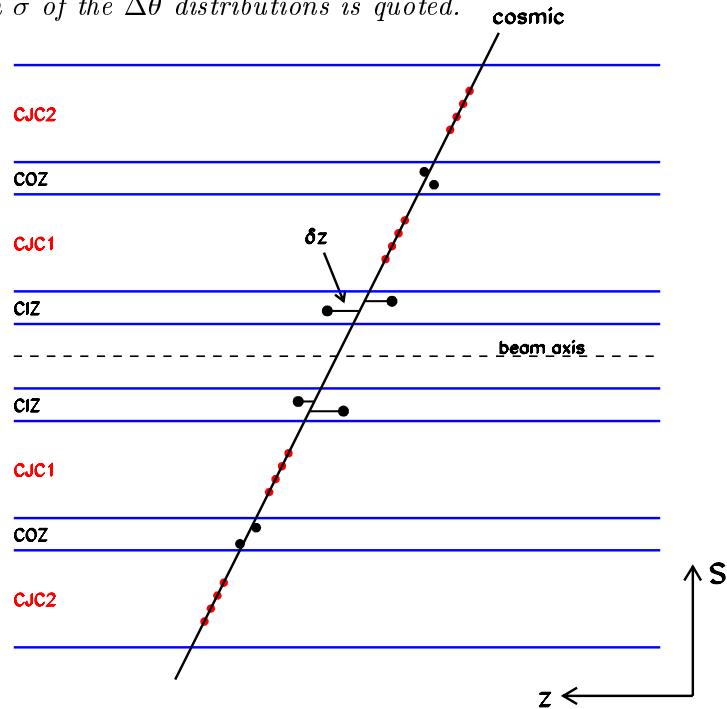


**Figure C.4:** Illustration of the CIZ calibration method using hit residual to cosmic tracks fitted to the COZ hits.

### C.3.1 CIZ calibration with cosmic tracks

The present procedure for calibrating the CIZ can be explained with reference to the illustration shown in Figure C.4. Cosmic events are used in which a lone cosmic penetrates

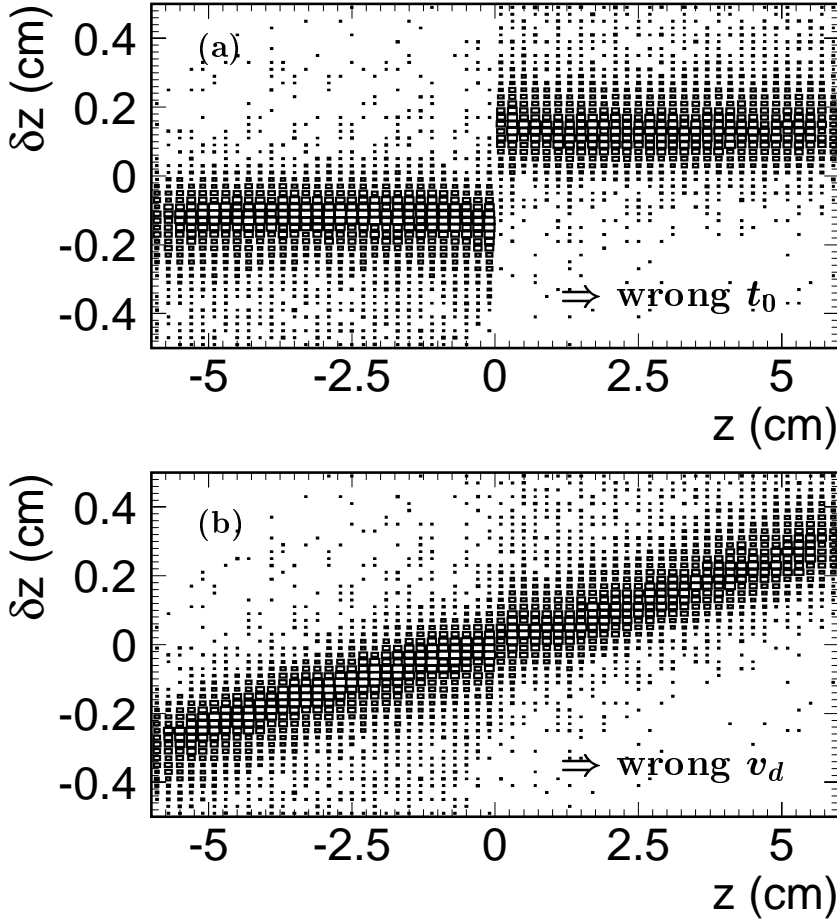


**Figure C.5:** Residuals  $\delta z$  versus the drift length  $z$  in the cell. Wrong calibration constants  $t_0$  (a) and  $v_d$  (b) show up as systematic shifts.

the H1 detector from above, passes through the COZ, CIZ, then near the beam axis, then through the CIZ and finally the COZ. Both the track measured in the *upper* half and the one measured in the lower half of the CJC must have at least two linked CIZ and COZ hits. A weighted averaging of the two sets of track parameters is performed where the upper and the lower track must agree within errors. The improved set of averaged track parameters is assigned to both cosmic track halves. Only tracks with a transverse momentum of  $p_T > 2$  GeV and a  $dca < 3$  cm are accepted. From the curvature  $\kappa = 1/R$  and the  $dca$  of the cosmic track the arc-lengths  $S_i$  of the COZ hits with radii  $r_i$  are calculated as

$$S_i = R \cdot \arccos \left( \frac{R^2 + d^2 - r_i^2}{2 \cdot R \cdot d} \right) \quad \text{with} \quad d = R - dca \cdot \text{sign}(\kappa). \quad (\text{C.6})$$

The COZ hits alone are then fitted to a straight line in the  $Sz$ -plane defining the *COZ reference track*. It should be noted from Equation C.6 that  $S$  is a function of  $\kappa$  and  $dca$  and thus the  $Sz$ -fit is not independent of the  $r\phi$ -coordinates. The calibration can now be checked by computing the  $z$ -residuals  $\delta z$  of the CIZ hits with respect to this reference track. As it is demonstrated in Figure C.5.a, a wrong drift time  $t_0$  (here  $\mathcal{O}(100$  ns)) leads to a mismatch in the distribution  $\delta z$  versus drift length  $z$ , since hits measured in the

left half of the drift cell are shifted to the opposite direction of those measured in the right half. A wrong drift velocity (here  $\mathcal{O}(5\%)$ ) results in a slope, seen in Figure C.5.b. A misalignment in  $z$  would appear as a global shift into one direction. For a correctly calibrated chamber the distribution should be flat and centered around zero. The width of the  $\delta z$ -distribution provides a measure of the resolution.

Assuming a correct drift velocity  $v_d$  the means of the  $\delta z$ -distribution for *left* hits  $\langle \delta z \rangle_l$  and *right* hits  $\langle \delta z \rangle_r$  can be used directly to calculate  $t_0$  and  $z$  wire by wire corrections as

$$\Delta t_0 = \frac{\langle \delta z \rangle_l - \langle \delta z \rangle_r}{2 \cdot v_d} \quad \text{and} \quad \Delta z_0 = \frac{\langle \delta z \rangle_l + \langle \delta z \rangle_r}{2}. \quad (\text{C.7})$$

The globally applied correction on the drift velocity  $\beta_v$  (see Equation C.2) is determined by fitting the slope of the distribution  $\delta z$  versus  $z$ .

So far only global fits for  $t_0$  and  $v_d$  have been performed assuming all wires to be identical and located at their nominal positions. Resolutions of the order  $\sigma_z \gtrsim 850 \mu\text{m}$  have been achieved. Using cosmic data of about  $10^6$  events detected in the early 1999 running period<sup>2</sup> a wire by wire calibration is performed according to the Equations C.7 after having determined  $\beta_v$  globally. The  $z$ -resolution is improved considerably to a value of  $\sigma_z \simeq 580 \mu\text{m}$  (Figure C.6) and quite large wire displacements of the order of up to  $\approx 500 \mu\text{m}$  are also corrected by the wire-wise calibration (Figure C.7).

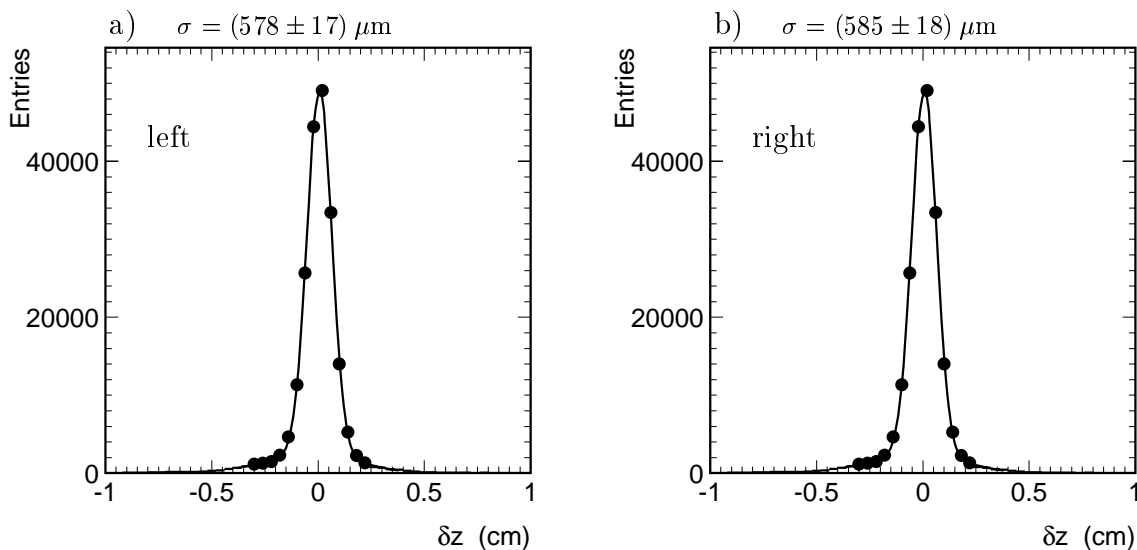


**Figure C.6:** Residuals  $\delta z$  measured with respect to the COZ reference track for hits measured (a) in the left cell half and (b) for those measured in the right cell half.

### C.3.2 Z-superfit

The calibration and alignment constants of the  $z$ -chambers can be determined using the superfit ansatz as it is implemented in the MILLEPEDE program [94]. Using the track

<sup>2</sup>In this period the CIZ and COZ have been almost fully operational

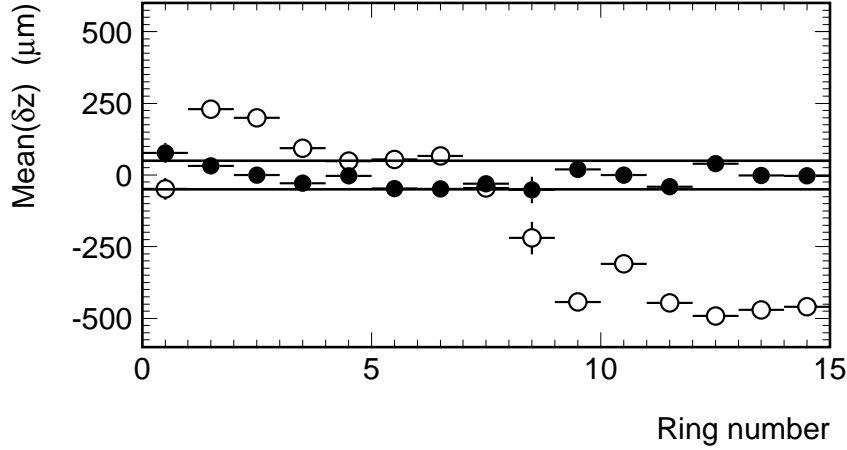


**Figure C.7:** Mean of  $\delta z$ -distribution versus ring number before (open dots) and after (full dots) a wire-wise  $\Delta t_0$  and  $\Delta z$  correction (see Equations C.7). The horizontal lines indicate the range  $\pm 50 \mu\text{m}$ .

information from many thousand events this algorithm allows for a simultaneous fit of all parameters relevant for the calibration. The  $z$ -superfit uses the CST 4-hit cosmic tracks as introduced in Section C.2. The geometrical alignment and calibration constants of the  $z$ -chambers determined by the superfit are global translations  $(\Delta x, \Delta y)$  and rotations  $(\gamma, \psi, \omega)$  around the  $z$ ,  $x$  and  $y$ -axis, wire-wise  $z$ -shifts  $\Delta z^1, \Delta z^2, \dots, \Delta z^{n_{\text{wire}}}$ , drift velocities  $v_d$  and drift time corrections  $t_0^1, t_0^2, \dots, t_0^{n_{\text{wire}}}$ . They can be integrated into one global fit-vector

$$\vec{P} = (\Delta x, \Delta y, \gamma, \psi, \omega, v_d, t_0^1, t_0^2, \dots, t_0^{n_{\text{wire}}}, \Delta z^1, \Delta z^2, \dots, \Delta z^{n_{\text{wire}}}) \quad (\text{C.8})$$

and the usual track model can be expanded to the form

$$z_{Hit} = z_0 + \lambda \cdot S_{Hit} + \vec{A} \cdot \vec{P}, \quad (\text{C.9})$$

with the slope  $\lambda = \cot(\theta)$  and the vector  $\vec{A}$  containing the derivatives  $\partial z / \partial \vec{P}$ . The alignment and calibration constants are then determined by minimizing the  $\chi^2$ -function

$$\chi^2 = \sum_i \left[ \sum_j \left( \frac{(z_j^i - (\vec{B}_j^i \cdot \vec{T}^i + \vec{A}_j^i \cdot \vec{P}^i))}{\sigma_j^i} \right)^2 + (\vec{T}^i - \vec{T}_{CST}^i)^t V_{T_{CST}^i}^{-1} (\vec{T}^i - \vec{T}_{CST}^i) \right] \quad (\text{C.10})$$

where for each track  $i$  it has to be summed over all related hits  $j$  measured in the CST, CIZ and COZ.  $\sigma_j^i$  is the uncertainty on the measured position  $z_j^i$  of the hit. In Equation C.10 the track model (compare Equation C.9) is written in general matrix notation as

$$\vec{B}_j^i \cdot \vec{T}^i = \begin{pmatrix} 1 & S_j^i \end{pmatrix} \begin{pmatrix} z_0^i \\ \lambda^i \end{pmatrix}. \quad (\text{C.11})$$

As can be seen in the second term of Equation C.10 the local parameters  $\vec{T}^i$  are simultaneously minimized, where  $\vec{T}_{CST}^i$  contains the parameters and  $V_{T_{CST}^i}$  the covariance matrix

of the  $i$ -th CST 4-hit cosmic track.

First results of the re-calibration according to the described  $z$ -superfit procedure are presented for the CIZ in Figure C.8 and for the COZ in Figure C.9. So far only central rings, which almost fully overlap with the CST, are considered. Shifts in the  $\delta z$ -distribution indicating a misalignmet vanish and the resolution improves for the CIZ from about  $500 \mu\text{m}$  to  $\sigma_z = (378 \pm 5) \mu\text{m}$  and for the COZ from about  $490 \mu\text{m}$  to  $\sigma_z = (423 \pm 5) \mu\text{m}$  after applying the superfit. This result can be compared with the *triplet* resolution of the  $z$ -chambers defined as the width of the distribution  $\sigma_T = z_i - 0.5(z_{i+1} + z_{i-1})$  divided by the term  $\sqrt{1.5}$ .  $\sigma_T$  is calculated for  $i = 1, 2$ , where  $i$  corresponds to the cell wire number. Triplet resolutions of about  $380 \mu\text{m}$  are obtained for both the CIZ and COZ.

Within the same framework also an *ep* calibration has become possible, allowing for immediate adjustments of short term variations of the drift velocity  $v_d$ .

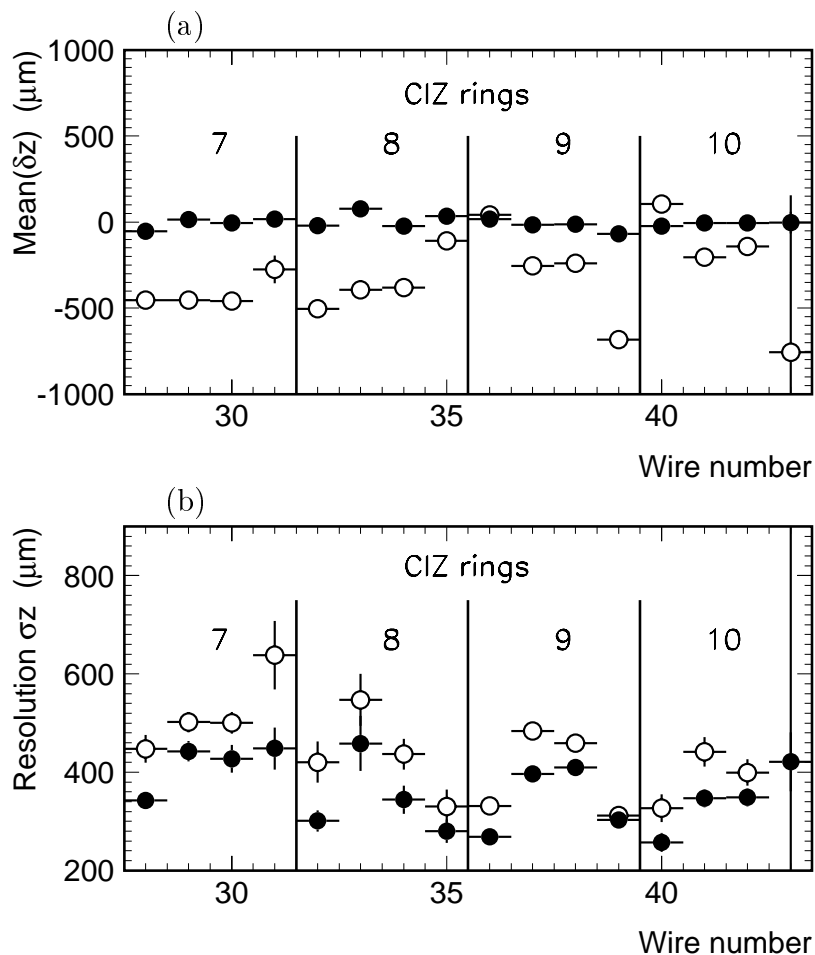


**Figure C.8:** (a) Residuals  $\delta z$  and (b) resolution  $\sigma_z$  versus wire number before (open dots) and after (full dots) the  $z$ -superfit calibration.

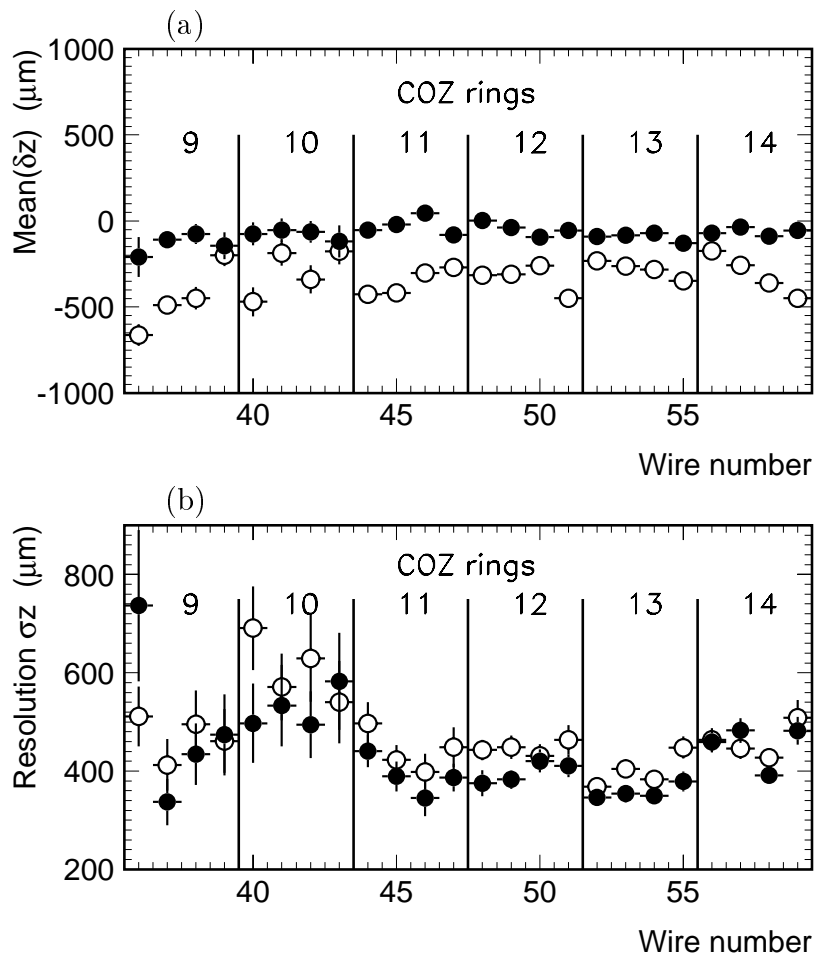


**Figure C.9:** (a) Residuals  $\delta z$  and (b) resolution  $\sigma_z$  versus wire number before (open dots) and after (full dots) the  $z$ -superfit calibration.

# List of Figures

1.1	Generic Feynman diagram for $ep$ -scattering . . . . .	4
1.2	Scaling violation of $F_2(x, Q^2)$ . . . . .	6
1.3	Charm production in leading order . . . . .	7
1.4	Peterson fragmentation of charm quarks. . . . .	9
1.5	Diagram for inclusive deep inelastic diffractive scattering . . . . .	10
1.6	The diffractive structure function . . . . .	13
1.7	$F_2^{D(3)}$ at $x_P = 0.003$ as a function of $Q^2$ . . . . .	15
1.8	$F_2^{D(3)}$ at $x_P = 0.003$ as a function of $\beta$ . . . . .	16
1.9	Light quark and gluon distributions to $z\mathcal{F}(z)$ . . . . .	17
1.10	Photon-gluon fusion in the resolved pomeron process . . . . .	18
1.11	Charm production by perturbative two gluon exchange . . . . .	18
1.12	Charm production via soft color interaction . . . . .	19
1.13	Definition of the azimuthal angle $\phi^*$ in the $\gamma^*\mathbb{P}$ CMS . . . . .	20
1.14	Parton level predictions for diffractive charm production in DIS . . . . .	22
2.1	The storage ring HERA and its pre-accelerators at DESY . . . . .	23
2.2	Integrated luminosity produced by HERA and measured in H1 (1992-2000)	24
2.3	Overview of the H1 detector . . . . .	25
2.4	H1 luminosity system . . . . .	26
2.5	The central tracking system, side view . . . . .	27
2.6	The central tracking detector, radial view . . . . .	28
2.7	CST geometry in the $r\phi$ -plane . . . . .	30
2.8	Schematic side view of the LAr calorimeter . . . . .	32
2.9	Side view of the backward detectors . . . . .	33

2.10	Schematic view of the four BDC double layers . . . . .	34
2.11	The forward muon detector . . . . .	35
2.12	Schematic view of the PRT . . . . .	36
2.13	Trigger levels used during 1994 to 1997 data taking . . . . .	37
2.14	Principle of the inclusive electron trigger . . . . .	38
2.15	Principle of the $z$ -vertex trigger . . . . .	39
3.1	Selection of positron candidates . . . . .	42
3.2	Inclusive $D^*$ signal . . . . .	46
3.3	Correlation between kinematic variables . . . . .	48
3.4	Number of $D^*$ candidates as a function of $\eta_{max}$ . . . . .	49
3.5	Acceptance for tagging the dissociated proton for the different forward detectors . . . . .	50
3.6	Acceptance of the forward cuts as a function of $ t $ . . . . .	51
3.7	Correlation between $x_P$ and $\eta_{max}$ . . . . .	52
3.8	Resolution of $x_P$ obtained from RAPGAP events . . . . .	53
3.9	Diffraction $D^*$ signal . . . . .	53
3.10	Side view of a diffractive $D^*$ candidate . . . . .	54
3.11	Front view of a diffractive $D^*$ candidate . . . . .	54
4.1	Noise level in the forward muon detector . . . . .	56
4.2	Trigger efficiencies 96 and 97 . . . . .	57
4.3	Efficiency of the selection cuts as a function of various variables . . . . .	60
4.4	The forward detector response in 97 . . . . .	62
4.5	Inclusive cross sections as a function of $p_T$ , $\eta$ , $Q^2$ and $y$ . . . . .	64
4.6	Differential cross sections $\sigma(ep \rightarrow e(D^*X)Y)$ as a function of $p_T^*$ , $x_P$ , $z_P^{obs}$ and $Q^2$ . . . . .	69
4.7	Differential cross sections $\sigma(ep \rightarrow e(D^*X)Y)$ as a function of $\beta$ , $y$ , $\eta$ , $p_T$ and $\phi^*$ . . . . .	70
4.8	$\Delta M$ signals in bins of $p_T^*$ , $Q^2$ , $x_P$ and $z_P$ . . . . .	71
4.9	Diffractive $D^*$ signal measured in the ZEUS kinematic range . . . . .	73
4.10	Kinematics and results of diffractive dijet production . . . . .	74

---

A.1	Invariant masses for $D^0 \rightarrow K^- K^+$ and $D^0 \rightarrow \pi^+ \pi^-$ decays . . . . .	79
A.2	Invariant masses for $D^0 \rightarrow K^- \pi^+ \pi^0$ decays . . . . .	81
A.3	Invariant masses for $D^0 \rightarrow \pi^+ \pi^- \pi^0$ decays . . . . .	81
A.4	Invariant masses for $D^0 \rightarrow K^- \mu^+ \nu_\mu$ decays . . . . .	81
B.1	$\Delta M$ distribution after a cut on the $D^0$ lifetime . . . . .	84
B.2	$D^0$ decay in the $r\phi$ -plane . . . . .	86
B.3	Lifetime distribution of $D^0$ mesons . . . . .	86
C.1	CIZ drift cell cross section . . . . .	87
C.2	Isochrone correction for CIZ . . . . .	88
C.3	Effect of the $z$ -chamber information on the $\theta$ resolution . . . . .	91
C.4	Calibration of the CIZ with COZ cosmic tracks . . . . .	91
C.5	Systematic shifts due to wrong calibration constants $t_0$ and $v_d$ . . . . .	92
C.6	Residuals $\delta z$ measured with respect to the COZ track . . . . .	93
C.7	Mean of $\delta z$ -distribution versus ring number . . . . .	94
C.8	Residuals $\delta z$ and resolution $\sigma_z$ versus wire number (CIZ) . . . . .	95
C.9	Residuals $\delta z$ and resolution $\sigma_z$ versus wire number (COZ) . . . . .	96

# List of Tables

2.1	Active regions of the central tracking chambers . . . . .	29
2.2	Helix parameters describing a track . . . . .	31
3.1	Integrated luminosities 1995 to 1997 . . . . .	41
3.2	Selection of $D^*$ mesons in DIS . . . . .	44
3.3	Branching ratios in the decay $D^* \rightarrow D^0 \pi_s \rightarrow (K\pi)\pi_s$ . . . . .	45
3.4	$\Delta M$ distribution fit results for the years 95, 96, 97 and the total sample . .	47
4.1	Trigger efficiencies 96 and 97 . . . . .	58
4.2	Efficiency of selection cuts . . . . .	59
4.3	Noise and $M_Y$ smearing corrections . . . . .	63
4.4	Predictions for the cross section $\sigma(ep \rightarrow e(D^*X)Y)$ of the different models	67
4.5	Kinematic regions measured by H1 and ZEUS . . . . .	72
A.1	$D^*$ decay modes and branching ratios . . . . .	78
B.1	Acceptance and efficiency for $D^*$ tagging with the CST . . . . .	83
C.1	Geometrical parameters of CIZ and COZ . . . . .	90

# Bibliography

- [1] R. Feynman, Phys. Rev. Lett. **23**, 1415 (1969).  
J.D. Bjorken, E.A. Paschos, Phys. Rev. **185**, 1975 (1969a).
- [2] C. Callan, D. Gross, Phys. Rev. Lett. **22**, 156 (1969).
- [3] J.D. Bjorken, Phys. Rev. **163**, 1767 (1967).
- [4] S. Aid et al., Nucl. Phys. B **470**, 3 (1996).
- [5] M. Bonesini et al., Z. Phys. C **38**, 371 (1988).
- [6] V. Gribov et al., Sov. J. Nucl. Phys. **15** 438 (1972).  
G. Altarelli, G. Parisi, Nucl. Phys. B **126**, 298 (1977).
- [7] F. Halzen, A. Martin, *Quarks & Leptons*, 1984, John Wiley & Sons.
- [8] B. Martin, G. Shaw, *Particle Physics*, 1992, John Wiley & Sons.
- [9] H1 Collaboration, Z. Phys. C **72**, 593 (1996).
- [10] H1 Collaboration., S. Adloff et al., Nucl. Phys. B **545**, 21 (1999).
- [11] B. Andersson, G. Gustafson, G. Ingelmann, T. Sjöstrand, Phys. Rep. **97**, 31 (1983).
- [12] C. Peterson, D Schlatter, I. Schmitt and P.M. Zerwas, Phys. Rev. D **27**, 105 (1983).
- [13] H. Albrecht et al. Z. Phys. C **52**, 353 (1991).
- [14] D. Bortoletto et al., Phys. Rev. D **37**, 1719 (1988).
- [15] M. Cacciari and M. Greco, Phys. Rev. D **55**, 7134 (1997).
- [16] J. Chrin, Z. Phys. C **36**, 163 (1987).
- [17] E. Norrbin, T. Sjöstrand, *Production and Hadronization of Heavy Quarks*, LU TP 00-16, hep-ph/0005110 May 2000.
- [18] T. Ahmed et al., Nucl. Phys. B **429**, 477 (1994).

- 
- [19] M. Derrick et al., Phys. Lett. B **315**, 481 (1993).
- [20] T. Regge, Nuovo Cim. **14** No. 5 951 (1959); T. Regge, Nuovo Cim. **18** 957 (1960).
- [21] P. D. B. Collins, *An Introduction to Regge Theory and High Energy Physics*, Cambridge University Press, Cambridge (1977).
- [22] A. Donnachie, P. Landshoff, Phys. Lett. B **296**, 227 (1992).
- [23] G. Ingelman, J. Bartels, Phys. Lett. B **255**, 175 (1990).
- [24] A. Donnachie, P. V. Landshoff, Phys. Lett. B **191**, 309 (1987).
- [25] H1 Collaboration, Z. Phys. C **76**, 613 (1997).
- [26] H. Jung, Comput. Phys. Commun. **86**, 147 (1995).
- [27] T. Sjöstrand, Comput. Phys. Commun. **39**, 347 (1986).
- [28] G. Ingelman, P. E. Schlein, Phys. Lett. B **152**, 256 (1985).
- [29] J. Bartels, H. Lotter, M. Wüsthoff, Phys. Lett. B **379**, 239 (1996).
- [30] J. Bartels, C. Ewerz, H. Lotter, M. Wüsthoff, Phys. Lett. B **386**, 389 (1996).
- [31] H. Lotter, Phys. Lett. B **406**, 171 (1997).
- [32] A. Edin, G. Ingelman, J. Rathsman, Z. Phys. C **75**, 57 (1997), Phys. Rev. D **56**, 7317 (1997).
- [33] G. Ingelman, J. Rathsman, G. A. Schuler, Comput. Phys. Commun. **101**, 135 (1997).
- [34] T. Sjöstrand, Comput. Phys. Commun. **82**, 74 (1994).
- [35] H1 Collaboration, Contrib. Paper No. 558 ICHEP 98, Vancouver, Canada.
- [36] M. Glück, E. Reya, A. Vogt, Z. Phys. C **67**, 433 (1995).
- [37] H1 Collaboration, Nucl. Instr. and Meth. A **386**, 310 (1997) and Nucl. Instr. and Meth. A **386**, 348 (1997).
- [38] H1 Calorimeter Group, B. Andrieu et al., Nucl. Instr. and Meth. A **344**, 492 (1994).
- [39] C. Kleinwort, private communication.
- [40] P. Robmann et al., Nucl. Instr. and Meth. A **277**, 368 (1989).
- [41] S. Egli et al., Nucl. Instr. and Meth. A **283**, 487 (1989).

- 
- [42] P. Robmann, *The central inner z-chamber of the H1 Experiment at HERA*, Ph.D. Thesis, University of Zürich (1994).
- [43] H. Bärwolff et al., Nucl. Instr. and Meth. A **283**, 467 (1989).
- [44] K. Müller et al., Nucl. Instr. and Meth. A **457**, 456 (1992).
- [45] D. Pitzl et al., *The H1 silicon vertex detector* hep-ex/0002044, submitted to Nucl. Instr. and Meth. **A**.
- [46] M. Kausch–Blecken v. Schmeling, *The Silicon Microvertex Detector of the H1 Experiment: Readout, Event Reconstruction, and Studies on Heavy Quark Decays*, Ph.D. Thesis, Hamburg (1998).
- [47] J. Gassner, *Messung der Ortsauflösung des H1-Siliziumvertexdetektors*, Diplomarbeit, ETH Zürich (1996).
- [48] C. Kleinwort and S. Schmitt, private communication.
- [49] V. Karimäki, Nucl. Instr. and Meth. A **305**, 187 (1991).
- [50] V. Blobel et al., *The new tracker bank scheme*, Internal H1 Software Note (1994).
- [51] M. Fleischer et al., *Performance and Upgrade of H1 Calorimeters: LAr Calorimeter, SpaCal and VLQ*, DESY Report 98-005 (1998).
- [52] H1 SpaCal Group, R. D. Appuhn et al., Nucl. Instr. and Meth. A **386**, 397 (1997).
- [53] A. Meyer, *Measurement of the Structure Function  $F_2(x, Q^2)$  of the Proton at low  $Q^2$  with the H1-Detector at HERA Using the New Detector Components Spacal and BDC*, Ph.D. Thesis, Hamburg (1997).
- [54] B. Schwab, *Das Rückwärtsdriftkammersystem des H1 Experiments*, Ph.D. Thesis, University of Heidelberg (1996).
- [55] J. Katzy, *Messung der Strukturfunktion bei kleinen Bjorken- $x$  und kleinen Impulsüberträgen am H1-Experiment bei HERA*, Ph.D. Thesis, University of Heidelberg (1997).
- [56] N. Keller, *Status of the BDC analysis*, Internal H1 Note H1-08/98-550 (1998).
- [57] H. Cronstrom et al., Nucl. Instr. and Meth. A **340**, 304 (1994).
- [58] H1 Collaboration, *Proposal for a Forward Proton Spectrometer for H1*, DESY Report 94-03 (1994).
- [59] T. C. Nicholls, *A Measurement of the Diffractive Proton Structure Function at HERA*, Ph.D. Thesis, University of Birmingham (1997).

- 
- [60] S. Eichenberger, *A Fast Pipelined Trigger for the H1 Experiment at HERA Based on Multiwire Proportional Chamber Signals*, Ph.D. Thesis, University of Zürich (1993).
- [61] H.P. Beck, *Measurement of the Total Photoproduction Cross Section at the Electron Proton Collider HERA at  $W_{\gamma P}$  of 200 GeV*, Ph.D. Thesis, University of Zürich (1996).
- [62] J. Riedlberger, *The H1 Trigger with Emphasis on Tracking Triggers*, H1 internal note H1-01/95-419 (1995), 5th International Conference on Advanced Technology and Particle Physics, Como, Italy, 3-7 October 1994.
- [63] *GEANT — Detector Description and Simulation Tool*, CERN Program Library Long Writeup W5013.
- [64] S. Peters, *Die parametrisierte Simulation elektromagnetischer Schauer*, Ph.D. Thesis, Hamburg (1992).
- [65] M. Rudowicz, *Hadronische Schauersimulation für den H1 Detektor*, Ph.D. Thesis, Hamburg (1992).
- [66] A. Meyer, *Measurement of the Structure Function  $F_2(x, Q^2)$  of the Proton at Low  $Q^2$  with the H1 Detector at HERA Using the New Detector Components Spacal and BDC*, Ph.D. Thesis, Hamburg (1997).
- [67] D. Müller, *A Measurement of the Gluon Density in the Proton Based on Charm Produktion at HERA*, Ph.D. Thesis, University of Zürich (1998).
- [68] C. Caso et al., (Particle Data Group), *Eur. Phys. J. C* **3**, 1 (1998).
- [69] G. Feldmann et al., *Phys. Rev. Lett.* **38**, 1313 (1997).
- [70] W. Erdmann, *Untersuchung der Photoproduction von  $D^*$  Mesonen am ep-Speicherring HERA*, Ph.D. Thesis, University of Zürich (1996).
- [71] F. James, CERN Program Library Long Writeup D506.
- [72] A.T. Doyle et. al. *Monte Carlo Generators for HERA Physics*, DESY-PROC-1999-02.
- [73] B. List, *Diffraktive  $J/\psi$ -Produktion in Elektron-Proton-Stößen am Speicherring HERA*, Diploma Thesis, Techn. Univ. Berlin (1993).
- [74] P. Thompson, *Open Charm Production in Inclusive and Diffractive Deep-Inelastic Scattering at HERA*, Ph.D. Thesis, University of Birmingham (1999).
- [75] C.M. Cormack, *Measurements of Hadron Production in Deep Inelastic Diffractive Scattering*, Ph.D. Thesis, University of Liverpool (1997).

- 
- [76] A.A. Glazov, *Measurement of the Proton Structure Functions  $F_2(x, Q^2)$  and  $F_L(x, Q^2)$  with the H1 Detector at HERA*, Ph.D. Thesis, University of Berlin (1998).
- [77] L. Lönnblad, *Comput. Phys. Commun.* **71**, 15 (1992).
- [78] G. Gustafson, *Phys. Lett. B* **175**, 453 (1986).
- [79] H1 Collaboration, *Z. Phys. C* **74**, 221 (1997).
- [80] H1 Collaboration, *Z. Phys. C* **75**, 607 (1997).
- [81] H1 Collaboration, *Phys. Lett. B* **338**, 507 (1994).
- [82] H1 Collaboration, *Phys. Lett. B* **428**, 206 (1998).
- [83] N. Gogitidze, S. Levonian, H1 internal note H1-02/96-471
- [84] ZEUS Collaboration, *Open Charm Production in Deep-Inelastic Scattering at HERA*, contributed paper to ICHEP 1998, Vancouver, Canada.
- [85] ZEUS Collaboration, *Study of  $D^*$  Meson Production in Diffractive Deep-Inelastic  $ep$  Scattering at HERA*, contributed paper to HEP 1999, Tampere, Finland.
- [86] H1 Collaboration, *Eur. Phys. J. C* **6**, 421 (1999).
- [87] H1 Collaboration, *Diffractive Jet Production in Deep-Inelastic  $e^+p$  Collisions at HERA*, contributed paper to ICHEP 2000, Osaka, Japan.  
F.P. Schilling, PhD Thesis in preparation, University of Heidelberg.
- [88] CDF Collaboration, *Eur. Phys. J. C* **13**, 397 (2000).
- [89] H1 Collaboration, *A Measurement of the Production of  $D^*$  Mesons in Deep-Inelastic Diffractive Interactions at HERA*, contributed paper pa02-060 to ICHEP 1996, Warsaw, Poland.
- [90] P. Billoir et al., *Track element merging strategy and vertex fitting in complex modular detectors*, NIM 1241 (1985) 115-13.
- [91] G. Lutz *Topological Vertex Search in Collider Experiments*, MPI-PhE/92-09.
- [92] T. Kuhr, private communication.
- [93] J. Fehlmann, *WIRCHA a program package to simulate drift chambers*, ETH Zürich (1985).
- [94] V. Blobel, *Linear Least Squares Fits with a Large Number of Parameters*, II Institut für Experimentalphysik, Universität Hamburg (1999).

---

# Acknowledgments

I wish to express my sincere gratitude to Prof. Dr. Peter Truöl for offering me the opportunity to work as a Ph.D. student for the H1 experiment.

I am very grateful to Dr. Felix Sefkow for his continuous support throughout my time as a member of the Zürich group. I benefited considerably from his experience and his advice has always been very helpful.

The physics analysis presented in this thesis has been performed in close collaboration with Paul Thompson. I would like to thank him particularly for his contribution to the “diffractive part” of the analysis. I am also indebted to Paul for proof-reading and commenting on substantial parts of this thesis.

The status of the analysis has been reported frequently to the Heavy Flavor and the Diffractive Working Group. Thanks to the members of both groups for their review and support.

Special thanks to all my colleagues from the University of Zürich. During shutdown periods, or whenever problems occurred with the detector components, I have been responsible for, I have been fortunate to work with the hardware specialists from Zürich University, Peter Robmann, Stefan Steiner and Kurt Bösiger.

I really enjoyed the pleasure and always friendly atmosphere in our Hamburg office which I shared most of the time with Martin zur Nedden, David Müller and Jürgen Kroseberg.

Last, but not least, I gratefully acknowledge the financial and moral support I got from my family, without which I would have been unable to complete my studies.

*This work has been supported by the Swiss National Science Foundation.*

---

## Curriculum Vitae

### Personalien:

Name: Stefan Alexander Hengstmann  
Bürgerort: Hamburg, Blankenese  
Geboren: 20. 12. 65, Hamburg

### Bildungsgang:

1972 - 76 Grundschole in Hamburg Blankenese  
1976 - 86 Gymnasium in Hamburg, Blankenese  
1986 Abitur der Freien und Hansestadt Hamburg  
1989 - 95 Studium der Physik (Mathematik, Astronomie) an der  
Universität Hamburg  
1995 - 96 Diplomarbeit in Experimentalphysik unter der Leitung  
von Prof. Dr. B. Naroska und Dr. R. Gerhards  
1996 Diplom in Experimentalphysik  
1997 - 2000 Wissenschaftliche Mitarbeit beim H1 Experiment am  
DESY Hamburg, Dissertation bei Prof. Dr. P. Truöl.

### Dozentenverzeichnis:

#### Universität Zürich:

C. Amsler	D. Brinkmann	R. Engfer	W. Jaus
U. Straumann	P. Truöl		

#### Universität Hamburg:

J. Bartels	R. Berndt	V. Blobel	U. Borgeest
D. Buchholz	F.W. Büber	D. Fay	V. Günther
G. Heinzelmann	G. Knies	C. Kunz	R. Langkau
G. Lindström	G. Mack	B. Naroska	H. Nicolai
S. Refsdal	D. Reimers	V. Riech	O. Riemenschneider
K. Scharnberg	W. Scobel	R. Stanik	F. Steiner
H.D. Wendt	H. Wendker	K. Wick	